DEVELOPMENT OF RARE-EARTH FREE PERMANENT MAGNETS

A THESIS SUBMITTED TO
THE GRADUATE SCHOOL OF NATURAL AND APPLIED SCIENCES
OF
MIDDLE EAST TECHNICAL UNIVERSITY

BY

AYŞE MERVE GENÇ ÜNALAN

IN PARTIAL FULFILLMENT OF THE REQUIREMENTS
FOR
THE DEGREE OF DOCTOR OF PHILOSOPHY
IN
METALLURGICAL AND MATERIALS ENGINEERING

OCTOBER 2017

Approval of the thesis:

DEVELOPMENT OF RARE-EARTH FREE PERMANENT MAGNETS

submitted by **AYŞE MERVE GENÇ ÜNALAN** in partial fulfillment of the requirements for the degree of **Doctor of Philosophy in Metallurgical and Materials Engineering Department, Middle East Technical University** by,

Prof. Dr. Gülbin Dural Ünver _____
Dean, Graduate School of **Natural and Applied Sciences**

Prof. Dr. C. Hakan Gür _____
Head of Department, **Metallurgical and Materials Engineering**

Assoc. Prof. Dr. Y. Eren Kalay _____
Supervisor, **Metallurgical and Materials Eng. Dept., METU**

Prof. Dr. M. Vedat Akdeniz _____
Co-Supervisor, **Metallurgical and Materials Eng. Dept., METU**

Examining Committee Members:

Prof. Dr. Tayfur Öztürk _____
Metallurgical and Materials Engineering Dept., METU

Assoc. Prof. Dr. Y. Eren Kalay _____
Metallurgical and Materials Engineering Dept., METU

Assoc. Prof. Dr. Burcu Akata Kurç _____
Micro Nanotechnology Dept., METU

Assoc. Prof. Dr. Yiğit Karpat _____
Industrial Engineering Dept., BILKENT UNIVERSITY

Assist. Prof. Dr.Caner Şimşir _____
Manufacturing Engineering Dept., ATILIM UNIVERSITY

Date: 11.10.2017

I hereby declare that all information in this document has been obtained and presented in accordance with academic rules and ethical conduct. I also declare that, as required by these rules and conduct, I have fully cited and referenced all material and results that are not original to this work.

Name, Last name: Ayşe Merve Genç Ünalan

Signature :

ABSTRACT

DEVELOPMENT OF RARE-EARTH FREE PERMANENT MAGNETS

Genç, Ayşe Merve

Ph.D., Department of Metallurgical and Materials Engineering

Supervisor: Assoc. Prof. Dr. Y. Eren Kalay

Co-supervisor: Prof. Dr. M. Vedat Akdeniz

October 2017, 145 pages

Magnetic materials play a critical role in devices for the conversion, transmission and energy storage. There is a growing demand for NdFeB permanent magnets with high coercivity and magnetic flux. These magnets have been the focus of research for almost 30 years. While magnets are increasingly dependent upon rare-earths, there has been an effort to minimize or substitute their use.

In this study, two permanent magnet alloys without any rare-earth elements have been investigated in details. AlNiCo magnets are good candidates to be produced with novel methods and investigated with the latest analysis techniques. Magnetic materials exhibit unique properties at nanoscales and the behavior of AlNiCo magnets in nanoscale is uncertain. Ball milling and hydrogen plasma experiments have been carried out for nanopowder synthesis. Nanoparticles of AlNiCo 5-7 alloy produced by plasma technique showed higher coercivity relative to ball-milled powders. Core/shell structure contributes to the increase in coercivity due to effective exchange coupling and the shell serves as a protective layer against room temperature oxidation.

Magnetism of MnAl alloys derives from a ferromagnetic metastable τ-phase. In order to improve the magnetic properties, ε-to-τ transformation should be well established. Microstructural, thermal and crystallographic analysis are carried out with synchrotron analysis. It is observed that there is a compositional limit to ferromagnetic τ-phase formation. ε→τ transformation is found to be dependent on ordering of the ε-phase and can only proceed with ε'-phase. As Mn content increases compositional ordering do not take place and stable phases form.

In the third part of the study, 3D printing is presented as a novel manufacturing method for permanent magnets in composite structure. A filament of magnetic MnAl powders embedded in a polymer binding material is produced through extrusion. Operating parameters are optimized and several prototypes are printed. It is observed that magnetic properties of bonded magnets are affected by the weight ratio and magnetic properties of the magnetic filler.

Keywords: Permanent magnets, Mn-Al alloys, τ-MnAl, ε' phase, ferromagnetic, high-energy X-ray diffraction.

ÖZ

NADİR TOPRAK ELEMENTİ İÇERMEYEN MIKNATIS GELİŞTİRİLMESİ

Genç, Ayşe Merve

Doktora, Metalurji ve Malzeme Mühendisliği Bölümü

Tez Yöneticisi: Doç. Dr. Y. Eren Kalay

Ortak Tez Yöneticisi: Prof. Dr. M. Vedat Akdeniz

Ekim 2017, 145 sayfa

Manyetik malzemeler enerjinin korunması, aktarılması ve dönüşümünde kullanılan cihazlarda önemli bir yol oynamaktadır. Koersifliği yüksek kalıcı mıknatıslara gereksinimin artması ile birlikte nadir toprak elementi içeren NdFeB mıknatısları önem kazanmıştır. Yaklaşık 30 senedir çalışmaların odak noktası bu mıknatıs olmuştur. Nadir toprak elementlerine talep arttıkça, kritik önemdeki malzemelerde nadir toprak elementlerinin kullanımının kısıtlanması ya da bitirilmesi söz konusu olmuştur.

Bu çalışmada, daha önceden üzerinde çalışılmış ve ticarileşmiş bir alaşım olan AlNiCo ile henüz ticarileşmemiş, diğerine kıyasla yeni sayılabilecek bir alaşım olan MnAl alaşımı kullanılmıştır. AlNiCo mıknatısları gelişmiş analiz teknikleri ile yeniden araştırılmak için iyi bir adaydır. Nano boyutlardaki davranışı henüz kesinleşmemiştir. Bu çalışmada bilyalı değirmen ve plazma ünitesinde parçacık boyutunu azaltmak için deneyler yapılmıştır. Plazma deneylerinin sonunda bilyalı değirmenle öğütülmüş numunelere göre daha yüksek koersifliğe ulaşılmıştır. Çekirdek yapının aynı zamanda oksitlenme için bir koruyucu tabaka oluşturduğu gözlemlenmiştir.

Manganez alüminyum alaşımlarının mıknatıslığı ferromanyetik τ-fazının oluşmasından kaynaklanmaktadır. ε-τ faz dönüşümünün anlaşılmasıyla manyetik özellikleri iyileştirmek mümkün olacaktır. Bunun için faz dönüşümünün mikroyapısı, termal ve kristallografi analizin yanı sıra sinkrotron deneyleri ile kompozisyon optimizasyonu da yapılmıştır. Ferromanyetik τ-fazının oluşması için alaşımda belli bir Manganez miktarının olması gerektiği gözlemlenmiştir. ε→τ dönüşümü ε-fazının düzenine bağlı olduğu ve düzenli ε'-fazı olmadan τ-fazının oluşmadığı fark edilmiştir. Mn miktarı arttıkça ε' ve τ-fazları oluşmamakta, kararlı fazlar oluşmaktadır.

Çalışmanın üçüncü bölümünde, 3B yazıcılar kompozit yapıdaki kalıcı mıknatısların üretimi için yeni bir üretim metodu olarak öne sürülmüştür. Üretilip, karakterize edilen nadir toprak elementi içermeyen MnAl tozları polimer ekstrüsyon yöntemi ile bir filament haline getirilmiştir. Manyetik özelliklerinin içerisindeki toz miktarına ve tozların mıknatıslanma miktarına bağlı olduğu gözlemlenmiştir.

Anahtar Kelimeler: Kalıcı mıknatıslar, Mn-Al alaşımları, τ-MnAl, ε' fazı, ferromanyetik, yüksek enerjili X-ışını kırınımı

To Ayşe Gülhis Yavaş,

ACKNOWLEDGMENTS

Foremost, I would like to express my deepest gratitude to my advisor Assoc. Prof. Dr. Y. Eren Kalay for the continuous support of my Ph.D research, for his contribution, inspiration, motivation, enthusiasm and guidance throughout my research. This thesis would not have been possible without his expert assistance and invaluable mentoring. I'm forever grateful and honored to be his first Ph.D student.

I would like to acknowledge my co-advisor Prof. Dr. Vedat Akdeniz for his support and guidance throughout my research.

I am also grateful to Asst. Prof. Dr. Meltem Sezen for her contribution and support in focused ion beam studies. I would also like to acknowledge Prof.Dr. Servet Turan and Umut Savacı for their help in in-situ TEM studies. I would also like to acknowledge Assoc.Prof.Dr.Abdullah Ceylan, Serkan Yılmaz, Baran Tunç, Burak Aktekin, Zülal Ateş and Mehmet Yıldırım for their assistance and support in certain stages of my thesis.

I wish to thank the members of my thesis progress meeting committee, Prof. Dr. Tayfur Öztürk and Assoc. Prof. Dr. Burcu Akata Kurç for their invaluable participation and insights. Their support and guidance throughout the research are greatly appreciated.

I owe particular thanks to my laboratory mates whom I shared all the ups and downs from day one; Güher and Evren Tan, Şeyda Küçükyıldız, Gökçe Şen, Elif Selen Ateş, Tuba Demirtaş, Şermin Turhan, Can Yıldırım, Mertcan Başkan, Mustafacan Kutsal, Özgün Acar, Sıla Atabay, Fatih Sıkan, Gökhan Polat, Doğancan Sarı and at last but not least Bengisu Yaşar for making every situation better with their support and friendship.

At last but not least, my special thanks are owed to my parents; F.Payidar and M.Cansen Genç for always being there for me, for encouraging me to do my best, for

their understanding and patience throughout my years of education. I wish to thank my husband; Emrah for his guidance and motivation, and our parents; Leyla and Güner Ünalan for their love and support. Special thanks to my uncles and aunts (Fatih, Cenk, Meltem, Deborah Yavaş) and my cousins (Yasemin, Ömer, Derin, Demir Yavaş) for their love and support. I also want to thank my friends (Ezgi, Gizem, Ezgi, Melis, Esra, Dilek, Işıl, Berkem and Emel) for their continuous support and friendship.

In-situ high energy X-ray experiments in this research was undertaken on the BL04-MSPD beamline at the ALBA Synchrotron facility, Spain.

TABLE OF CONTENTS

ABSTRACT…... v
ÖZ……... vii
ACKNOWLEDGMENTS ... x
TABLE OF CONTENTS ... xii
LIST OF TABLES ... xiv
LIST OF FIGURES ... xv
NOMENCLATURE ... xxiii
CHAPTERS
1. INTRODUCTION TO PERMANENT MAGNETISM ... 1
1.1 The Magnetism ... 1
1.2 History and Applications of Commercial Permanent Magnets ... 7
1.3 Problem Description and Objective of the Study ... 13
2. SYNTHESIS OF ALNICO CORE/SHELL NANOPOWDERS ... 17
2.1 Introduction ... 17
2.2 AlNiCo Permanent Magnets ... 18
2.3 Magnetic Nanoparticles ... 20
2.4 Plasma Synthesis of Magnetic Nanoparticles ... 22
2.5 Core/Shell Structured Nanoparticles ... 25
2.6 AlNiCo 5-7 Powder Synthesis ... 27
2.6.1 Production of Alloys ... 27
2.6.2 Mechanical Milling ... 28
2.6.3 Plasma Synthesis ... 29
2.6.4 Characterization Techniques ... 32
2.7 Results and Discussion ... 35
2.8 Conclusions ... 42

3. INVESTIGATION OF PHASE SELECTION HIERARCHY IN MnAl-BASED ALLOYS……..…...…….....….45
3.1 Introduction 45
3.2 MnAl Alloy Transformations 46
3.3 Experimental Procedure 53
3.3.1 Production of Alloys 53
3.3.2 Heat Treatment 53
3.3.3 Characterization Techniques 54
3.4 Results and Discussion 61
3.4.1 Synchrotron Analyses 62
3.4.2 Differential Scanning Calorimetry Analysis 68
3.4.3 Magnetic Measurements 73
3.4.4 Transmission Electron Microscopy Analyses 75
3.5 Conclusions 87
4. 3D PRINTING..……..……..……..……..……..……..…89
4.1 Introduction 89
4.2 Polymer Bonded Magnetic Materials……..……...89
4.3 3D Printing 93
4.4 Experimental Procedure 95
4.5 Results and Discussion……..……...100
4.6 Conclusions 109
5. CONCLUSION AND FUTURE RECOMMENDATIONS 111
5.1 Conclusion 111
5.2 Future Recommendations 113
REFERENCES..... 117
APPENDIX A: PERMISSION LICENCES….……...…….…..…..…133
CURRICULUM VITAE.....……..……..…….143

LIST OF TABLES

TABLES

Table 1. 1 Magnetic properties of permanent magnets [9]. 11
Table 1. 2 Sales prices of some rare-earth oxides in 2009 and 2011 [24] 14

Table 2. 1 Process parameters of the induction plasma system…….……31
Table 2. 2 Average EDS data of the core and shell structure from 10 measurements.40

Table 3. 1 EDS results of the samples S1, S2, S3, and S4. Mn and Al ratios of the alloys are given in atomic and weight percentages…….……... 62
Table 3. 2 Critical transformation temperatures of ε, ε', τ and stable phases for alloys S1, S2, S3 and S4……67
Table 3. 3 Onset, peak and offset temperatures of S1, S2 and S4 alloys heated at a rate of 10°C in DSC……...…… 71
Table 3. 4 Calculated activation energies for S1, S2 and S4 samples with Kissinger and Ozawa approaches……...…….73
Table 3.5 Comparison of the transformation temperatures obtained using various characterization techniques……..……...84

Table 4. 1 Printing parameters for the 3D printers utilized in this work……..…... 106

LIST OF FIGURES

FIGURES

Figure 1. 1 Hysteresis loop of a permanent magnet and the stages in the alignment of magnetic moments. 1

Figure 1. 2 The atomic dipole configurations for diamagnetic, paramagnetic, ferromagnetic, antiferromagnetic materials with and without magnetic field [2]. 4

Figure 1. 3 Typical schematic hysteresis loops for diamagnetic, paramagnetic, superparamagnetic and ferromagnetic materials. 5

Figure 1. 4 Types of commercialized permanent magnets. 8

Figure 1. 5 Maximum achieved energy density BHmax of permanent magnetic materials in the 20th Century showing how BHmax has improved exponentially [16]. 10

Figure 1. 6 Evolution of Chinese rare earth element supply and demand, export quotas from 2005 to 2015, in metric tones [23] 14

Figure 2. 1 (a) Bright field micrograph in longitudinal view, (b) conventional dark field image in transverse view of AlNiCo 5-7 [28]……...……..18

Figure 2. 2 Change in magnetic response (coercivity) with respect to the particle size [35]……..……....20

Figure 2. 3 Schematics of (a) a single large domain structure with extended large magnetic field, (b) Two domain structure with magnetic dipoles at opposite directions reducing the field outside, (c) Stable multi domain structure, where small parallel

domains have magnetization in alternating directions, (d) A smaller grain, which can only hold two domain structure, (e) Uniformly magnetized single domain, f) Superparamagnetic structure, where domain boundary can no longer fit..……..... 21

Figure 2. 4 The relationship between saturation magnetization and coercivity with respect to the mean particle size diameter for AlNiCo 5 alloys [45]……..…...….25

Figure 2. 5 Schematic illustration of a core/shell structure…… 26

Figure 2. 6 Photos of (a) Edmund Bühler arc-melter used for the preparation of samples (b) Pure elements inside the chamber before melting process……28

Figure 2. 7 D50 and D90 values for various milling conditions. Error bars on this plot represents 95% confidence interval of the mean…… 29

Figure 2. 8 Schematic illustration of the Tekna thermal induction plasma system [70]……..…….....30

Figure 2. 9 Photos of (a) vibrational powder feeder system and (b) the plasma reactor [70]……..…….....31

Figure 2. 10 Secondary electron images of the FIB procedure showing the sectioning, trenching, cutting and welding stages, respectively…….……...34

Figure 2. 11 SEM micrographs of ball milled and sieved samples with sieve sizes of (a) +149 µm, (b) -149 µm +75 µm, (c) – 75 µm +63 µm and (d) -63 µm +45 µm at different magnifications……...……... 36

Figure 2. 12 SEM micrographs of plasma synthesized AlNiCo alloy at different magnifications…….....37

Figure 2. 13 (a)(b)(c) Bright-field TEM images of plasma synthesized powders at different magnifications (d) STEM image showing the core/shell structure...……... 38

Figure 2. 14 (a)(b) STEM micrograph showing the region of interest where EDS analysis is carried out, (c) STEM EDS analysis of the core and shell layers showing

the difference in the oxygen content, (d) SAED pattern showing the Fe_3O_4 and FeCo/NiAl reflections...……..39

Figure 2. 15 (a) X-ray diffraction pattern of the ball-milled powders before and after plasma reaction. (b) X-ray diffraction pattern of the ball milled and sieved powder. 40

Figure 2. 16 (a) Hysteresis loops of the ball-milled/sieved and plasma synthesized powders, inset shows the improvement in the Hc after plasma reaction, (b) the change in Hc of the powders with respect to the average particle size……... 41

Figure 3. 1 Schematic atomic structures of (a) an face-centered cubic and (b) a body-centered tetragonal $L1_0$ [83]……..……..…… 46

Figure 3. 2 Phase diagram of Mn-Al system [87]……...48

Figure 3. 3 Portion of the phase diagram showing the ε→τ transition……... 48

Figure 3. 4 The transformation sequence of hexagonal ε to τ-phase. ε transforms into cubic B19 ε'-phase followed by τ-phase formation through martensitic shear [106].50

Figure 3. 5 Schematics of the orientation relationship (a) between matrix ε and three variants of ε' (b) shearing transformation of ε and major ε' variant to τ-phase along [001] (ε1′) [112]…….….51

Figure 3. 6 Secondary electron images of FIB samples (a) $Mn_{67,5}Al_{32,55}$ (b) $Mn_{70}Al_{30}$ (c) $Mn_{71,5}Al_{28,5}$ (d) $Mn_{73}Al_{27}$…….....54

Figure 3. 7 (a) Electron microscopy image of the in situ heating holder. The area of interest is marked by a square. (b) Bright field image of the sample attached to the in situ holder. (c) Bright field image of the sample after heating. (d) Dark field image of the sample after heating showing the Ga ion coalescence……..56

Figure 3. 8 (a) DSC instrument, (b) Al pans and lids along with the pressing tool to cover the lids and (c) heating chamber……..……..57

Figure 3. 9 Principle features of a synchrotron facility showing the path of synchrotron radiation……..……59

Figure 3. 10 BL04-MSPD beamline in ALBA Synchrotron Radiation Light Source.60

Figure 3. 11 Conventional XRD spectra of sample (a) S1, (b) S2, (c) S3, and (d) S4 after solutionizing……..... 61

Figure 3. 12 2-D film synchrotron plots of (a) S1 (b) S2, (c) S3 and (d) S4…..…… 63

Figure 3. 13 HEXRD patterns of the alloys (a) S1, (b) S2, (c) S3 and (d) S4 within 8,2 -9,6° a 2Θ range of 8.2-9.6° showing the evolution of ε' peak at different temperatures……..……..64

Figure 3. 14 HEXRD patterns of the alloys (a) S1, (b) S2, (c) S3 and (d) S4 within a 2Θ range of 11-15° showing the formation of τ-MnAl peak upon heating..…….. 65

Figure 3. 15 High energy X-ray diffraction patterns of the alloys (a) S1, (b) S2, (c) S3 and (d) S4 within 4-11° (2Θ) range showing the formation of the stable phases upon heating……..……...66

Figure 3. 16 DSC heating curves of S1, S2, S3 and S4 with a heating rate of 10 K/min from room temperature to 773 K (500 °C)…… 69

Figure 3. 17 Gaussian fitted DSC scans for (a) S1 alloy and (b) S4 alloy both with a heating rate of 10 °C/min. Black line represents the original data and red line represents the Gaussian fit…….....70

Figure 3. 18 Kissinger and Ozawa plots for (a) S1 alloy τ-phase, (b) S2 alloy τ-phase, (c) S1 alloy β-phase and (d) S2 alloy β–phase……72

Figure 3. 19 Hysteresis curves of S1, S2, S3 and S4. Inset shows the second quadrant of the B-H curve of S1 and S2 specimens……...…….... 74

Figure 3. 20 Dependence of energy product on field strength for samples S1 and S2……..……..... 74

Figure 3. 21 Bright field TEM images of samples (a) S1 (b) S2 (c) S3 (d) S4, insets showing the selected area diffraction patterns and zone axes…….75

Figure 3. 22 HRTEM images and corresponding FFT images obtained from S1..… 76

Figure 3. 23 (a) Schematic illustration of the ε-phase atomic structure along [110] zone axis, (b) corresponding diffraction pattern of ε along [110] zone axis, (c) atomic structure of ε' when rotated along ε [110], (d) corresponding diffraction pattern of ε' when rotated along ε [110]……..77

Figure 3. 24 (a) 2D model of MnAl box with ε' variant oriented along [001] zone axis, (b) HRTEM image simulation of MnAl box with ε' variant along [001] zone axis; inset showing the FFT image, (c) 2D model of MnAl box with ε' variant oriented along [110] zone axis, (d) HRTEM image simulation of MnAl box with ε' variant oriented along [110] zone axis. The insets show FFT images of the marked areas...……...79

Figure 3. 25 Screenshots extracted from the dynamic video sequence during in-situ heating TEM experiment of sample S2 at temperatures of (a) 30, (b) 390, (c) 430, (d) 450, (e) 460 and (f) 500°C. Dashed lines indicate the grain boundary between ε and β-phases……..……81

Figure 3. 26 Screenshots extracted from the dynamic video sequence during in-situ heating TEM experiment of sample S4 at temperatures of (a) 30, (b) 340, (c) 400, (d) 470, (e) 480 and (f) 500°C. Dashed lines indicate the grain boundary between ε and β-phases…… 82

Figure 3. 27 Bright-field TEM images of sample (a), (b) at room temperature and (c), (d) quenched at 210°C. Insets show the diffraction patterns and zone axis……..... 85

Figure 3. 28 Two bright-field TEM images obtained from different locations on the sample quenched at 375°C. Arrow and dashed line at (b) indicates the morphologically plate-like τ-phase……..…….. 86

Figure 3. 29 Two bright field TEM images obtained from different locations on the sample quenched at 480°C. The grains marked on (a) and (b) are identified as stable β-phase. Dashed line indicates the morphologically plate-like τ-phase……..…... 86

Figure 4. 1 Hysteresis curves for NdFeB bonded magnets with different magnetic powder content showing the increase in Mr and Ms……. 91

Figure 4. 2 Changes in the magnetic properties with respect to the weight percent of (a) high-Nd and (b) low-Nd content powders in polymer matrix……..92

Figure 4. 3 (a) 3D printed bionic ear; first attempt to blend human tissue and electronics [136]; (b) a metal object printed by 3D systems cooperation; (c) a customized 3D printed knee replacement (right) as compared to a traditional knee implant (left) [137]; (d) a 3D printed architectural model [138]…….....94

Figure 4. 4 Schematic illustration of the experimental procedure……..…… 96

Figure 4. 5 Twin-screw extruder configuration and profile [143]..…… 97

Figure 4. 6 Photos of (a) Makerbot Replicator Mini and (b) custom made 3D printer converted from a CNC machine……..…… 98

Figure 4. 7 Photo of the extruder assembly showing the components of Makerbot Replicator Mini…….....99

Figure 4. 8 Photos of (a) PLA filament mixed with MnAl powders after extrusion and (b) spiral filament showing the color gradient…….……...……. 101

Figure 4. 9 SEM micrographs in (a) low and (b) high resolution showing PLA mixed with magnetic powders……..….....102

Figure 4. 10 High (a) and low (b) resolution SEM micrographs of the commercially available PLA/Fe filament……..……...… 103

Figure 4. 11 DSC curve of the commercial PLA filament used in 3D printing……104

Figure 4. 12 Photos of two prototypes printed using the custom made 3D printer.. 105

Figure 4. 13 Photo of the 3D printed block from Makerbot Mini, (b) 3D printed block from custom made printer…….....107

Figure 4. 14 Photo of the 3D printed magnetic propeller used in wheel speed detection both in marine applications and ground vehicles……..108

Figure 4. 15 (a) Hysteresis curve of MnAl powders alone and same powders encapsulated in PLA (b) Dependence of energy product on field strength…..…… 109

NOMENCLATURE

RE: Rare-earth

Br: Remanance

Tc: Curie Temperature

Ms: Saturation Magnetization

BH_{max}: Maximum Energy Product

XRD: X-ray Diffraction

DSC: Differential Scanning Calorimetry

HEXRD: High Energy X-ray Diffraction

VSM: Vibrating Sample Magnetometer

EDS: Energy Dispersive X-ray Spectroscopy

RE: Rare-earth Elements

SEM: Scanning Electron Microscopy

TEM: Transmission Electron Microscopy

HRTEM: High Resolution Transmission Electron Microscopy

STEM: Scanning Transmission Electron Microscopy

QSTEM: Quantitive Scanning Transmission Electron Microscopy

BF: Bright Field

DF: Dark Field

SADP: Selected Area Diffraction Pattern

3D Printing: 3 Dimensional Printing

CNC: Computer Numerical Control

PLA: Polylactide

ABS: Acrylonitrile Butadiene Styrene

CHAPTER 1

INTRODUCTION TO PERMANENT MAGNETISM

1.1. THE MAGNETISM

A permanent magnet is an object that exhibits strong magnetic field and retains its magnetization even after an external field is removed. When discussing the origin of magnetism, magnetic moments constitute a fundamental part. Permanent magnetism is a consequence of magnetic moments and magnetic moments originate from the motion of an electrical charge. A moving electron creates a magnetic field through its orbital and spinning motions.

Orbital motion is the motion of an electron revolving around nucleus creating a small current loop and generating a magnetic field. A spin magnetic moment is the magnetic moment induced by the spin of electrons along the spin axis. The net magnetic moment is theoretically the sum of orbital and spin moments. Net magnetic moment is mainly determined by the atomic magnetic moments due to electron spin. Orbital magnetic moment contribution is small in comparison to the spin moment. When an atom has all the electron shells filled, orbital and spinning cancel each other and net magnetic moment becomes zero.

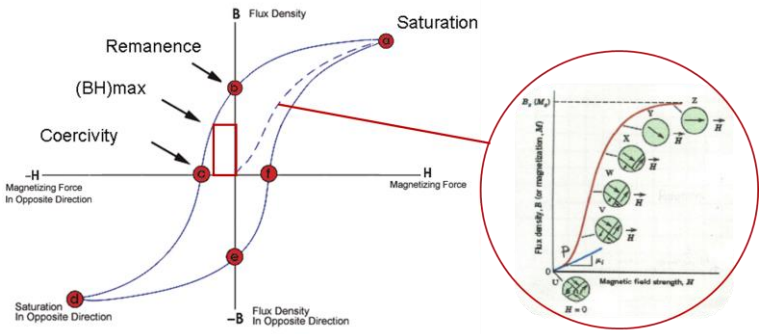

Figure 1. 1 Hysteresis loop of a permanent magnet and the stages in the alignment of magnetic moments.

Permanent magnetism is caused by the alignment of the magnetic moments. In most solids, magnetic moments are randomly arranged in the absence of a magnetic field. When disordered magnetic moments line up in the same direction due to the interatomic forces and coupling interactions in the electron structure, exceptional magnetic properties are observed and these materials are called as permanent magnets. Magnetic properties are best described by the hysteresis loops. Hysteresis loops are curves of flux density versus magnetizing force (Figure 1.1). When an external magnetic field (H) is applied, atomic or ionic magnetic moments align and magnetic domains are formed [1]. Magnetic domains are local regions having the same direction of the magnetization. The material divides itself into multiple small magnetic domains in order to minimize the magnetostatic energy. A single region creates a large magnetic field extending towards outside, requiring large magnetostatic energy in accordance. To reduce this energy, material splits into multiple domains with the magnetization in various orientations. With the motion of domain walls, magnetic domains of one direction grow at the expense of others. When all or most of the domains are aligned in the same direction, the whole object becomes magnetized in that direction and becomes a magnet.

Saturation magnetization (Ms) is reached when all the domains are in the direction of the external magnetic field and the entire solid becomes a single domain. After applied field (H) is removed, a certain flux density remains in a permanent magnet, known as remanence (Mr). The reverse field required to reduce the remaining flux density to zero is called as coercivity (Hc). Net magnetization is more or less independent of external magnetic fields. The strength of a permanent magnet is determined by the combination of these terms known as BH_{max}. BH_{max} is defined as the maximum area of the square that one can fit into the second quadrant of the hysteresis loop. Quality of a permanent magnet is expressed by the value of BH_{max}. Permanent magnets are most efficient at the BH_{max} value. The higher the BH_{max} the smaller the volume of the material needed to produce a certain magnetic field.

Alignment of the magnetic moments determine the magnetic behavior and shape of their hysteresis curves. Based on the response of moments to the magnetizing force, materials are classified as ferromagnetic, ferrimagnetic, antiferromagnetic, diamagnetic and paramagnetic [2]. Ferromagnetic materials retain their magnetism by possessing a net magnetic dipole moment even in the absence of a magnetic field. Moments of neighboring atoms spontaneously align in the same direction due to interatomic forces. Ferromagnetism is common among transition metals such as iron (Fe), cobalt (Co), nickel (Ni) and some rare-earth elements. For engineering applications, ferromagnets are classified as hard and soft. Alloys such as AlNiCo and ceramic magnets are called as soft, whereas NdFeB is one of the best example of a hard magnet. Ferromagnets find use in many applications due to their high permeability (high magnetic inductions can be obtained even under modest magnetic fields), their ability to retain magnetization enabling their use as a source of field. Antiferromagnetism and ferrimagnetism are subgroups of ferromagnetism. Antiferromagnetism appears when magnetic moments of neighboring atoms (or ions) hinges and results in an antiparallel alignment. The main difference between ferromagnetism and antiferromagnetism is the alignment direction of the two nearby magnetic dipoles. In ferromagnetism, magnetic coupling of adjacent atoms (or ions) takes place in the same direction however, the magnetic moments in antiferromagnetic materials tend to align in opposite directions. Ferrimagnetism occurs mostly in ionic compounds such as oxides. Like antiferromagnetism, adjacent magnetic moments lie in opposite directions. The opposite ordering would normally results in cancellation of the overall magnetic field. However, in case of ferrimagnets, microscopic differences in the crystal structure results in a net magnetic moment. The magnetic moments of the neighboring sublattices are not equal to each other and thereby permanent magnetism arises. Most of the oxides including magnetite possess ferrimagnetic properties. Diamagnetic and paramagnetic materials are both considered as nonmagnetic materials. Diamagnetic materials have no magnetic dipoles present in the absence of the magnetic field. However, when exposed to magnetic field, the magnetic moments align in the opposite direction to the applied field. Magnetism disappears

when the field is removed so this type of magnetism is nowhere near permanent. Similar to diamagnetism, magnetism persist only when an applied field is present in paramagnetic materials. Unlike diamagnetism, the magnetic moments inside are oriented in random directions due to unpaired electrons in partially filled orbitals. When an external field is applied, adjacent dipole moments align partially in the direction of the field. Upon removal of the field, dipoles revert back to random. Paramagnetism is therefore considered as temporary magnetism whereas diamagnetism is almost negligible. Superparamagnetism is a form of ferromagnetism which only appears in the single domain nanoparticles. Magnetization direction of the nanoparticle spontaneously changes due to thermal fluctuations [3]. Schematic atomic dipole configurations for paramagnetic, diamagnetic, ferromagnetic, ferromagnetic and antiferromagnetic materials are given in Figure 1. 2.

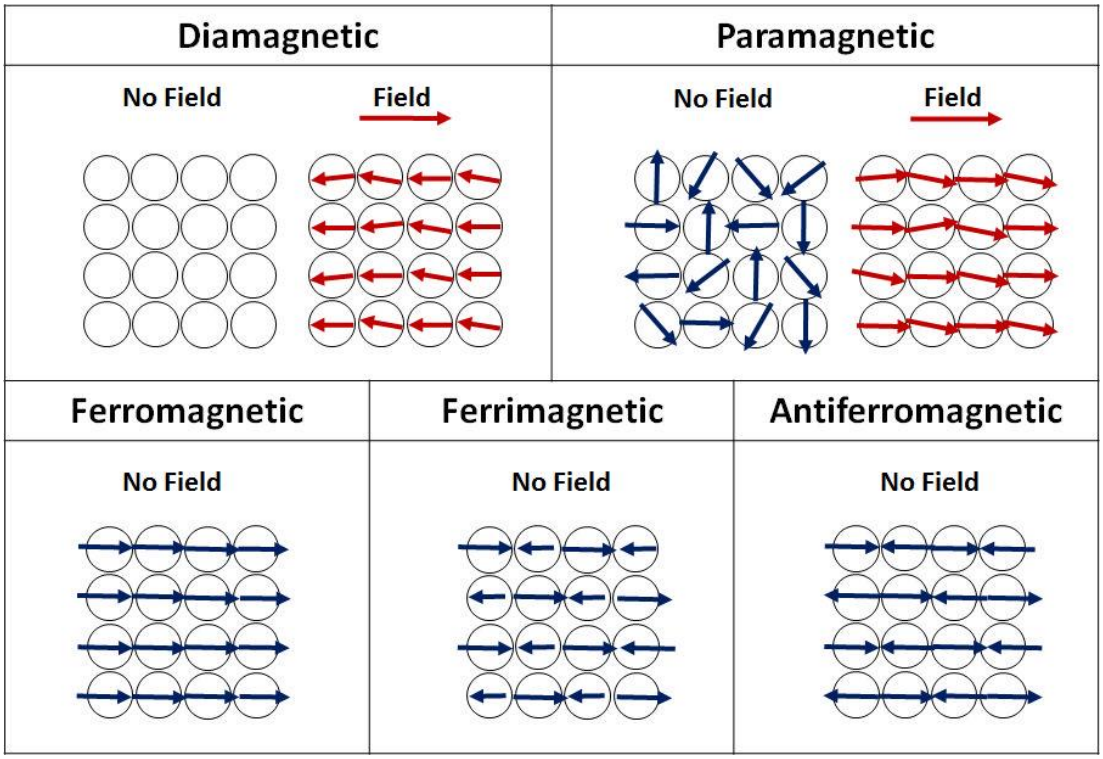

Figure 1. 2 The atomic dipole configurations for diamagnetic, paramagnetic, ferromagnetic, antiferromagnetic materials with and without magnetic field [2].

The alignment of the magnetic moments not only determines the magnetic behavior but also the shape of their hysteresis curves. Hysteresis of different magnetic materials are different than one another. Typical schematic hysteresis loops of diamagnetic, paramagnetic and ferromagnetic materials are provided in Figure 1. 3. Ferromagnets are difficult to demagnetize and thereby they have the highest BH_{max} and largest hysteresis. Diamagnets do not retain any magnetic property and repelled by a magnetic field which results in an almost linear line with negative slope. Paramagnetic materials also do not exhibit hysteresis behavior, but slightly attracted by a magnetic field.

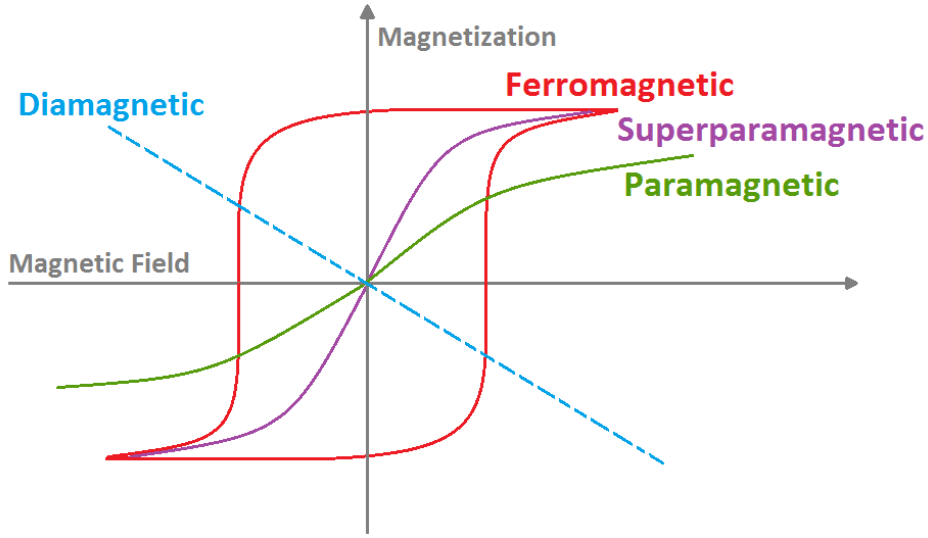

Figure 1. 3 Typical schematic hysteresis loops for diamagnetic, paramagnetic, superparamagnetic and ferromagnetic materials.

As magnetism is caused by the alignment of the magnetic moments, magnetic properties are not only intrinsic but also extrinsic. Critical extrinsic magnetic parameters for permanent magnet applications are;

- coercive force/field *H*c,
- remanence induction *M*r, (*Br* residual flux density)
- maximum energy product BH_{max}, (squareness of the loop)

The extrinsic properties of a material reflects the magnet's real-structure and dependent on the details of the chemical and topological microstructure [4], [5] Judging solely by the extrinsic properties, it is obvious that key requirements for permanent magnets are a high remanent magnetization (Mr), a high coercivity (Hc) and a nearly square hysteresis loop shape so that a large flux density would be remained after magnetization and the influence of externally applied field is minimized. Intrinsic properties, on the other hand, are related to the crystal structure of the material and can be defined as;

- Saturation magnetization (M_s)
- Curie temperature (T_c)
- Magnetocrystalline anisotropy [5].

The temperature at which the ordered magnetic moments become disordered due to thermal effects, known as the Curie temperature (T_c). A ferromagnetic/ferrimagnetic material becomes paramagnetic at temperatures beyond T_c. Ferrimagnetic materials have lower Curie temperatures than ferromagnetic materials.

Magnetocrystalline anisotropy is defined as the dependence of magnetic properties on the crystal direction. The energetically favorable direction at which magnetic moments readily align is called as the easy axis. In the absence of an easy axis (magnetic anisotropy), the moments have no specific preferred direction unless a magnetic field is applied and act as a paramagnetic material. Thereby, magnetic anisotropy is an essential property for ferromagnetism [6].

To sum up, if a ferromagnetic material has large Br (remanence) and Hc (coercivity) combined with a high Curie temperature (T_c) and magnetic anisotropy, it is considered to be a good candidate for a permanent magnet [7].

1.2. HISTORY AND APPLICATIONS OF COMMERCIAL PERMANENT MAGNETS

The history of permanent magnetism dates back to 600 B.C with the discovery of lodestone, a variation of magnetite (Fe_3O_4). The first man-made permanent magnets were iron needles magnetized by lodestone. They were long called "artificial permanent magnets" to distinguish them from the natural loadstone. The first fundamental description of magnetism is given by William Gilbert in 1600. Artificial magnets have been used and studied from that day on; however the first major improvement in magnetic materials took place almost after 300 years.

With the invention of electromagnets, permanent magnets gained significant importance and steel permanent magnets were developed in the beginning of 1900s. Tungsten and/or chromium is added to the iron-carbon alloys and it is observed that the resulting carbide precipitates prevented the domain wall movement and improved the magnetism under appropriate heat treatments. However, there were problems with the stability carbon steel magnets and they only had an energy product of about 2.5 kJ/m^3. If the carbon steel is alloyed with cobalt, it is observed that the energy product increased up to 8 kJ/m^3. This finding draw attention to the cobalt alloys and AlNiCo alloys were developed in the 1930s.

Modern commercialized permanent magnet as we know begins with metal magnets (also known as AlNiCo) and today, literature contains a wide variety of permanent magnet materials with different characteristics. They can be classified in three main classes each based on their material composition as shown in Figure 1. 4.

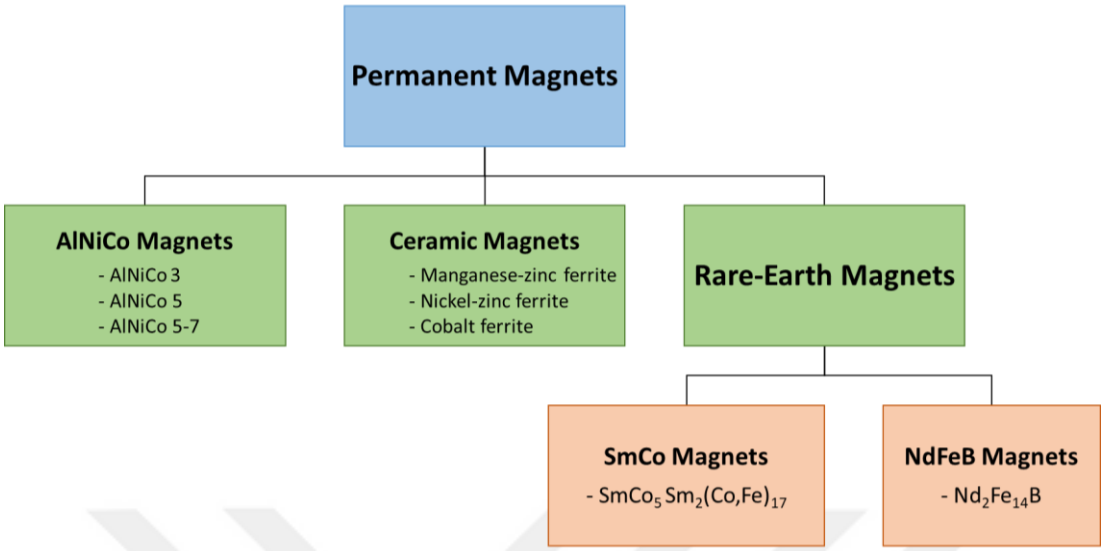

Figure 1. 4 Types of commercialized permanent magnets.

As the name implies, AlNiCo magnets are iron alloys with main additions of aluminum, nickel and cobalt. Discovery of AlNiCo alloys was a major technological achievement as they were able to replace electromagnets in devices such as generators and electric motors. Their T_c was high, so that they have excellent temperature resistance for demagnetization. AlNiCo magnets have high remanent force (Br) and good corrosion resistance [8]. However; they can be easily demagnetized due to their low coercivity. The strategic locations and scarcity of Co also created a problem for these magnets. Overall, AlNiCo alloys are a good combination of high saturation magnetization and good temperature stability.

In 1940s, ferrite magnets became the preferred choice over AlNiCo due to the low cost and large availability of raw materials. Ferrite magnets, also known as ceramic magnets, are categorized as soft ferrites and hard ferrites in terms their magnetic coercivity. The most common soft ferrites are manganese-zinc and nickel-zinc ferrite. Hard ferrites have relatively high coercivity and high remanence and best known examples are cobalt ferrite, strontium ferrite and barium ferrite. They are usually manufactured by die pressing, followed by sintering. The coercivity is relatively high thereby they have strong resistance to demagnetization. Ferrite magnets have excellent

corrosion resistance. However, like all ceramics, ceramic magnets are brittle so that their machinability is difficult and the mechanical strength is low. Major drawbacks exist in the key extrinsic properties which characterize permanent magnets. For instance, the remanence is considerably lower than that of metallic materials and energy product BH_{max} is not as high as in AlNiCo magnets. It is these aspects that made the researchers look for a new and stronger magnetic material that can be produced at a reasonable cost.

Neodymium iron boron (NdFeB) and samarium cobalt (SmCo) magnets, collectively known as rare-earth magnets, have been the focus of research due to the increase in the demand for highly coercive permanent magnets. They are composed of materials from the rare-earth group of elements, neodymium and samarium are known to be the most powerful and strongest permanent magnets commercialized, substantially stronger than ferrite or AlNiCo magnets. Rare-earth materials provide sufficient flux density at high values of magnetizing force [9].

Samarium cobalt magnets were introduced in early 1970s. Its main characteristic is the high magnetic strength - up to about 32MGOe and high working temperature up to 350 °C [10]. SmCo magnets are very suitable for the manufacturing of a variety of high-performance permanent magnet motors as well as for complex applications. It's fairly high magnetization is due to the presence of Co ions. Increasing the Co content causes a reduction in *B,* and an increase in H_c with an overall increase in energy product [11].

The high anisotropy produces very narrow walls between domains, which are easily pinned and this leads to high coercivity. In addition, SmCo magnets are very corrosion resistant and thus their surface do not require an electroplating treatment. However, their applications are limited by considerations of cost. A large proportion of cobalt sources are in politically sensitive areas and their availability is subject to changes in the world's political climate. In addition, due to low Sm reserves on earth, it is an

expensive material. They are also very brittle magnets and hence prone to cracking and chipping which makes SmCo magnets not suitable for machining.

SmCo magnets have largely been supplanted by the invention of a new material for permanent magnets on a base of Nd and Fe in 1984. Sumimoto [12] and General Motors [13] simultaneously announced the development of $Nd_2Fe_{14}B$ magnet, which rapidly solidified, have excellent magnetic properties and can be produced at a reasonable cost. NdFeB magnets are classified into two groups as bonded [14] and sintered [15] depending on their production method. The alloy consists of Fe, B and Nd and Nd is a rare-earth element.

The Sumimoto magnets are fabricated through sintering the aligned powders. Sintered Nd-Fe-B magnets are produced first by pulverization of an ingot precursor, followed by sintering the magnetically aligned powder. Afterwards, sintered blocks were heat treated, cut to shape, surface treated and finally magnetized.

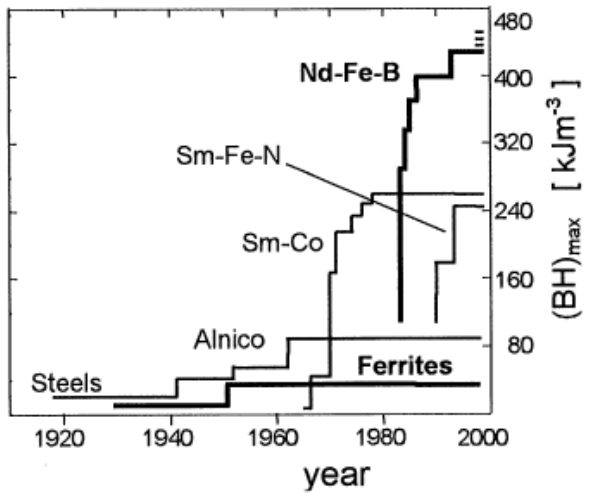

Figure 1. 5 Maximum achieved energy density BH_{max} of permanent magnetic materials in the 20th Century showing how BH_{max} has improved exponentially [16].

General Motors magnets are fabricated by hot pressing of melt-spun ribbons. Bonded Nd-Fe-B magnets are prepared by melt spinning Nd-Fe-B ribbons. The ribbons contain randomly oriented small grains of $Nd_2Fe_{14}B$. Following melt spinning, the ribbon is

pulverized into particles, mixed with a polymer and either compression or injection molded into bonded magnets. Bonded magnets provide less flux than sintered magnets but can be formed into intricately shaped parts. In addition, it is possible to hot press the melt spun nanocrystalline particles into fully dense isotropic magnets, and then upset-forge/back-extrude these into high energy anisotropic magnets. This technique has attracted commercial interest due to the anisotropic behavior of the final product [17]. There are approximately 5,500 tons of bonded Nd-Fe-B magnets produced each year.

Nd-Fe-B magnets are currently the strongest known type of permanent magnet. These magnets have been the focus of research for almost 30 years. The highest value of the energy product (BH_{max}), which is considered to be the most important extrinsic property, has so far been achieved for $Nd_2Fe_{14}B$-based magnets (Figure 1. 5). Table 1. 1 represents a summary of the coercivity, remanence, BH_{max} and Curie temperature values of the well-known already commercialized permanent magnets.

Table 1. 1 Magnetic properties of permanent magnets [9].

Magnet Types	**Magnetic Properties**			
	Hc (kA/m)	**Br** (T)	**BH_{max}** (kJ/m^3)	**Tc**(°C)
Steel	4	0.9	1.6-8	500
AlNiCo	18-25	0.7-1.2	13-60	900
Ceramic (Ferrite)	160-400	0.4	30-50	450
$SmCo_5$	600-2000	0.9-1.1	160	800
$Sm_2(Co,Fe)_{17}$	450-1300	1.1	260	800
Sintered Nd-Fe-B	750-2000	1	320-400	300
Bonded Nd-Fe-B	500-1200	1.4	320-400	300

Today, permanent magnets are an important part of our daily lives, serving as essential components in almost everything spanning from consumer products to large systems utilized in transport, medicine and military [18]. There has been an increasing use of permanent magnet materials as the properties of these materials have been improved over the years. Soft permanent magnets are usually used in applications that require low coercive field. Their high permeability and small hysteresis loss makes them truly attractive for use in the cores of transformers, motors, generators and magnetic recorders [19]. Hard magnets have high coercivity and high remanence thereby used in applications that needs rather high magnetic force. Neodymium Boron Iron alloys are nearly ideal for use in electric motors, generators (wind turbines, turbo generators), loudspeakers, magnetic separators, MRI devices, sensors, headphones and microphones. As the magnetism of NdFeB alloys is very strong, even the smallest magnets are sufficient to obtain the required force for most of the applications. The relatively low cost per unit weight combined with a high energy product leads to a decrease in the overall cost and volume needed for the machine. The compactness of the required volume makes this type of magnets desirable in many ways. Especially in the past 20 years, there has been an extensive demand for rare-earth permanent magnets due to their essential role in many applications from cell phones to batteries, motors and generators to national defense and the high-tech field. The fact that they can reach high torque values under magnetic field is especially beneficial for their use in electric motors. The exciting combination with microcomputers and power electronics makes the permanent magnet motors attractive for drives requiring smooth synchronous operation, constant torque and constant power characteristics [20]. These materials are readily machinable and can be easily manufactured into the desired shape.

Some other high tech applications include nanoparticle ferrofluids for cancer treatment, guided by a magnet and delivering high local doses of drugs or radiation [19], micro-electromechanical systems (MEMS) and nanoscale magnetic-force nanotips made from platinum cobalt (PtCo) [21], [22].

1.3. PROBLEM DESCRIPTION AND OBJECTIVE OF THE STUDY

There is a growing demand for permanent magnets with better coercivity and magnetic flux and thereby, it is essential to improve the alloy design and processing of permanent magnets. NdFeB and SmCo magnets, being the most powerful permanent magnets, are today's most commonly used and studied alloys. They consist of rare-earth elements such as Sm and Nd. Rare-earth element deposits are located mostly in Mongolia and south of China. There are also some deposits in (Mountain Pass) United States, India, Brazil and South Africa. Even though Turkey has some potential rare-earth element reserves in Eskisehir, there has been no sign of evidence of either extracting or processing these ore deposits. During 1960-1990, United States was dominating the market with the reserves in Mountain Pass. However; in 2002 it was shut down owing to severe environmental problems and the emergence of Chinese producers that supplied these metals at a lower cost. Today, worldwide rare-earth mineral trade is under monopoly of China, which is currently holding up 97 % of the rare-earth mineral industry.

While countries are increasingly becoming dependent upon this metal, the world supply of rare-earths is becoming more and more dependent on China. The rare-earth element crisis started in 2010 when China announced that they would significantly restrict their rare-earth exports to ensure a supply for domestic manufacturing and for environmental reasons. This announcement triggered extensive bulk import and rare-earth prices increased exponentially accordingly. Rare-earth element quota of production and import from China in between 2005 and 2015 is shown in Figure 1. 6.

Figure 1. 6 Evolution of Chinese rare-earth element supply and demand, export quotas from 2005 to 2015, in metric tones [23]

In less than 12 months, costs of some rare-earth oxide materials experienced increases ranging from 500% to more than 2000%. The increase in the prices of some rare-earth oxides from 2009 to 2011 due to the decrease in export quota are given in Table 1. 2. Among these elements, the increase in the price of Nd is especially significant considering that the element is mainly used in Nd-Fe-B magnets.

Table 1. 2 Sales prices of some rare-earth oxides in 2009 and 2011 [24]

	2009 (Sales Price/Kg)	August 2011 (Sales Price/Kg)
Lanthanum Oxide	$4.88	$117.68
Cerium Oxide	$3.88	$118.65
Neodymium Oxide	$19.12	$338.85
Disporsium Oxide	$115.67	$2262.31
Europium Oxide	$492.92	$4900.00
Terbium Oxide	$361.67	$3761.64

As the prices for rare-earths continued to increase in line with the growing demand, China's near monopoly in production become a more than serious threat to the buyers. Due to the strategic importance of the rare-earth element reserves and political issues governing these elements, there has been an effort to minimize the use of rare-earths or to completely substitute rare-earth elements with other ones.

Once the magnetic properties of the RE and RE-free permanent magnets are compared, the gap between the maximum energy product (BH_{max}) values between these two types of materials become evident (Table 1.1). Although it may have been challenging to substitute the rare-earth permanent magnets, it is still possible to improve a rare-earth free permanent magnet in order to fill the gap. In this study, two permanent magnet alloys without any rare-earth elements are investigated.

The first approach is to choose a conventional, already-commercialized alloy (AlNiCo) and improve its magnetic properties. When BH_{max} values are considered (Table 1.1), the closest successor of rare-earth magnets are AlNiCo alloys [25]. Provided that the coercivity of AlNiCo is improved, it is likely that it may fit into the gap. AlNiCo permanent magnets have been widely used since 1920's; but, has not been thoroughly studied after 1950s. In this research, AlNiCo magnets are revisited using novel production methods and latest analysis techniques.

Similar to many other alloy systems, magnetic materials exhibit unique properties at nano length scales many of which have still been remained unsolved. Especially in case of AlNiCo systems, there is little or no information on the behavior of nanoscale magnets. It has been aimed to reduce FeCo content in NiAl matrix and sharpen chemical gradient at the interface. By producing narrower and more regular array of nanoprecipitates, coercivity will likely be increased through shape anisotropy. Enhanced control of microstructure and improved coercivity is the aim of this part of the study.

The second approach is to investigate a relatively new and promising composition without rare-earth elements that hasn't been commercialized so far. First characterized

in 1958, manganese-aluminum (MnAl) alloys did not receive much attention until more recently when rare-earth supply crisis made it more attractive for commercial applications. Its magnetism arises from a ferromagnetic τ-phase with high and uniaxial magnetocrystalline anisotropy with an "easy" *c*-axis. By increasing the amount of τ-phase and having a better understanding of the ε-to-τ phase transformation, it is possible to improve the magnetic properties of the alloys.

CHAPTER 2

SYNTHESIS OF ALNICO CORE/SHELL NANOPOWDERS

2.1. INTRODUCTION

Aluminum-nickel-cobalt (AlNiCo) permanent magnets revolutionized the permanent magnet industry in 1920's but has not been thoroughly studied after the development of powerful rare-earth permanent magnets. They have high remanent force (Br), better corrosion resistance and higher Curie temperature as compared to rare-earth magnets but lack high coercivity [8]. If the coercivity is improved, BH_{max} value may increase up to values that would potentially fill the gap in between rare-earth and rare-earth free permanent magnets. The alloy stands as a good candidate to be produced with novel methods and investigated with the latest analysis techniques. It is now well established that magnetic behavior is strongly dependent on the size of the nanoparticles.

In this chapter, it is aimed to decrease the particle size of AlNiCo powders as close to dimensions between the critical diameters of single-domain and superparamagnetism range while creating a protective ferromagnetic oxide layer to get the advantages of the effective exchange coupling between the core and the corresponding shell structure. Magnetic properties of micron-size ball-milled powders and radio frequency (RF) plasma synthesized core-shell nanopowders are compared. The magnetic measurements indicated that coercivity increased significantly with decreasing particle size, particularly for the nanopowders encapsulated with hematite (Fe_3O_4) layer. It is likely that this oxide coating contributes to the increase in coercivity due to effective exchange coupling between the core and the shell structure. In addition, it serves as a protective layer against room temperature oxidation.

2.2. AlNiCo PERMANENT MAGNETS

First developed by Mishima in 1931 [26], AlNiCo magnets are among the oldest commercially available magnets. Alloys of Fe with Al, Ni and Co represent a good candidate as a substitute to rare-earth magnets given their high remanent force (Br), Curie temperature and good corrosion resistance.

The conventional AlNiCo magnet consists of α1-α2 duplex phase structure formed due to a spinodal decomposition reaction during the solidification process. Among these two, α1 is the FeCo-rich magnetic and α2 is the NiAl-rich non-magnetic phases, respectively. FeCo precipitates decompose along {001} planes in NiAl-rich matrix and preferentially grow parallel to a magnetic field. Typical spinodal phase morphology of AlNiCo 5-7 alloy is shown in the TEM images provided (Figure 2. 1). Dark regions correspond to FeCo-rich phase, whereas the bright regions are NiAl-rich phase in the TEM dark field image (Figure 2. 1b). In most of the commercial applications, the grains are purposely textured along an applied magnetic field through a thermomagnetic treatment in order to enhance the magnetic properties [27].

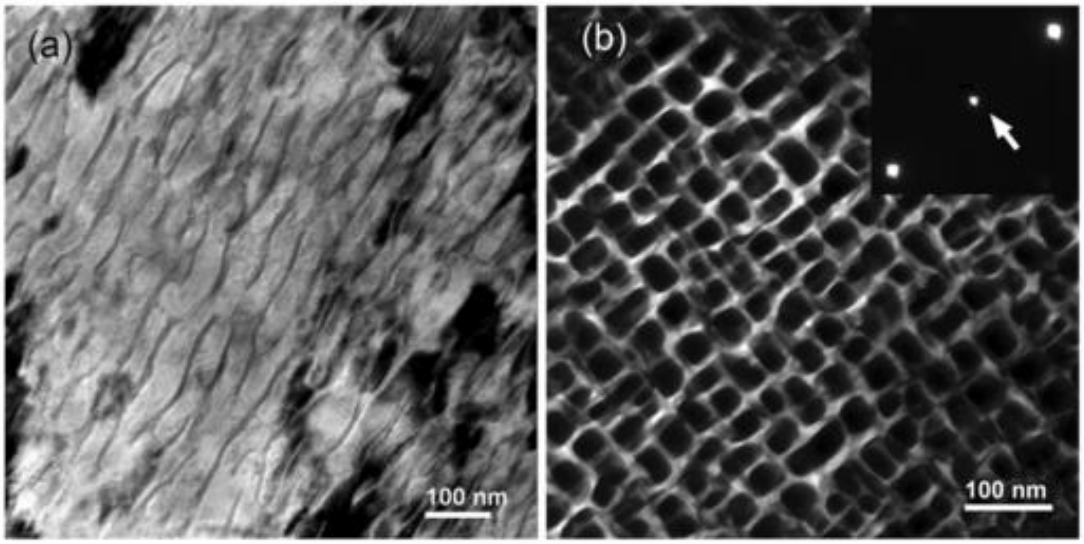

Figure 2. 1 (a) Bright field micrograph in longitudinal view, (b) conventional dark field image in transverse view of AlNiCo 5-7 [28].

AlNiCo magnets are manufactured by primarily two processes:

1. Cast AlNiCo magnets are fabricated by pouring melted AlNiCo into a mold. After grinding the solidified ingot, it is heat treated and cooled. The material can be treated in a magnetic field to make anisotropic or made isotropic by a treatment outside the magnetic field.

2. Sintered AlNiCo magnets are made by pressing powders into a die under pressure. They are then sintered in a hydrogen atmosphere and cooled in an anisotropic or isotropic environment.

The resulting magnet is extremely hard and brittle and difficult to machine. Their energy product (BH_{max}) is only about 10 kJ/m^{-3} and they have low Hc values, meaning that they are easily demagnetized [29]. Cast AlNiCos often have casting pores and voids within them, which can be problematic because large voids may lower expected magnetic flux.

AlNiCo alloys have high Tc, meaning they can preserve their magnetic properties even at extremely high temperatures (as high as 900°C), which makes them desirable for many applications. Among all of the permanent magnets, AlNiCo alloys have the lowest reversible temperature coefficient due to the presence of Co element with high Curie temperature, increasing the Curie temperature of the alloy. Permanent magnet stability of AlNiCo alloys can be maintained up to 550°C [30].

The main limitation of AlNiCo magnets is their low coercivity resulting in easy magnetization reversal [31]. Magnetization reversal process is known to start at imperfections (defects) in materials whether in the form of dislocations, impurity elements, compositional defects or stresses. These defects serve as nucleation sites for magnetization reversal [8]. As the number of these defects decreases, nucleation slows down and magnetic properties are preserved for longer periods. Therefore, major defects must be isolated and material should be divided into fine domains.

Microstructure of nanoparticles are less prone to these defects; thereby, the coercivity of ultrafine magnets increases with the decrease in particle size.

2.3. MAGNETIC NANOPARTICLES

Primarily attributed to their appealing physical and chemical properties due to the reduction in size, magnetic nanoparticles have been the center of attention for several decades. The size of the nanoparticle helps in defining the nanoparticle's magnetic behavior and the relationship between magnetic properties and particle size is already well established in literature [32]. It is observed that at a given particle size range it is possible to increase the coercivity by decreasing the particle size. For instance, coercivity of elongated Fe particles having a diameter of 150 Å is 104 times that of the Fe in bulk form [33]. As illustrated in

Figure 2. **2**, maximum coercivity can only be achieved within a given size range. As grain size increases, coercivity decreases as the grain subdivides into multi domains. For ultrafine particles, coercivity is again low due to randomizing thermal effects and becomes superparamagnetic [34].

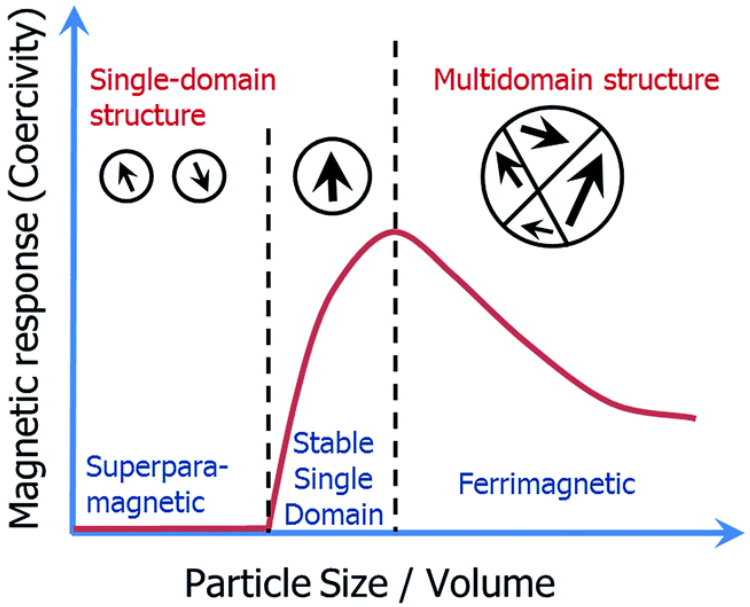

Figure 2. 2 Change in magnetic response (coercivity) with respect to the particle size [35].

Domain size is determined by the magnetocrystalline anisotropy as already defined in Chapter 1.1. Magnetocrystalline anisotropy (energy for stabilizing a magnetic moment in a certain orientation) decreases with decreasing particle size [36]. Similar to many other alloy systems, magnetic materials tend to lower their internal energy by creating an interface (domain wall) and separating into multiple domains. A uniformly magnetized, single domain material have surface charges as shown in Figure 2. 3a. This creates a large magnetic field which extends outside the material acting as a demagnetizing field. A configuration as such requires a lot of energy associated with the surface charge distribution (magnetostatic energy) and thus, becomes unstable.

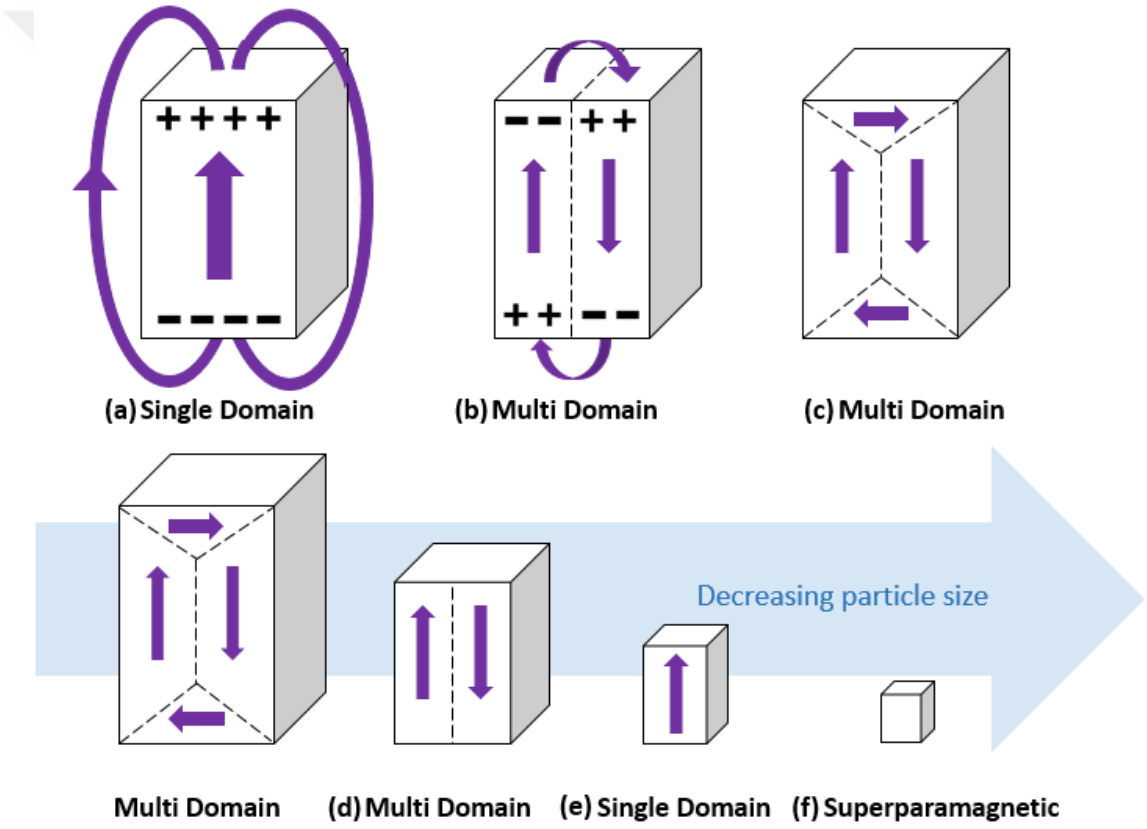

Figure 2. 3 Schematics of (a) a single large domain structure with extended large magnetic field, (b) Two domain structure with magnetic dipoles at opposite directions reducing the field outside, (c) Stable multi domain structure, where small parallel domains have magnetization in alternating directions, (d) A smaller grain, which can only hold two domain structure, (e) Uniformly magnetized single domain, f) Superparamagnetic structure, where domain boundary can no longer fit.

In order to lower the magnetostatic energy, large single domain would split into multiple domains magnetized in opposite directions as illustrated in Figure 2. 3b. A domain wall in the middle is created and this brings positive and negative charges close together, thus decreasing the field outside the material. Best configuration is shown in Figure 2. 3c, where it further divides into smaller parallel domains with magnetization in alternating directions.

However, this subdivision into multiple domains cannot continue indefinitely since creating an additional domain wall requires extra energy. Thereby, the overall energy reduction due to the domain splitting can be calculated by subtracting the energy of the domain boundary from the saved magnetic field energy. Eventually an equilibrium number of domains will be reached for a given particle size.

As the particle size decreases, the equilibrium number of the domains in a particle also decreases as shown in Figure 2. 3d. At a certain threshold size, grain becomes sufficiently small so that it can no longer accommodate domain walls and becomes a single domain, as shown in Figure 2. 3e. The moments of a single domain particle is aligned in one direction and uniformly magnetized to its saturation magnetization. This configuration is energetically favorable and has the maximum coercivity.

With further decrease in size, anisotropy energy balances with the thermal energy. This enables random flips of the magnetic moment, which in turn causes loss of magnetization due to thermal fluctuations. Material becomes superparamagnetic and do not possess any magnetic behavior (Figure 2. 3f). Depending on the desired application, properties of the magnetic particles can be altered from ferromagnetic to superparamagnetic by changing the particle size.

2.4. PLASMA SYNTHESIS OF MAGNETIC NANOPARTICLES

Interest in nanoparticles gave rise to widespread research and developed extensive variety of methods for nanopowder synthesis. Generation of fine powders can be achieved by homogeneous nucleation in gaseous state [37]. Several techniques include

furnace flow reactors, laser reactors, laser vaporization of solids, flame reactors, plasma reactors, spark source and exploding wire, sputtering, inert gas condensation and expansion-cooling [38].

Among many synthesis methods of ultrafine particles, plasma methods have gained interest over the past years. Plasma is a partially or fully ionized gaseous state of matter having free electrons and positive ions at extremely high temperatures. Due to its loose electrons, plasma easily conducts electricity and responds to magnetic fields. Plasma in material processing can either be thermal or non-thermal depending on the temperature.

In non-thermal (cold) plasma, material is exposed to low temperature and pressure. It is also called as "non-equilibrium plasma" since the temperature of the electrons is greater than the temperature of the heavy particles such as ions and neutrals.

On the other hand, in thermal plasma, system is in thermodynamic equilibrium as the temperature of the electrons is equal to the temperature of the heavy particles. Extremely high temperatures enable fast decomposition and leads to production of highly pure nanopowders. The overall process doesn't yield large amounts of waste. High intensity arcs (alternating current (AC) and direct current (DC)) between electrodes, microwave discharges and inductive coupling of radio frequency (RF) energy are some methods that can be used to generate thermal plasmas [39].

RF torches in particular, have attracted much attention due to a wide range of material precursors. Reactive gases, liquids and suspensions can all be used in addition to the solid powders [40]. Radio frequency electrical supply creates a magnetic field which then reacts with partially ionized central gas and generates the inductively coupled plasma. The diameter of the discharge changes with respect to the power conditions. Torch power smaller than 100 kW results in particles with diameters of ~20 – 30 mm whereas higher torch power (> 100 kW) results in the formation of particles with diameters 50 – 100 mm [41].

The method RF induction coupled plasma has some advantages over the alternative techniques. Plasma temperatures may reach up to 20,000 K and it is possible to reach a heating rate on the order of 10^6 K/s within a torch power of 20-60 kW [42]. This energy enables evaporation and chemical reactions necessary to obtain a wide variety of high purity ultrafine particles. The method can be readily applied to larger scale operations. Unlike DC systems, RF induction coupled plasma are not equipped with an electrode. This technique can be used for nanoparticle synthesis of pure metals as well as alloys and intermetallics. For example, pure Fe nanoparticles can be produced using RF coupled plasma under atmospheric pressure [43]. Relatively larger powders of pure Fe are fed into the plasma to synthesize Fe nanopowders with sizes of 20-70 nm. It is observed that the particle size get coarsened with increasing feed rate. In a similar study, silver nanoparticles are produced using DC arc plasma and the effect of the gas type on the particle size is investigated. The size of the particles are found to be in the range of 20-50 nm when Ar or He is used during production. And when these gases are used in combination, the particle size increased to 20-150 nm [44].

While particle size is the only parameter of concern in the synthesis of pure metals, the stability of the composition becomes an important factor in alloy production. Different compositions result in different reactions during plasma and may result in the formation of unconventional phases. Thereby, process parameters such as feed rate, gas composition must be changed and optimized accordingly in addition to the alloy composition.

To the best of our knowledge, AlNiCo nanoparticles has been investigated by hydrogen plasma-metal reaction method in only one particular study by Li and coworkers [45]. First developed by Ohno and Uda, hydrogen plasma-metal reaction (HMPR) method is commonly used in metallic nanoparticle production at industrial scale [46]. In the HMPR method, nanoparticles are synthesized by DC thermal plasma in a gaseous mixture of Ar and H_2. In addition to the metals, oxides, intermetallics, alloys and nanoparticles with a surface coating can be prepared by this technique [47].

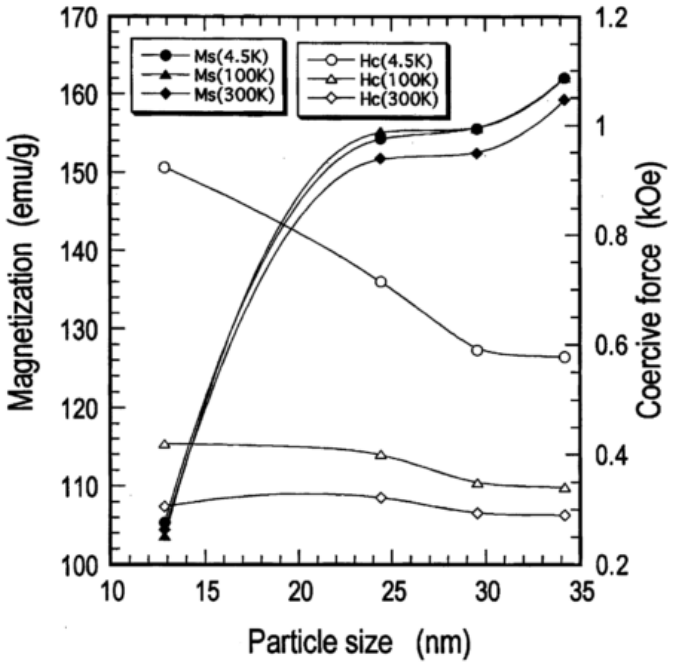

Figure 2. 4 The relationship between saturation magnetization and coercivity with respect to the mean particle size diameter for AlNiCo 5 alloys [45].

Li and coworkers [45] synthesized AlNiCo 4 and AlNiCo 5 nanoparticles with mean particle diameters of 12 to 34 nm, respectively, by hydrogen plasma metal reaction. The nanoparticles are heated in differential scanning calorimetry (DSC) and their oxidation behavior is investigated. The oxygen content is found to increase with decreasing particle size. Their results indicated that as the mean particle size increases, saturation magnetization and oxidation temperature decreases, whereas the coercivity is improved (Figure 2. 4). The increase in coercivity is attributed to the large number of single domain nanoparticles and the decrease in saturation magnetization is explained by the oxidation of nanoparticles.

2.5. CORE/SHELL STRUCTURED NANOPARTICLES

Research on nanoparticles is gained a new dimension following the emergence of composite (core/shell) nanoparticles in 1980s [48], [49]. Recently, there has been a gradual increase in demand for such advanced core/shell magnetic nanomaterials with

remarkable properties with increased coercive field [50], better thermal stability [51] and tunable exchange bias fields [52]. Among the commercial permanent magnets, core/shell structured AlNiCo alloys have not been thoroughly investigated.

These nanoparticles consist of an inner material (core) and an outer layer (shell) with modified chemical compositions and/or structures. Schematic illustration of a typical core/shell particle is given in Figure 2. 5.

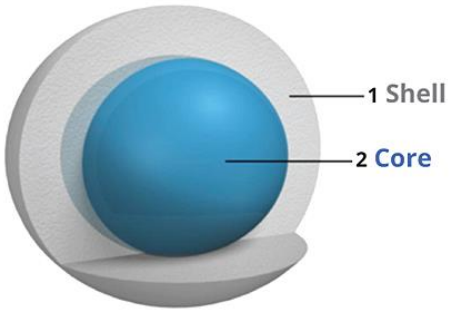

Figure 2. 5 Schematic illustration of a core/shell structure.

By changing either the constituting materials or the volume of the core/shell ratio, core/shell nanoparticles can exhibit enhanced properties with significant surface functions [53]. The shell is particularly used for surface modification and stability in order to create functional materials [54]. Several different types of ceramics and metals are frequently used as shell materials. Silica, for example, is a popular choice because of its superior thermal and chemical stability [55]. Metals such as Au [56], Ni [57], Co [57], Cu [58] and metal oxides [59] are commonly used as the shell materials. Core/shell nanoparticles composed of a metal and an oxide layer are frequently reported in literature by employing coating methods of gas or liquid phase reactions [60], [61]. Liu and coworkers [62], for example, synthesized Fe_3Al nanoparticles by the hydrogen plasma– metal reaction method and studied the oxidation behavior of the intermetallic nanoparticles, changes in morphology, particle size and crystal structure. It is observed that the synthesized nanoparticles are stable both in shape and structure at 473 K when Fe nanoparticles are covered with an Al oxide layer. Developing such core/shell nanostructures has a great promise to create materials used in diverse

engineering applications. Large specific surface area and surface activity, chemical stability, uniformity in size made them particularly attractive in pharmaceuticals [63], magnetic resonance imaging [64], [65], microwave absorbers [66] and magnetic applications [67], [68]. Magnetic core/shell structures have particularly received much interest due to their multi-fuctionality in drug delivery systems, clinical cell labeling, catalysts, ferrofluids, magnetic storage media and permanent magnets [69].

Pure magnetic nanoparticles without any shell layer have a tendency to aggregate and oxidize. In order to increase their stability and reduce the aggregation probability, many magnetic nanoparticles are produced in the form of core/shell structures. The magnetic properties of the nanoshell structures can be tailored by controlling the dimensions and chemical compositions of both core and shell layers [68]. The magnetic core can be coupled with a non-magnetic, antiferromagnetic or ferro/ferri-magnetic shell materials. In core/shell systems, where both core and shell are strongly magnetic (ferro- or ferri-magnetic), the intimate contact between the core and shell leads to an effective exchange coupling and cooperative magnetic switching. This facilitates the fabrication of nanostructured magnetic materials with tunable properties [68].

2.6. AlNiCo 5-7 POWDER SYNTHESIS

2.6.1. Production of Alloys

The master alloy, $Fe_{51}Al_{8.5}Ni_{14.5}Co_{24}Cu_3$, is prepared using copper-heart Edmund Bühler electric arc furnace under Ar atmosphere from highly pure Fe (99.97 wt%), Al (99.9 wt%), Ni (99.95 wt%), Co (99.9 wt%) and Cu (99.9 wt%) beads (Figure 2. 6). The melting process is repeated three times to ensure homogeneity. Final compositions of the alloys are verified using X-ray spectroscopy.

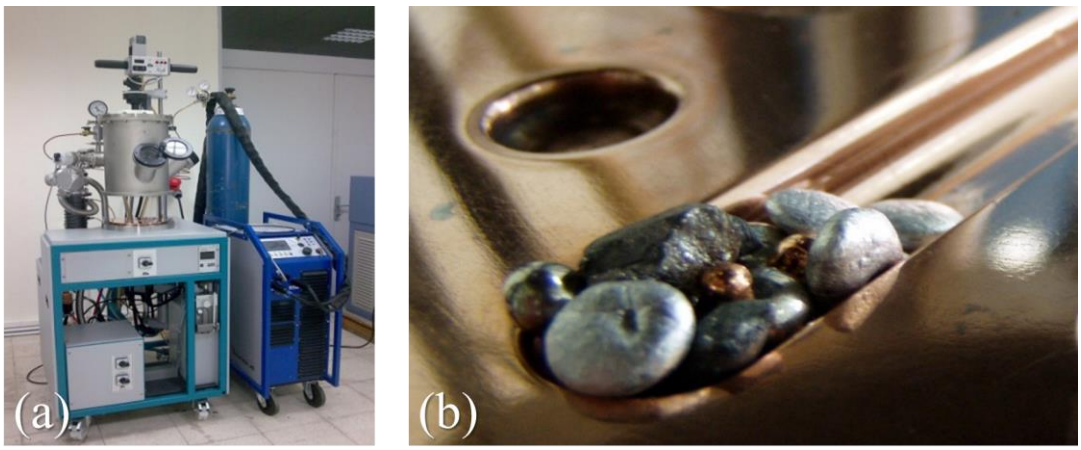

Figure 2. 6 Photos of (a) Edmund Bühler arc-melter used for the preparation of samples (b) Pure elements inside the chamber before melting process.

2.6.2. Mechanical Milling

Arc-melted ingots are crushed into pieces using a mortar and pestle following N_2 freezing. After obtaining powders of a suitable size range to be fed into a Fritsch ball mill, the powders are pulverized using stainless steel balls. Milling rate is optimized according to the particle size distribution. D50 and D90 are the most commonly used metrics when describing particle size distributions. D50 and D90 are the intercepts for 50% and 90% of the cumulative mass, respectively. Particle size distribution and D values are measured using Malvern Mastersizer 2000 particle size analyzer. D50 and D90 values for various milling conditions are shown in Figure 2. 7. Tests are repeated 3 times and the error bars represents 95% confidence interval of the mean.

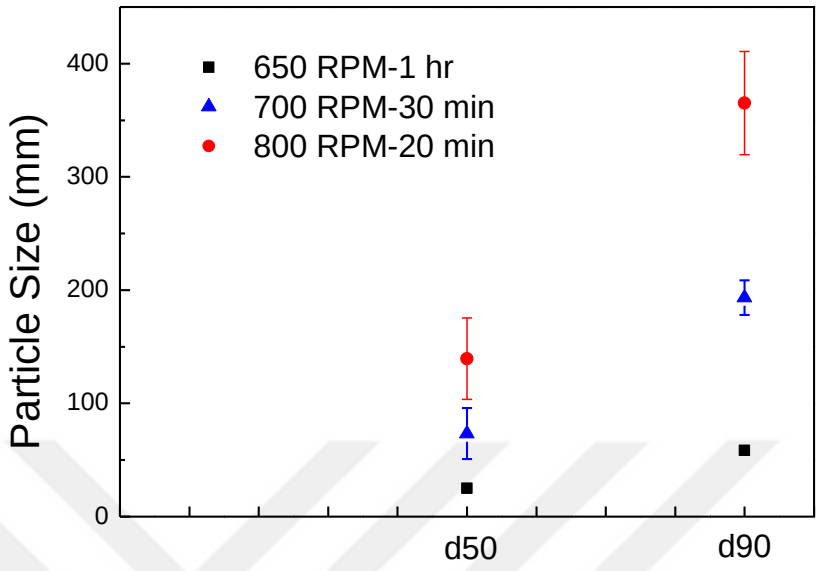

Figure 2. 7 D50 and D90 values for various milling conditions. Error bars on this plot represents 95% confidence interval of the mean.

Grinding balls are selected to be smaller than 5mm. Ball to powder ratio was set to 10:1 to obtain maximum powder efficiency. The powders produced by mechanical milling are screened using a vibratory shaker with sieves (ASTM) of sizes ranging from 45 to 149 μm. sieves. The average particle size in each range is determined using scanning electron microscopy (SEM) images.

2.6.3. Plasma Synthesis

Nano powder synthesis is carried out using a Tekna thermal induction plasma system. The system holds a RF power terminal having an oscillator frequency of 2-5 MHz, which is connected to an induction plasma torch (Tekna PL-35). Plasma torch has a power of approximately 30 kW and positioned at the top of the reactor. A schematic illustration of the thermal induction plasma system is presented in Figure 2. 8. The tests are performed at 25 kW under 0.97 bar pressure. The temperature of the reactor is maintained constant by a deionized water cooling system.

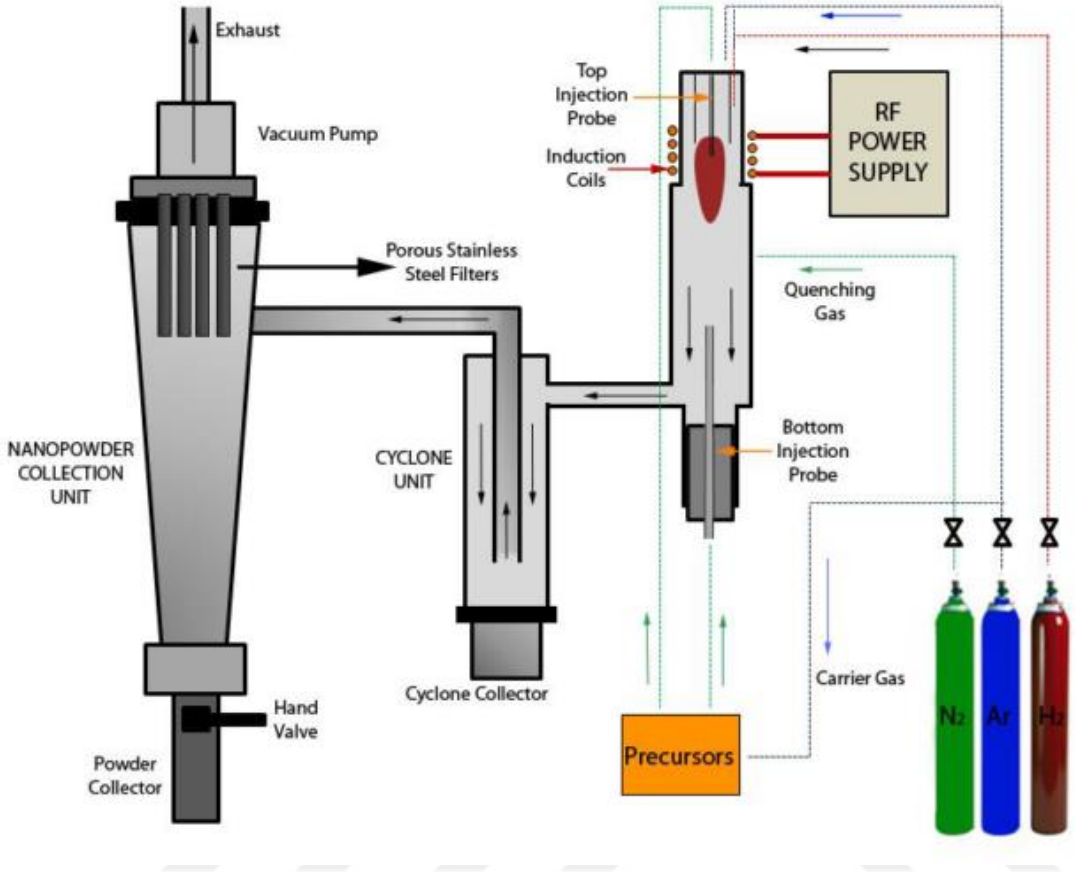

Figure 2. 8 Schematic illustration of the Tekna thermal induction plasma system [70].

The ball-milled powders are fed into the plasma reactor using a vibrational powder feeder (Figure 2. 9) The feeding rate is determined beforehand by calibrating the frequency and stroke. Arc current and hydrogen partial pressure are adjusted according to the feed rate.

Plasma forming central gas is Ar (Linde, 99.995% purity) and the sheath gas (stabilizing plasma discharge and protecting the tube from overheating) is a gaseous mixture of Ar (Linde, 99.995% purity) and H_2 (Linde, 99.995% purity). The purpose of hydrogen is to prevent the excessive heating of the plasma torch and to enable a proficient thermal interaction.

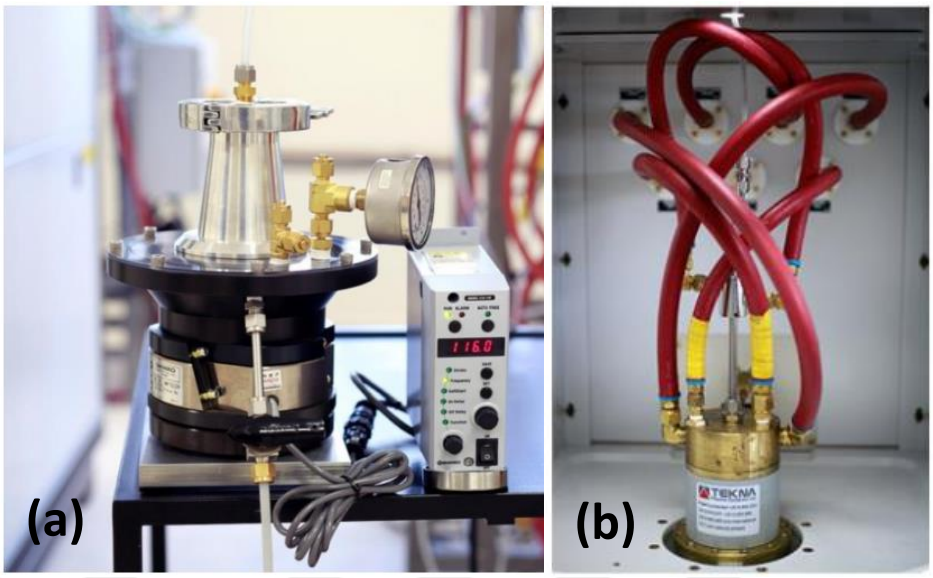

Figure 2. 9 Photos of (a) vibrational powder feeder system and (b) the plasma reactor [70].

Ball-milled AlNiCo powders vaporizes at the plasma torch where the temperature reaches more than 10,000°C. Nanoparticles are synthesized during the rapid condensation in the quenching zone. Process parameters of the plasma induction system are summarized in Table 2. 1.

Table 2. 1 Process parameters of the induction plasma system

Power	~ 24 kW
Plate Voltage	7 kV
Plate Current	3.4 A
Grid Current	4 A
Central Gas	15 lt/min Ar (Linde, 99.995% purity)
Sheath Gas	6 lt/min H_2 (Linde, 99.995% purity) + 60 lt/min Ar(Linde, 99.995% purity)
Quenching Gas	N_2

Following quenching, particles reach to a cyclone unit, where they are sorted out according to their sizes in 2 collector stations. Relatively coarse particles (> 1-2 μm) are collected at the first collecting chamber. Finer particles reach to the second powder collection unit. The typical particle size of the yield ranges from 10 to 100 nm. The plasma synthesized powders are collected from these two chambers after adequate passivation with O_2 in order to prevent the sparking while handling. It should be noted that oxygen release into the system is adjusted throughout the experiments to allow the formation of the core structure encapsulated with an iron-oxide layer.

2.6.4. Characterization Techniques

Microstructural and elemental analysis was carried out using FEI 430 NanoSEM -30 kV Field Emission Scanning Electron Microscope (SEM) equipped with an energy dispersive X-ray spectrometer (EDAX SSD Apollo10 Detector). Powder samples were embedded in epoxy resin for microstructural analysis. The mounted samples were ground with silicon carbide (SiC) papers under water and polished with aqueous slurries of alumina with sizes 0.1 and 0.05 μm. Each polished mount was then etched with Keller's reagent for approximately 10 seconds. Sides of the epoxy was painted with silver paint suspension to maintain conductivity. For particle size analysis, powders were sprinkled onto the double-sided conductive carbon tape and sealed by pressing lightly to make sure they do not get loose and fly off under the vacuum. Energy Dispersive X-Ray Spectroscopy (EDS) data was collected from various parts of the sample for at least 60 seconds.

A Jeol JEM-2100F Transmission Electron Microscope (200 kV) was used for characterization of the plasma synthesized powders. Transmission electron microscopy (TEM) is a technique in which a beam passes through a thin portion of the sample and an image is formed due to the interaction between the electrons and the specimen. First and foremost, a TEM sample must be electron transparent to be analyzed. Thereby, TEM specimen preparation generally involves thinning the sample (assuming on Al specimen < 100 nm for conventional TEM and < 30 nm for HRTEM).

TEM sample preparation procedure depends on whether the sample is self-supporting or not. The self-supporting samples are bulk and strong enough to hold themselves on the TEM holder. Specimen goes through stages such as cutting, dimpling, thinning (i.e. electropolishing, ion milling) and a 3 mm disk with an electron transparent region is formed at the end. The final specimen should be representative, stable under the beam and thin to avoid multiple scattering events [71].

Samples that are not capable of supporting themselves on the holder (i.e. powders, fibers) are either embedded in a resin (i.e. epoxy) to form a 3mm disk or used as is on a TEM grid. If the powders are large or not stable under the electron beam, it is better to mount them into a special epoxy. The powders are mixed with a TEM compatible resin in a form of 3 mm disk and the mixture is cured. Reinforced resin disks are then treated as a self-supporting specimen and prepared in a similar manner using conventional thinning techniques such as ion milling. If the specimen is sufficiently thin to be electron transparent, a TEM grid can be used. The method basically consists of forming a solution of sample and ethanol, floating the finest particles, dripping directly onto the TEM grid and letting it dry. Various types of grid supports are available for all TEM applications in life sciences and materials science. According to the mesh size and shape, copper and carbon grids in various configurations such as holey, lacey, square, oyster etc. used for certain applications. It should be considered that if a copper grid is used, it may contribute to the X-ray signal during the X-ray analysis.

Samples prepared in this part of the study were already thinner than 100 nm and were suitable for float and drip method. However, their magnetic nature and the fact that they were nano-sized particles present a problem to instrumentation and imaging. The electromagnetic parts of the microscope may attract the magnetic particles forcing them to stick to the lens polepiece. In addition, the magnetic field emitted by sample may deflect the electron beam causing drifts of both the beam and the image. In order to minimize the magnetic disturbance and stabilize the image, TEM specimens are prepared by focused ion beam (FIB) technique. FIB is a relatively new technique used

for ionic thinning of TEM specimens. The method consists of machining a lamella from a certain area of the sample using ion beam (generally gallium). The thin slice was then firmly attached to a TEM grid through welding and an electron transparent and stable TEM specimen is formed. JEOL JIB-4501 MultiBeam Focused Ion Beam-Scanning Electron Microscope at Sabancı University is used. Steps of FIB specimen preparation is given in Figure 2. 10.

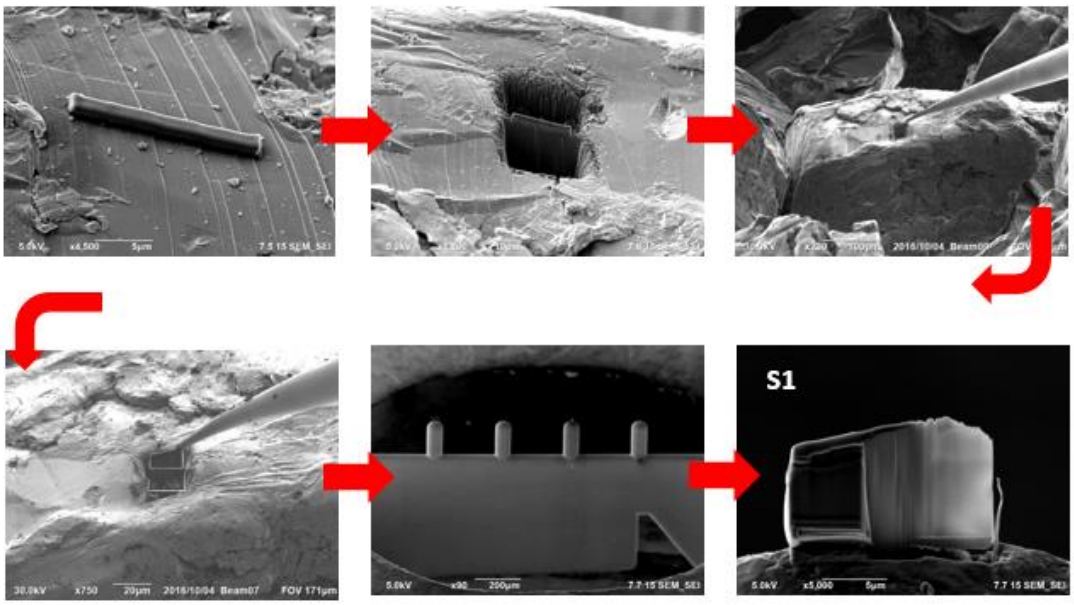

Figure 2. 10 Secondary electron images of the FIB procedure showing the sectioning, trenching, cutting and welding stages, respectively.

TEM used in this study was equipped with an energy dispersive X-ray spectrometers (EDS), and has scanning transmission electron microscopy (STEM), high angle annular dark field (HAADF) capabilities. Gatan beryllium single or double tilt specimen holders are used throughout the study. Beryllium single tilt holder minimizes unwanted X-ray signals coming from the holder during elemental analysis whereas the double tilt holder enables obtaining higher tilting angles for diffraction purposes. The conventional XRD analyses (Cu-Kα) are conducted at Bragg-Brentano geometry between 2θ degrees of 10 and 100 at a scan rate of 2 degrees/min.

Magnetic properties of the powders are measured by vibration sample magnetometer ADE Magnetics EV/9 at room temperature with applied fields up to 2 T. In vibrating sample magnetometer (VSM), sample is placed in between a set of coils creating a uniform external magnetic field. Vibration with a certain amplitude and frequency creates disturbance in the magnetic field and the change in the value of the magnetic induction is monitored through magnetic field sensors. Powder samples are weighted around 100 mg and embedded in epoxy. Measurements are repeated three times.

2.7. RESULTS AND DISCUSSION

Planetary ball-milled powders are sorted out by sieving and corresponding SEM micrographs are given in Figure 2. 11. It is observed that the ball-milled powders have irregular shapes with faceted corners. Average particle size is calculated for ball-milled samples using SEM micrographs. An approximate number of 100 powder particles in each size range are measured in order to calculate the average particle size. The corresponding EDS analyses indicated that the nominal compositions remained the same after milling.

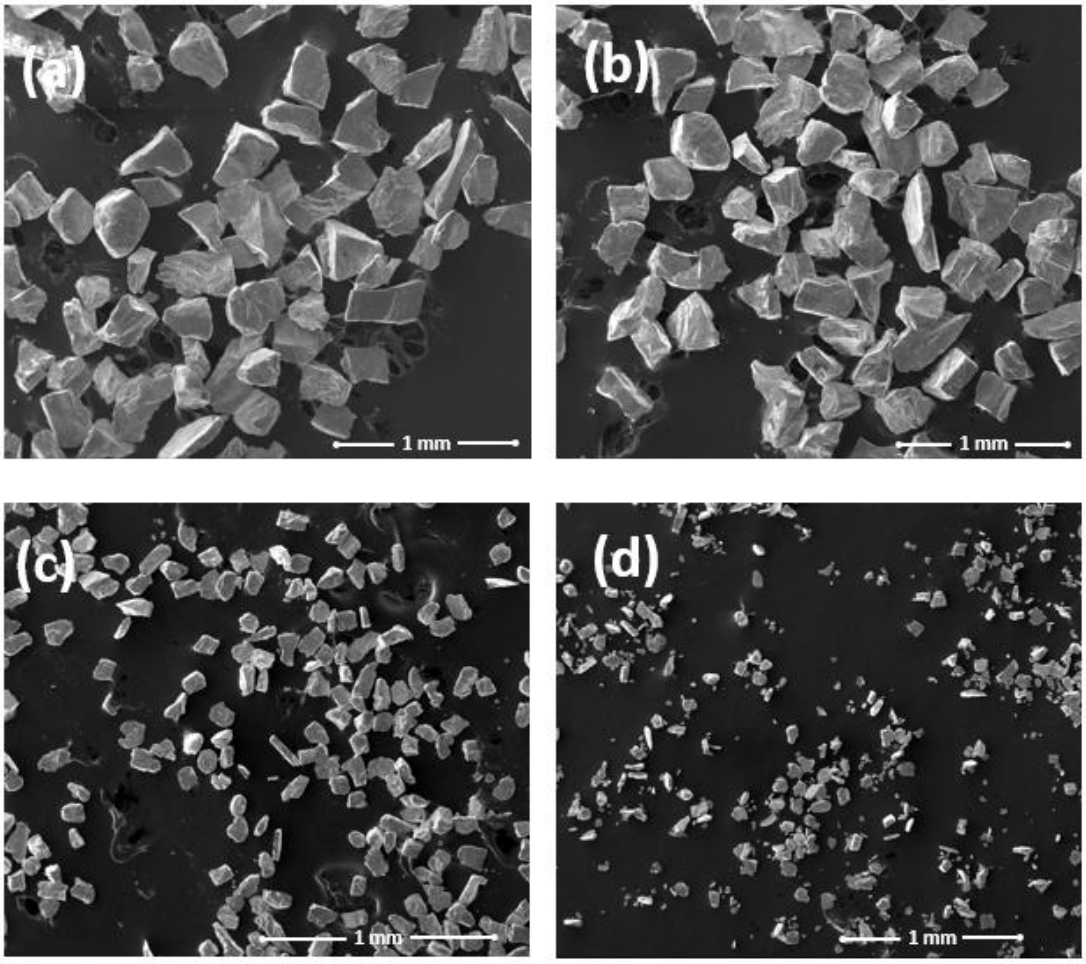

Figure 2. 11 SEM micrographs of ball milled and sieved samples with sieve sizes of (a) +149 μm, (b) -149 μm +75 μm, (c) – 75 μm +63 μm and (d) -63 μm +45 μm at different magnifications.

SEM micrographs of the plasma synthesized powders are given in Figure 2. 12. It is observed that plasma synthesized nanoparticles have spherical morphology, connected in chains and physically aggregative in nature. Average particle size is calculated for plasma-synthesized samples using SEM and scanning transmission electron microscope (STEM) micrographs. An approximate number of 100 powder particles in each size range are measured in order to calculate the average particle size. The corresponding EDS analyses indicated that the nominal compositions remained the same after RF plasma treatment.

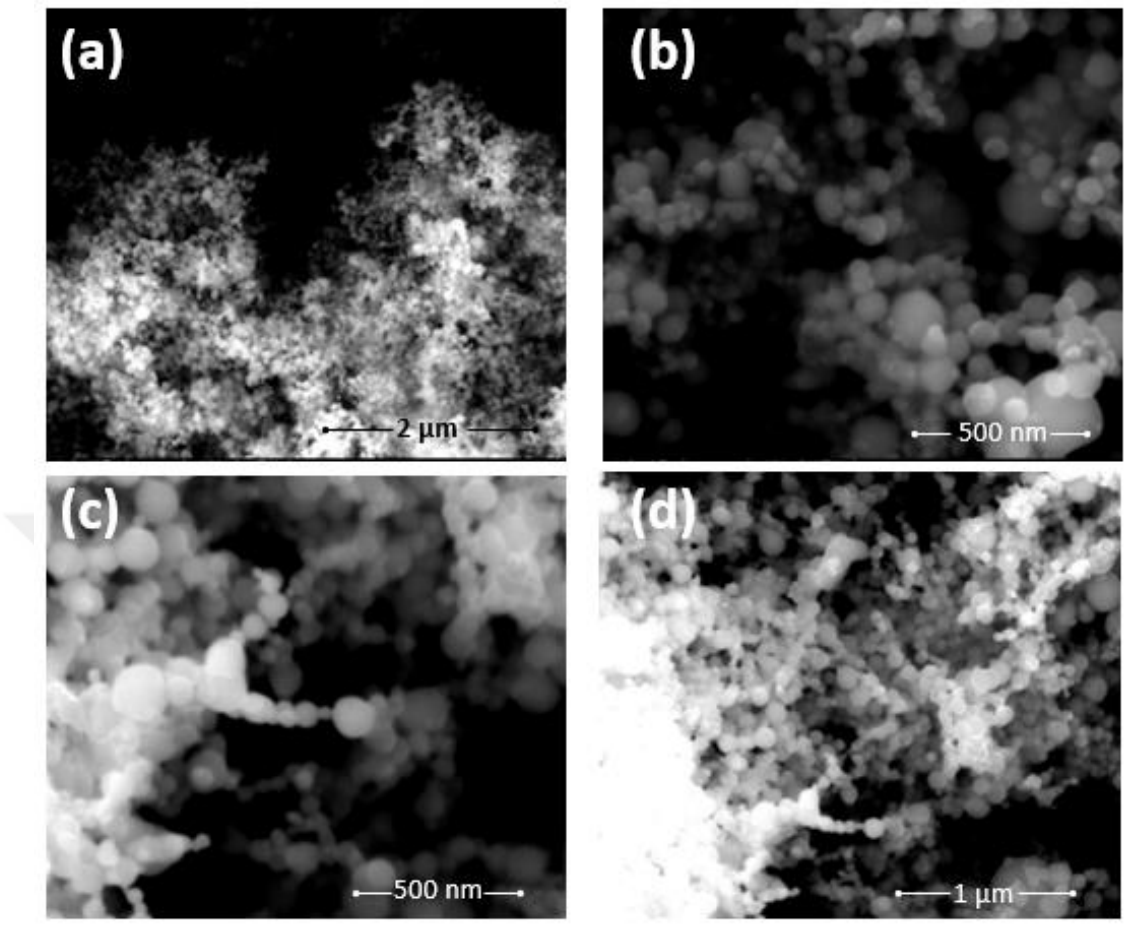

Figure 2. 12 SEM micrographs of plasma synthesized AlNiCo alloy at different magnifications.

A core/shell structure is clearly seen in bright field micrograph as shown in Figure 2. 13(a) for plasma synthesized nanoparticles. The cores appear dark and shell is lighter in the TEM images due to the large difference in electron penetration efficiency on AlNiCo and iron oxides. This core/shell structure is difficult to be revealed and identified with conventional SEM. When only the cores of the particles are taken into consideration, the mean size of the plasma synthesized nanopowders is estimated as 30 ± 5 nm from 100 individual particles. The average diameter of the shell is found to be 50 ± 9 nm.

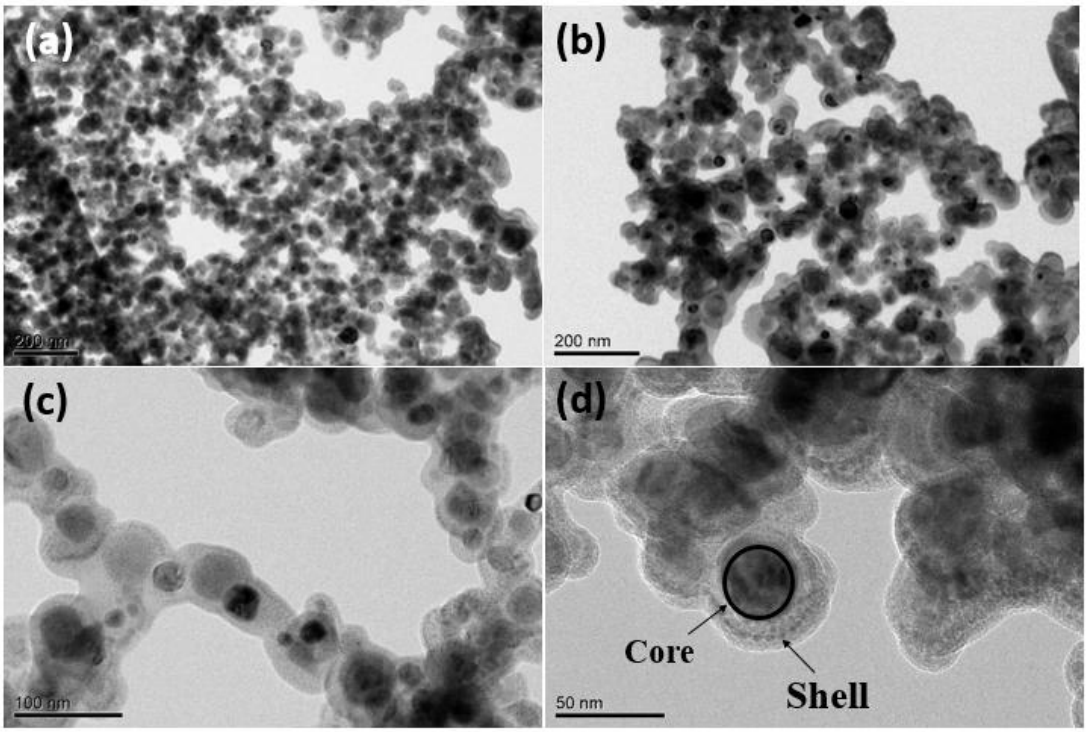

Figure 2. 13 (a)(b)(c) Bright-field TEM images of plasma synthesized powders at different magnifications (d) STEM image showing the core/shell structure.

EDS analyses in STEM are carried out to identify the elemental composition of the core and the shell layers. STEM combines the principles of transmission electron microscopy and scanning electron microscopy. Its primary advantage over conventional SEM imaging is the improvement in spatial resolution. The electron beam is focused into a narrow spot which is scanned over the sample in a raster. The rastering of the beam across the sample makes these microscopes suitable for analysis techniques such as mapping by energy dispersive X-ray (EDX) spectroscopy, electron energy loss spectroscopy (EELS) and annular dark-field imaging (ADF). These signals can be obtained simultaneously, allowing direct correlation of image and quantitative data. STEM EDS data from the core and shell collected separately. The region of interest is provided in Figure 2. 14(a) and (b) and the spectra obtained is provided in Figure 2. 14(c). The oxygen weight percent was found to be high for the shell whereas the value drops down to almost 10 percent for the core (Table 2.2). The results have

been reported with standard deviation. Higher error margin for the data of the shell is due to the lower thickness and dead time. Oxygen content is found to be higher for the shell relative to the core when the Fe peak is normalized. This suggests that the core is perfectly encapsulated with a continuous oxide layer. By considering the stoichiometric ratios obtained from EDS analysis, it is concluded that the rim and the core consists of Fe_3O_4 and FeCo-NiAl phases, respectively. Controlled oxidation of the resultant AlNiCo nanoparticles has led to formation of Fe_3O_4 shell, as clearly seen in Table 2.2. The corresponding selected area electron diffraction (SAED) analysis revealed the co-existence of FeCo-NiAl and Fe_3O_4 phases (Figure 2. 14(d)).

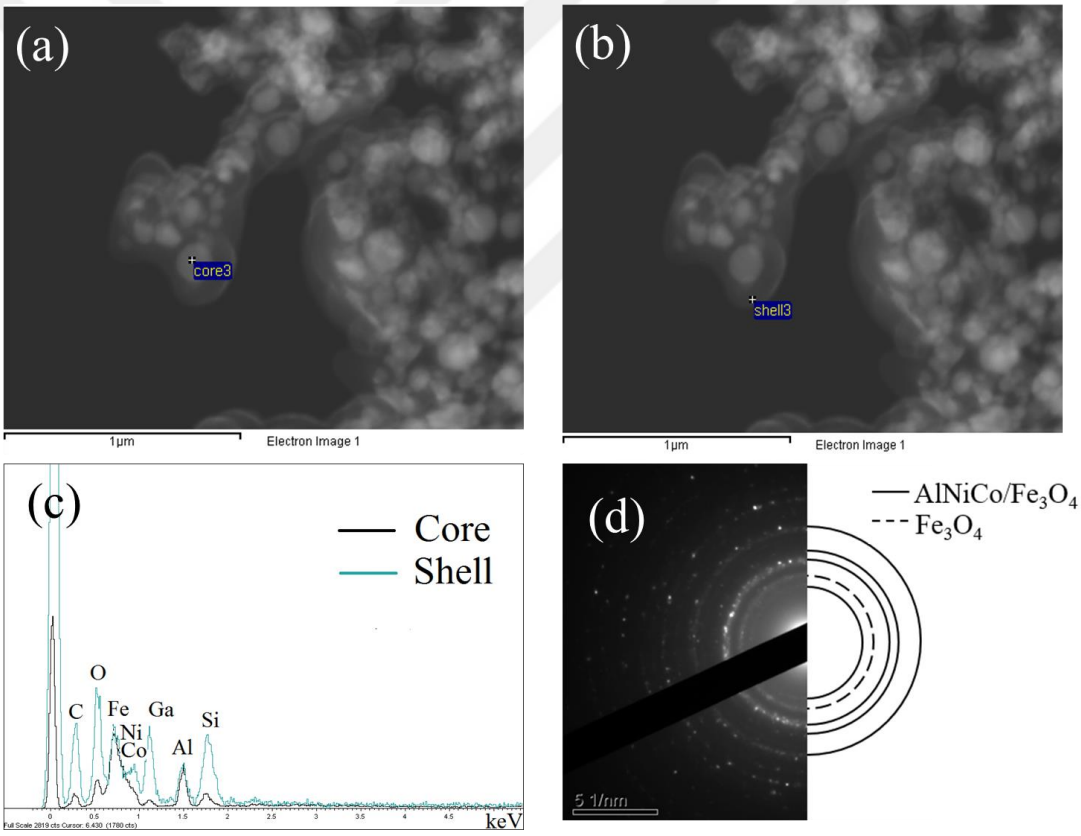

Figure 2. 14 (a)(b) STEM micrograph showing the region of interest where EDS analysis is carried out, (c) STEM EDS analysis of the core and shell layers showing the difference in the oxygen content, (d) SAED pattern showing the Fe_3O_4 and FeCo/NiAl reflections.

Table 2. 2 Average EDS data of the core and shell structure from 10 measurements.

Element	O (Kα)	Al (Kα)	Fe (Kα)	Co (Kα)	Ni (Kα)	Cu (Kα)
Core (wt%)	10.90±0,6	47.26±15,11	39.43±4,27	15.26±1,28	9.86±0,61	21.99±5,68
Shell (wt%)	2.56±0,12	1.94±2,04	10.47±15,69	4.99±3,87	0.65±2,43	34.68±8,61

It is elusive to distinguish these phases under electron and X-ray diffraction as they share common Bragg reflections. Assuming that the oxide layer covers the surface of the magnetic AlNiCo nanoparticles homogeneously throughout the sample, the core-to-shell volume ratio is calculated to be 1:4 from 30 individual core/shell particles. Fe_3O_4 phase formation is also confirmed by the X-ray diffraction of AlNiCo powders after plasma treatment. The microstructure before plasma process found to consist of only two phases: primary magnetic phase FeCo and the matrix NiAl as reported in the literature [29] (Figure 2. 15(a)). In case of ball milling, it is observed that powders of different sizes have the same phase compositions (FeCo and NiAl) as the master alloy Figure 2. 15(b). A similar XRD spectra indicates the absence of a new phase and impurities within the detection limits of an X-ray diffractometer.

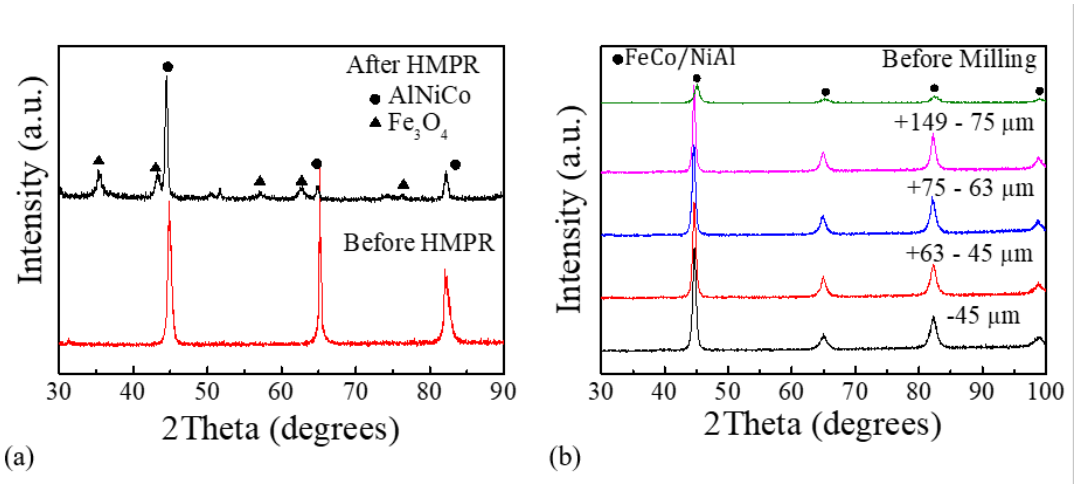

Figure 2. 15 (a) X-ray diffraction pattern of the ball-milled powders before and after plasma reaction. (b) X-ray diffraction pattern of the ball milled and sieved powders.

The hysteresis loops, demagnetization curves of ball-milled sieved powders and plasma synthesized nanoparticles are presented in Figure 2. 16(a). In terms of magnetization, the major hysteresis loops of sieved samples show soft magnetic character with low coercivity values. It is observed that there is an increase in coercivity with decreasing mesh size as expected. Nanoparticles of AlNiCo alloy produced by plasma technique showed significantly higher coercivity relative to the ball-milled counterpart at the expense of a decrease in magnetic saturation. Coercivity increased 5 times, starting from 50 Oe reaching to almost 250 Oe. This value is found to be in consistence with another AlNiCo nanopowder study by Li et.al. [45]. For comparison second quadrant of the hysteresis loop is placed as an inset on the same graph. The change in coercivity values with average particle size is shown in Figure 2. 16(b). In addition to the increase in coercivity, it is observed that the Br decreased with decreasing particle size which is in good agreement with previous observations [72].

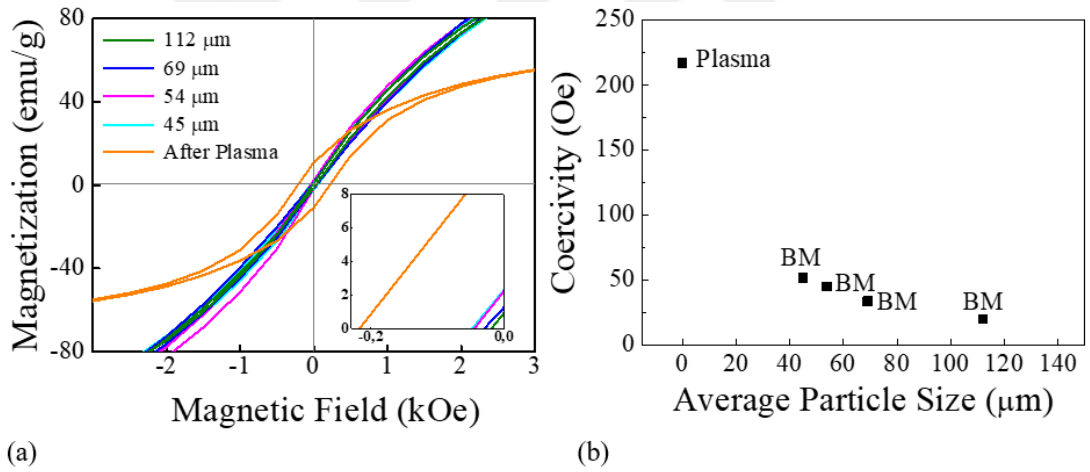

Figure 2. 16 (a) Hysteresis loops of the ball-milled/sieved and plasma synthesized powders, inset shows the improvement in the Hc after plasma reaction, (b) the change in Hc of the powders with respect to the average particle size.

A general relationship between the coercivity of a composite in terms of the amount of magnetic material utilized can be expressed by rule of mixtures [73]. Rule of mixtures has been previously applied to properties such as saturation polarization, permeability, coercivity and density [73]. For the current case, the coercivity and saturation magnetization values of the Fe_3O_4 and AlNiCo nanoparticles are obtained

from literature [45], [74], [75]. Fe_3O_4 is a soft magnetic phase and its coercivity is measured to be approximately 157 Oe for agglomerated nanoparticles [74]. The corresponding coercivity for nanosized AlNiCo particles is taken from the study of Li and coworkers as 300 Oe [45]. Using these data, the volumetric fraction of the core/shell particles is calculated as 1: 3.9. This is almost equal to the measured volume fraction of the core/shell particles, which is measured as 1:4. Overall the coercivity shows a rising trend, even though the size of the plasma synthesized particles (30 ± 5 nm) are not in the ideal theoretical range (2-20 nm) for maximum coercivity as reported in [45]. Core/shell structure with an oxide coating on the surface of metallic nanoparticles is observed to be effective for improving the oxidation resistance of metallic nanoparticles [76]. As metallic nanoparticles have extensive surface area, their oxygen sensitivity/reactivity is excessive even at ambient conditions. The formation of the oxide shell layers may protect the particles from further oxidation [62]. For the current case, the powders collected from the first collection chamber are kept in air for almost one year and then checked for the efficiency of the protective layer. The coercivity of the powders (> 1-2 μm) kept in air is measured as 81.5 Oe which is almost equal to the coercivity value obtained right after production (82.5 Oe). Thus, the samples that are kept in air show high stability and exhibit no evident loss in magnetic properties as the magnetic nanoparticles are tightly wrapped by a protective magnetic oxide layer.

2.8. CONCLUSIONS

In summary, AlNiCo powders of different sizes are produced with plasma reaction and ball milling. A protective oxide layer is created for the plasma synthesized AlNiCo nanoparticles as confirmed by STEM analysis. XRD spectra and EDS data revealed the formation of Fe_3O_4 as protective layer. The magnetic measurements indicated that significant increase in coercivity with decreasing particle size. In addition, the core/shell structure contributed to the enhancement of magnetization due to the effective exchange coupling. The exchange coupling lead to a smooth rotation of the magnetization vector from the easy-axis orientation between core and shell, thereby

increased the magnetization. The magnetically hard core provides high coercivity whereas the magnetically soft shell increases the magnetic flux density. As a combination of this behavior and the coupling between the core and shell, a relatively square hysteresis loop is achieved. The oxide coating not only contributed to an increase in coercivity; but, also to the protection of the metallic nanoparticles against further oxidation. The interfacial exchange interaction between the magnetically hard core and magnetically soft shell hard and soft magnetic phases may yield finely tailored materials for various magnetic applications.

CHAPTER 3

INVESTIGATION OF PHASE SELECTION HIERARCHY IN MnAl-BASED ALLOYS

3.1. INTRODUCTION

MnAl-based alloys, having a theoretical BH_{max} value in between rare-earth magnets and rare-earth free magnets draw the attention as a promising permanent magnet candidate [77]. This novel alloy has attracted much interest owing to its low cost, high energy per unit weight and high coercivity relative to the other conventional RE-free permanent magnets [78], [79]. Its magnetism arise from a metastable ferromagnetic τ-phase and the exact mechanism of τ-phase transformation is unclear.

In this chapter, it is aimed to have a better understanding of the τ-phase formation through microstructural, thermal and X-ray analyses. If the exact transformation mechanism is determined, it is possible to increase the ferromagnetic phase quantity, stabilize the τ-phase and improve the magnetic properties. The effect of composition on the phase selection hierarchy was investigated. It is observed that there is a compositional limit to τ-phase formation. Mn70% (wt) was found to be the limit and further increase in Mn content results in the formation of stable phases. It is observed that ε→τ transformation is dependent on ordering of the ε-phase and can only proceed with an intermediate phase known as the ε'-phase. ε and ε'-phases were observed at room temperature and transformed into τ-phase upon annealing. Compositional ordering do not take place as Mn content increases and intermediate ε'-phase do not occur. Instead, stable phases form and magnetization diminished. In situ TEM imaging confirmed the transformation sequence.

3.2. MnAl ALLOY TRANSFORMATIONS

First characterized in 1950s, manganese-aluminum alloys did not receive much attention until more recently. MnAl alloys, in fact, exhibit an attractive combination of magnetic properties for many technological applications, including bulk permanent magnets and thin-film devices. In addition to its permanent magnet properties, MnAl alloy shows superior machinability impact strength and good corrosion resistance. It is also light-weight and relatively economical.

In 1958, a new metastable tetragonal ferromagnetic τ-phase originated from a hexagonal close-packed ε-phase was observed in MnAl alloys (47% to 60% of Mn) [80]. The magnetic properties derive from the formation of a metastable $L1_0$ intermetallic phase (τ -MnAl) [81]. Body-centered tetragonal $L1_0$ structure have the potential to be used as a permanent magnet material due to high, uniaxial magnetocrystalline anisotropy. The energetically favorable, preferred direction for the magnetic moment is the *c*-axis marked in Figure 3. 1. $L1_0$ is a crystallographic derivative of the face centered cubic (fcc) structure. It is a well-known fact that most $L1_0$ compounds form either by a peritectic transformation or from a high temperature disordered fcc phase [82]. Unlike fcc, whose faces and corner sites occupied by the same atoms, $L1_0$ structures have two of the faces occupied by one type of atom and the corner and the other face occupied with the second type of atom. The shortest distance between a pair of Mn atoms within the lattice is found to be 2.66 Å [80].

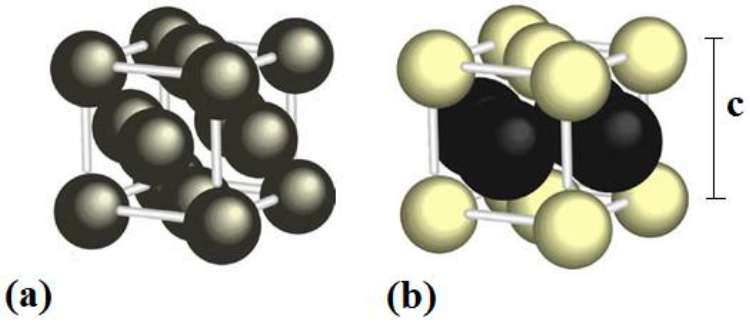

Figure 3. 1 Schematic atomic structures of (a) an face-centered cubic and (b) a body-centered tetragonal $L1_0$ [83].

Conventionally τ-phase is achieved through quenching of ε-phase followed by annealing at a relatively low temperature as shown in the phase diagram provided in Figure 3. 2. The alloy is first solutionized at high temperatures, about 1150 -1250°C until the structure becomes fully ε. It is then quenched in cold water to retain the ε phase at room temperature. The rapid cooling process not only provides sufficient undercooling for the room temperature stability of the disordered ε (hcp) phase; but, it also keeps the grain size small and introduces defects to the microstructure [84]. It was found that a cooling rate of 10 degrees/sec at 800°C was required for the formation of the ferromagnetic phase. The quenching is followed by annealing the alloy at various temperatures ranging from 350 to 500°C for different time periods. Subsequent annealing transforms the ε-phase to τ-phase. The annealing overcomes the activation energy required for the transition from the ε state to the τ state.

In the Mn-Al phase diagram (Figure 3. 2), τ-phase formation range is marked by a curved dashed line at compositions between 50 at.%Mn and 60 at.%Mn [78], [85]. Thereby, most of the studies are concentrated within this range. It is known that the β and γ2 phases make up the majority of the standard form of Mn-Al at room temperature. β-γ2 split is more energetically favorable and thereby, τ phase is less in quantity [86].

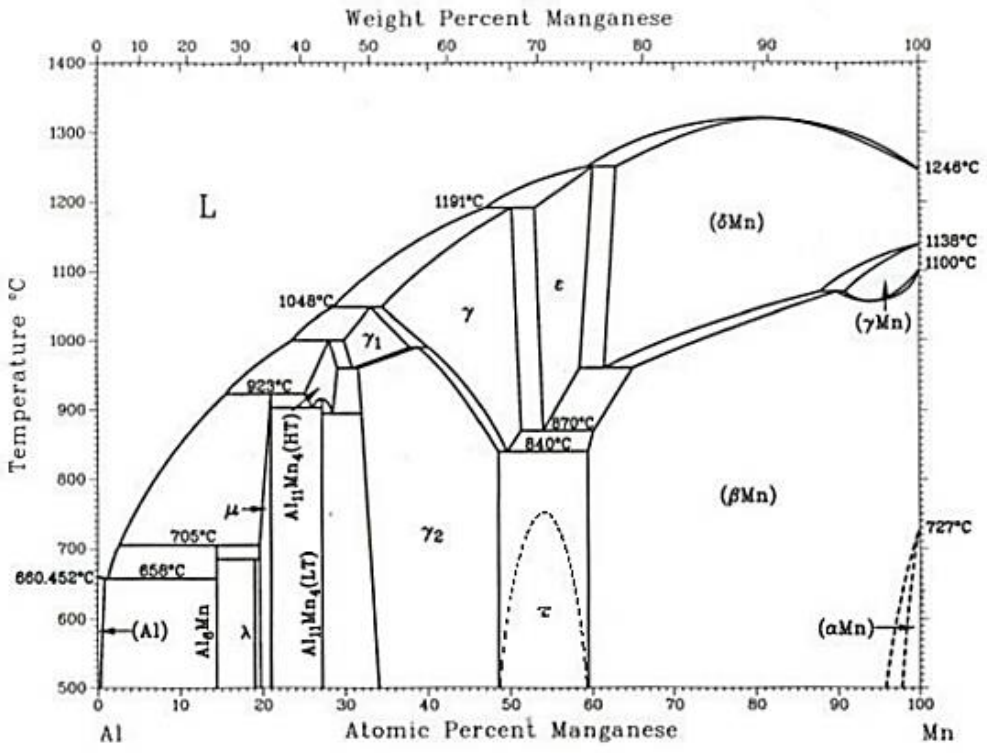

Figure 3. 2 Phase diagram of Mn-Al system [87].

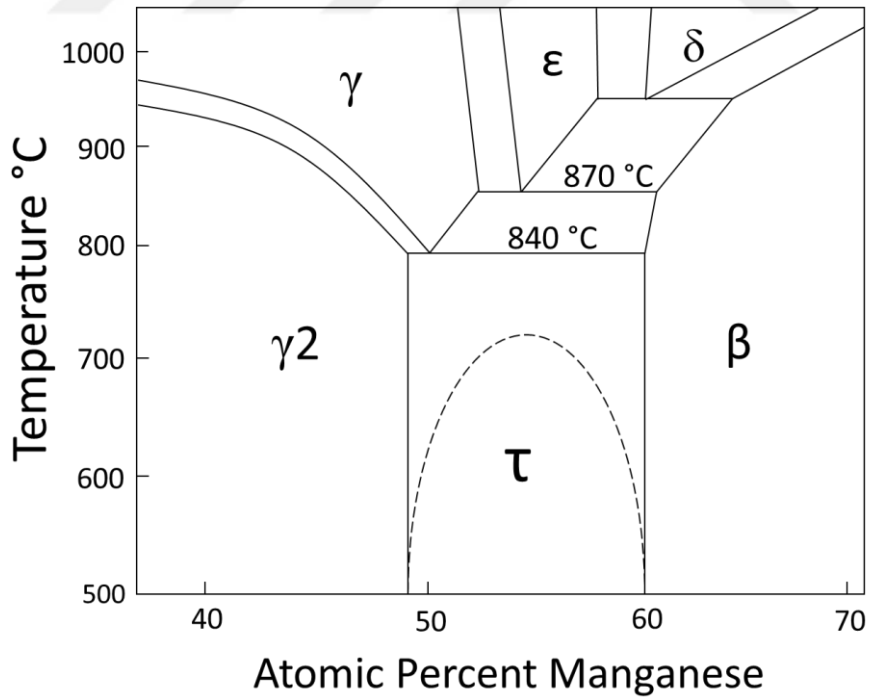

Figure 3. 3 Portion of the phase diagram showing the ε→τ transition.

As the τ-phase is metastable, it can be obtained with non-equilibrium solidification techniques. Several fabrication methods such as melt spinning [88]–[90], splat quenching [91], gas atomization [92], [93] and mechanical milling [94]–[98] are commonly utilized since they allow access to thermodynamically metastable phases [78], [79]. Singh and co-researchers (2015) studied the effects of different processing techniques on $Mn_{54}Al_{46}$ alloy in 2015 [85]. The magnetic properties were found to depend on the crystallite size of the ε-phase and the density of defects. Mechanical alloying resulted in a microstructure, which consists of small grain size, high defect density, but low amount of τ-phase. The arc-melted alloy had the largest grain size and the highest fraction of τ-MnAl phase. The highest Curie temperature (365 °C) and coercivity (1.8 kOe) were achieved for the samples prepared by a combination of arc-melting and ball milling. Improved magnetic properties were attributed to the pinning of ferromagnetic domains by the defects. These defects were also believed to act as nucleation sites for the τ-phase [85]. Optimum magnetic properties of the same composition ($Mn_{54}Al_{46}$) were achieved after annealing the sample at 400 °C and obtaining an average grain size of 300 μm in the study by Foreback and coworkers (2008) [97]. Similarly, Zeng and Baker (2006) observed that magnetic properties are strongly dependent on both the fraction of τ-phase and the grain size. Mechanical alloying and mechanical milling were used to produce nanocrystalline microstructure. A coercivity of 4.8 kOe and a remanence of 87 emu/g were reported for $Mn_{54}Al_{46}$ powders annealed at 400 °C for 10 minutes [96]. The ε→τ transition temperature of melt-spun $Mn_{55}Al_{45}$ decreased by 100 K due to fine ε-phase grain size [99]. In the study by Sakka and co-researchers (1989), it is observed that cooling rate affects the quantity of the τ-phase formed, thereby has an influence on the magnetic properties. The rapidly quenched ribbons have a larger B_r and H_c than the water-quenched bulk samples in the MnAl systems [100]. This is likely due to an increase in the τ-phase quantity.

In order to improve the magnetic properties of MnAl-based permanent magnet alloys, the τ phase formation mechanism must be well understood. There are three different theories proposed in literature attempting to explain mechanism of ε→τ phase

transformation. The first theory states that the ferromagnetic τ-phase forms via a two-step process; metastable B19 ordering within the parent ε-phase (ε →ε') followed by a displacive or martensitic shear transformation (ε' →τ) [77], [101]–[107]. ε'-phase is an intermediate disordered state of ε phase and it is not shown on the phase diagram. It is suggested that ε-phase (a = 2.69 Å and c = 4.38 Å) already contains numerous small nuclei of the ε'-phase (a = b = c = 3.006 Å) in the quenched state [103], [108]. Upon heating, ordering takes place and high density of stacking faults show up in the ε+ε' matrix. This faulting gives rise to the martensitic shear, which transforms ε' into a ferromagnetic τ-phase. It is later observed that the second step involves a thermally activated reordering transformation in addition to the martensitic shear [105]. The transformation sequence from parent hexagonal ε-MnAl phase to tetragonal $L1_0$ τ-phase is illustrated in Figure 3. 4.

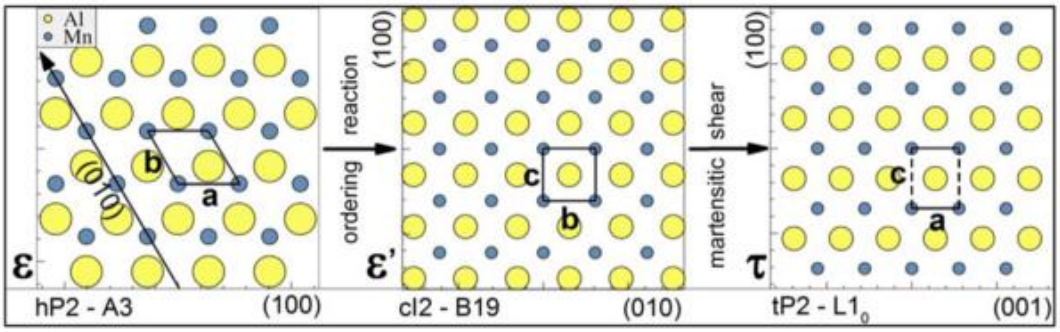

Figure 3. 4 The transformation sequence of hexagonal ε to τ-phase. ε transforms into cubic B19 ε'-phase followed by τ-phase formation through martensitic shear [106].

The orientation relationship between ε and ε' is already well established in literature [103], [109]–[111]. It is stated that there are three possible orientation variants of ε' precipitates occurred during ordering reaction. These variants are crystallographically equivalent but differ in the orientation with respect to ε-phase. The orientation relationship is stated as follows;

Variant 1: $(0001)\varepsilon \,//\, (001)\varepsilon'$ and $[11\bar{2}0]\varepsilon \,//\, [010]\varepsilon'$

Variant 2: $(0001)\varepsilon \,//\, (001)\varepsilon'$ and $[1\bar{2}10]\varepsilon \,//\, [010]\varepsilon'$

Variant 3: $(0001)\varepsilon \,//\, (001)\varepsilon'$ and $[\bar{2}110]\varepsilon \,//\, [010]\varepsilon'$

Figure 3. 5 shows schematics of the possible orientation relationships between ε-phase and ε' variants. Among three, only one of them becomes the major variant in terms of quantity and it is the only variant that can yield τ-phase through shearing [111]. It is observed that shearing of variant 1 (ε_1') together with ε-phase result in the formation of τ-phase whereas the other minority variants (ε_2' and ε_3') act as obstacles to shearing. The obstacle variants hinder the shear-type transformation and do not yield τ-phase [111]. τ-phase semicoherently nucleates within the majority ε'-phase [110].

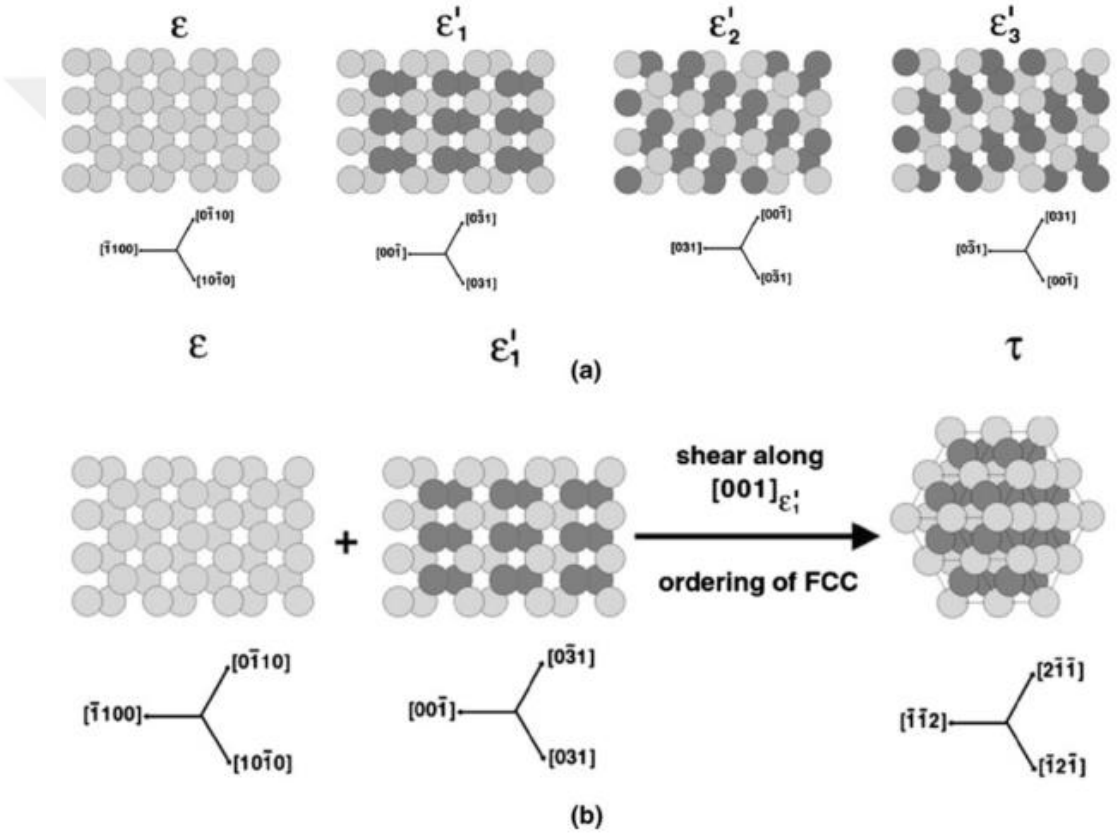

Figure 3. 5 Schematics of the orientation relationship (a) between matrix ε and three variants of ε' (b) shearing transformation of ε and major ε' variant to τ-phase along [001] (ε_1') [112].

A second theory suggests that ε→τ phase transformation occurs via a compositionally invariant, diffusional transformation known as massive transformation [84], [113]–

[115]. It is observed that the τ-phase heterogeneously nucleates at the grain boundaries and grows behind advancing incoherent interfaces over the temperature range of 723-973 K (450-700°C) [113]. The resultant microstructure of the τ-phase contains a high density of lattice defects i.e. dislocations and twins as supported by the electron microscopy observations [114]. During microstructural analysis, τ-MnAl was found to contain arrays of overlapping octahedral stacking faults, microtwins, thermal antiphase boundaries and dislocations. The origin of these defects was found to be the atomic attachment on {111} and {020}-type facets at the migrating massive growth interface [115]. Classical nucleation theory is applied in order to explain this behavior and it is suggested that the growth mechanism consists of random atomic jumps from the parent phase to nucleation sites [84].

A further mechanism involves a new transformation mechanism having both structural shear and atomic diffusion which is named as hybrid displacive-diffusional transformation [116]. Wiezorek and co-researchers (2011) carried out transmission electron microscopy (TEM) analysis to support this theory. It was asserted that the transformation kinetics are controlled by the massive transformation mode, whereas partial dislocation glide causes the τ-phase formation. TEM results showed that ε'-phase and ε-phase coexist in the same matrix, and ε'-phase is present due to the initial elastically accommodated anisotropic misfit strain. Stacking faults overlap each other which were observed in the ε + ε' matrix causing the formation of τ phase. This was also confirmed by in-situ heating TEM imaging showing that there were numerous twins and stacking faults on the close-packed planes of ferromagnetic τ-phase [111].

Even though previous studies provided insights on MnAl-based alloys, the exact ε→τ transformation mechanism is still unclear. Synchrotron light source data is never correlated with thermal analysis to our best knowledge. In this work, the transformation sequence and structural changes in four different MnAl-based alloys were investigated by means of in-situ high energy X-ray diffraction, isochronal differential scanning calorimetry (DSC) and magnetic measurements.

3.3. EXPERIMENTAL PROCEDURE

3.3.1. Production of Alloys

Ingots of Mn-Al alloys within the composition range of 67.5-73 wt% Mn - bal. Al were produced in Edmund Bühler compact arc-melting (MAM-1) furnace from high-purity Mn (99.95%) and Al (99.8%) elements under argon atmosphere. These ingots were re-melted three times to ensure compositional homogeneity. Final compositions of the alloys were verified using X-ray spectroscopic analysis.

High-purity Mn (99.95%) and Al (99.8%) elements were fed into the arc-melter in the form of pieces and shots, respectively. However, this method was observed to be problematic in terms of Mn vaporization and oxidation. Mn oxidizes readily and the oxide content affects the final composition. Thus, oxide layer was removed by submerging into a dilute nitric acid solution (5.9%) for 10-30 seconds depending on the layer thickness. In addition to this problem, vaporization occurs during melting and the ingot was found to have low Mn content. The error margin was calculated to be around 5 wt %. In order to minimize the loss, the elements were utilized in the form of pellets. Pellets were prepared by pressing Mn and Al powders. Mn bulk pieces were crushed into powders and weighed with Al powders. Mn content was adjusted 5 wt% higher in order to remain in the τ-forming range determined by the phase diagram. 3 grams of powder was then compacted into a pellet with a hydraulic press. A 15 mm die was used under 200 bar pressure. A cylindrical pellet was formed and arc-melted thereafter. Although final EDS data showed slight differences, the composition of the samples were consistent were within the expected range.

3.3.2. Heat Treatment

Following production, alloys were solutionized for an hour to produce single ε-phase at 1150 °C. They were subsequently quenched in water to conserve the high temperature metastable ε-phase at room temperature. The presence of ε-phase was confirmed by Cu-Kα X-ray diffraction analysis.

3.3.3. Characterization Techniques

a) Microstructural and Crystal Structure Analysis

Microstructural and elemental analysis were carried out using FEI 430 NanoSEM -30 kV Field Emission Scanning Electron Microscope (FESEM) equipped with an energy dispersive X-ray spectrometer (EDAX SSD Apollo10 Detector). The nominal compositions were determined using energy dispersive X-ray spectroscopy (EDS) attached to FEG-SEM.

For the TEM sample preparation, focused ion beam (FIB) in Sabancı University, Turkey was used. Secondary electron images of the final FIB samples on TEM grid are given in Figure 3. 6. Conventional transmission and high-resolution transmission electron microscopy (HRTEM) analyses were performed using Jeol JEM-2100F Transmission Electron Microscope (200 kV). Detailed information on TEM and FIB are already provided in Chapter 2.6.4.

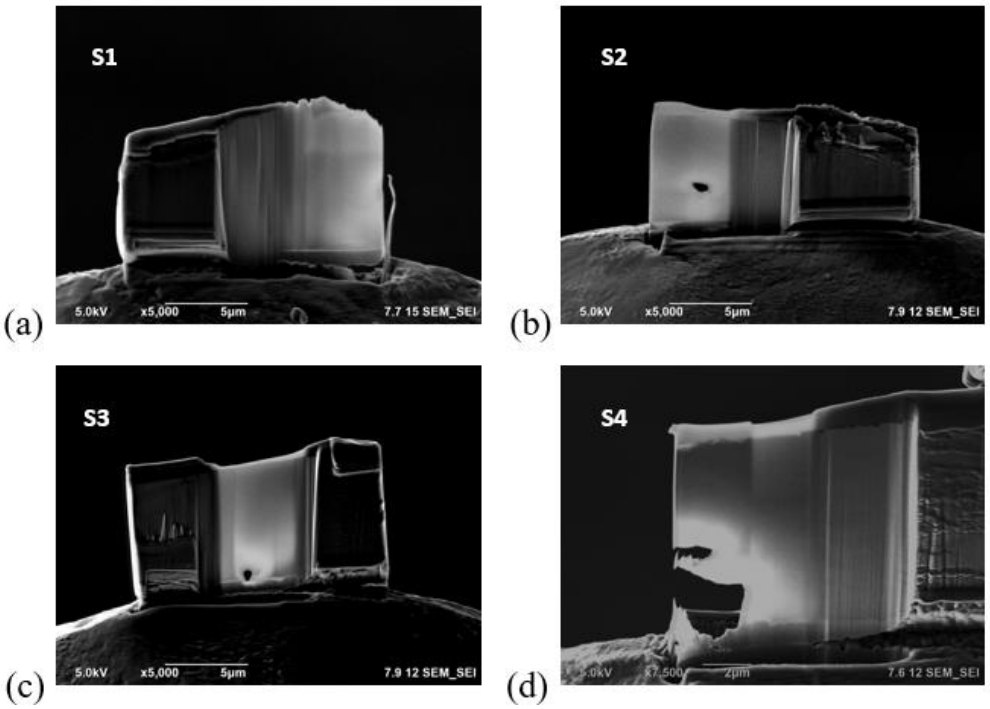

Figure 3. 6 Secondary electron images of FIB samples (a) $Mn_{67,5}Al_{32,55}$ (b) $Mn_{70}Al_{30}$ (c) $Mn_{71,5}Al_{28,5}$ (d) $Mn_{73}Al_{27}$.

In order to observe the temperature effects on ε→τ transformation, in-situ heating TEM experiments were carried out in JEOL 200kV at Anadolu University (Eskisehir). Samples were heated from room temperature to 550°C with 10°C/min as in synchrotron experiments. Single-tilt heating holders from Gatan Inc. were used during the heating experiments. In-situ heating TEM set-up basically consisted a special specimen-heating holder to heat the sample under high vacuum. Thermal and mechanical stability of the investigated samples at high temperatures are important factors that affect the resolution attained. Thermal instability causes specimen drift, which in turn deteriorates the focus settings. The main sources of the drift in most in-situ experiments are expansion or contraction of the sample, specimen charging, temperature variations induced by the electron beam and reaction of the sample with the environment. Thermal drift was initially insignificant; but, inclined with heating over time. It was manually corrected by observing the images while they were being recorded. Contamination is another common problem for in-situ TEM studies. It is observed that the samples were contaminated with gallium (Ga) ions upon annealing. It can be speculated that Ga implantation during FIB process resulted in the coalescence (ripening) of Ga precipitates with increasing temperature. The area of interest, bright field image of the in-situ heating sample and bright field, dark field images after the experiments showing Ga precipitation are provided in Figure 3. 7, respectively.

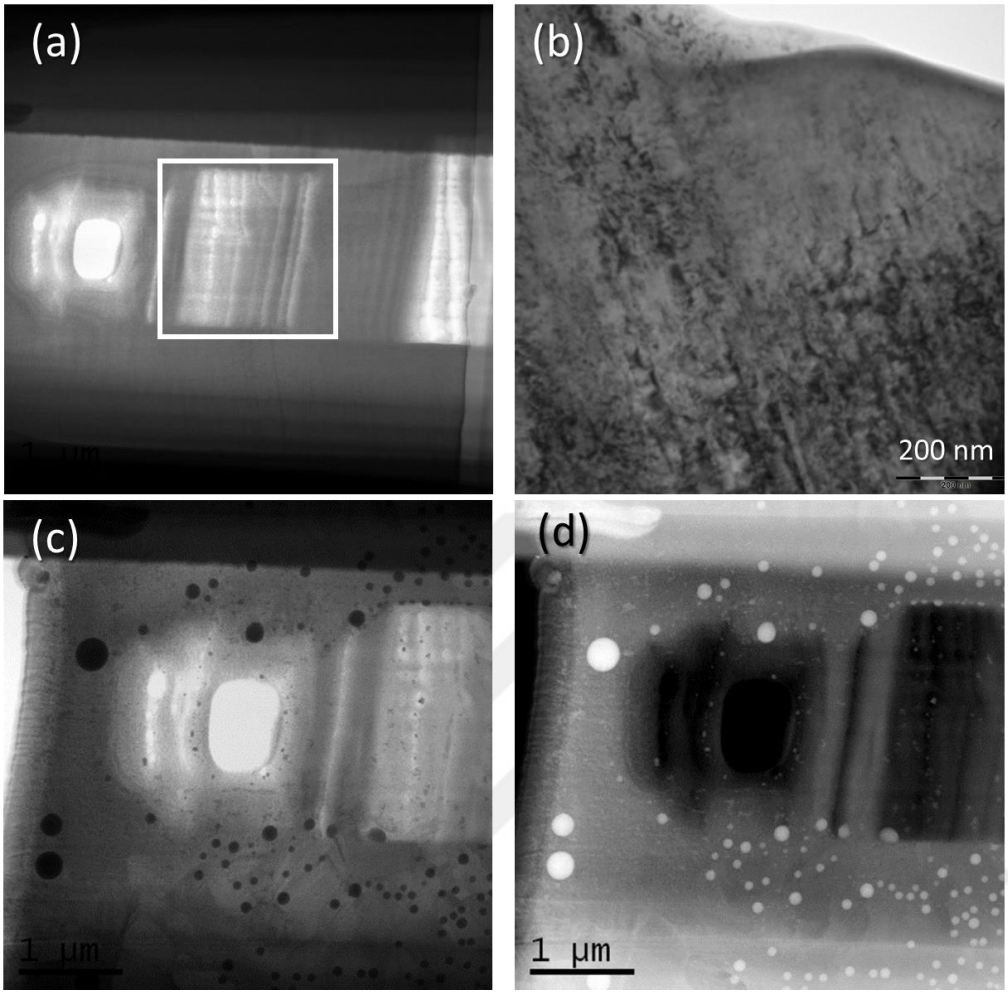

Figure 3. 7 (a) Electron microscopy image of the in situ heating holder. The area of interest is marked by a square. (b) Bright field image of the sample attached to the in situ holder. (c) Bright field image of the sample after heating. (d) Dark field image of the sample after heating showing the Ga ion coalescence.

b) Thermal Analysis

Differential scanning calorimetry (DSC) is a thermoanalytical technique used to analyze the thermal behavior during solid-state phase transformations. The difference in the amount of heat lost or gained is measured to determine the phase transitions as well as physical properties such as melting point and heat capacity.

In DSC experiments, two separate pans are placed on two separate heating platforms in DSC chamber of inert atmosphere. One pan, being the reference, remains empty whereas the other has the sample in it. The heating rate is kept constant in both heating platforms and throughout the experiments. As the temperature rises, sample pan requires more heat to keep the temperature rate constant. The amount of heat released to increase the temperature of the sample is measured by the thermocouples and recorded by the computer. The reaction can either be exothermic or endothermic depending on the nature of the heat flow.

A SEIKO SII X-DSC7000 instrument is used in this part of the study (Figure 3. 8a). Powder specimens of 10 mg were enclosed into Al pans with Al lids (Figure 3. 8b). The samples are heated-up from room temperature to 773 K (500 °C) under a protective N_2 gas atmosphere (Figure 3. 8c). N_2 gas flow is adjusted to be 20-40 cc/min. A heating rate of 10 K/min is kept constant throughout the experiments. DSC scans provide exothermic peaks for crystallization events.

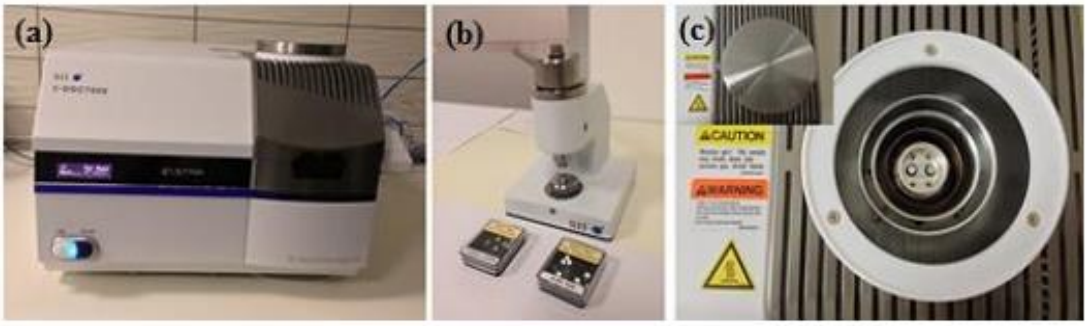

Figure 3. 8 (a) DSC instrument, (b) Al pans and lids along with the pressing tool to cover the lids and (c) heating chamber.

Activation energy of a transformation can be calculated using isochronal DSC scans. Activation energy is the thermal energy required to overcome the energy barrier and initiate a phase transformation. Kissinger [117] and Ozawa [118] methods are today's most commonly used methods to calculate the activation energy of a phase transformation. Both theories makes use of the change in transformation temperature

with heating rate. Temperature dependence of a reaction rate is best described by the Arrhenius relationship [119];

$$K = K_0 \exp(-\frac{E_a}{RT})$$

,where K is the reaction rate, K_0 is a material constant, E_a is the activation energy per mole, T is the temperature and R is the universal gas constant (8.314 J/K mole). Kissinger theory [117] is based on the assumption that for a DSC curve with a given heating rate, maximum reaction rate is obtained at the peak temperature and the derived the following equation;

$$\ln\left(\frac{\Phi}{T_p^2}\right) = const.\,(-\frac{E_a}{RT_p})$$

,where Φ is the heating rate, T_p is the peak temperature, E_a is the activation energy per mole, T is the temperature and R is the universal gas constant. T_p is determined from DSC scans of different heating rates (Φ). When $\ln(\Phi/T_p^2)$ is plotted against $1/T_p$ for a set of DSC curves with different heating rates, E_a can be determined from the slope of the curve.

Ozawa's theory [118] is based on the assumption that when a DSC curve reaches its peak, the degree of reaction is a constant value independent of the heating rate. The Ozawa relationship is described as;

$$\ln(\Phi) = const.\left(\frac{-1.052E_a}{RT_p}\right)$$

,where Φ is the heating rate, T_p is the peak temperature, E_a is the activation energy per mole and R is the universal gas constant. T_p is determined from DSC scans of different heating rates (Φ). Ozawa curve is plotted as $\ln(\Phi)$ versus $1/T_p$ and the slope of the curve is used to find the E_a.

c) Structural Analysis

Being the brightest artificial source of X-rays, synchrotron light source allows fundamental research on even the smallest details on molecular structures and find use in a wide range of applications such as physics, nanoscience, pharmaceuticals, engineering, structural biology and environmental science. It offers high flux, high brilliance electromagnetic waves and high stability of the source.

Synchrotron radiation occurs when a charged particle is accelerated by a strong magnetic field, follows along a spiral path and high brilliance X-rays are formed. The part, where the electrons are ejected form an electron source and accelerated in a linear accelerator is called as the “booster”. They are then injected into the “storage ring”, where the electrons circle at the speed of light. Magnetic fields bend the resulting X-ray and guide it towards a “beamline”, where the experiments are performed. The properties of the beamline varies according to the sample. X-ray interacts with the sample in the beamline, the detectors record the information and the data is collected from the control unit. Principle features of a synchrotron facility showing the path of synchrotron radiation is given in Figure 3. 9.

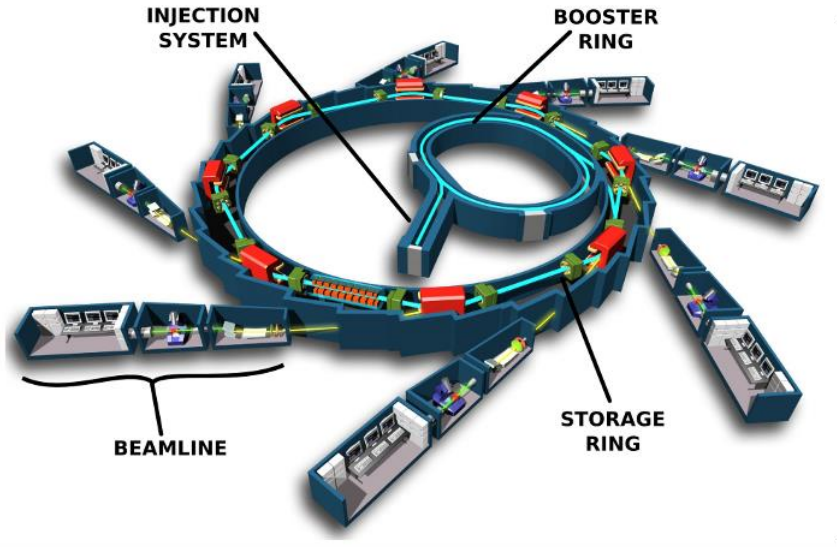

Figure 3. 9 Principle features of a synchrotron facility showing the path of synchrotron radiation.

High energy X-ray diffraction (HEXRD) experiments in this study were performed at BL04-MSPD beamline of ALBA Synchrotron Light Laboratory (Figure 3. 10). In-situ continuous heating was applied up to 773 K (500 °C) with a heating rate of 10 K/min and the corresponding phase changes were observed. Samples in powder form were sealed into 1 mm diameter borosilicate capillaries. These specimens were exposed to X-rays with a wavelength of 0.4962 Å. Room temperature data were collected from free-standing specimens in the 2θ range of 0.6-20°, where θ is the Bragg's angle, using Mythen array detector system.

Figure 3. 10 BL04-MSPD beamline in ALBA Synchrotron Radiation Light Source.

d) Magnetic Measurements

Magnetic properties were measured by vibrating sample magnetometer (VSM) under an applied field of 2 Tesla at room temperature. Detailed information on VSM is already provided in Chapter 2.6.4. Samples are placed in between magnetic coils and the change in the magnetic induction is monitored. Magnetic properties, such as coercivity and remanence are evaluated through the resultant hysteresis curves.

3.4. RESULTS AND DISCUSSION

The compositions were purposely selected to represent possible τ-phase forming chemistries according to MnAl phase diagram [87] and named as S1, S2, S3 and S4. Each specimen was solutionized at 1423 K (1150 °C) for an hour and quenched in water subsequently. Single ε-phase was observed in all samples within the resolution limit of CuKα as shown in Figure 3. 11. The nominal chemistries were verified using EDS and the results were tabulated in Table 3. 1.

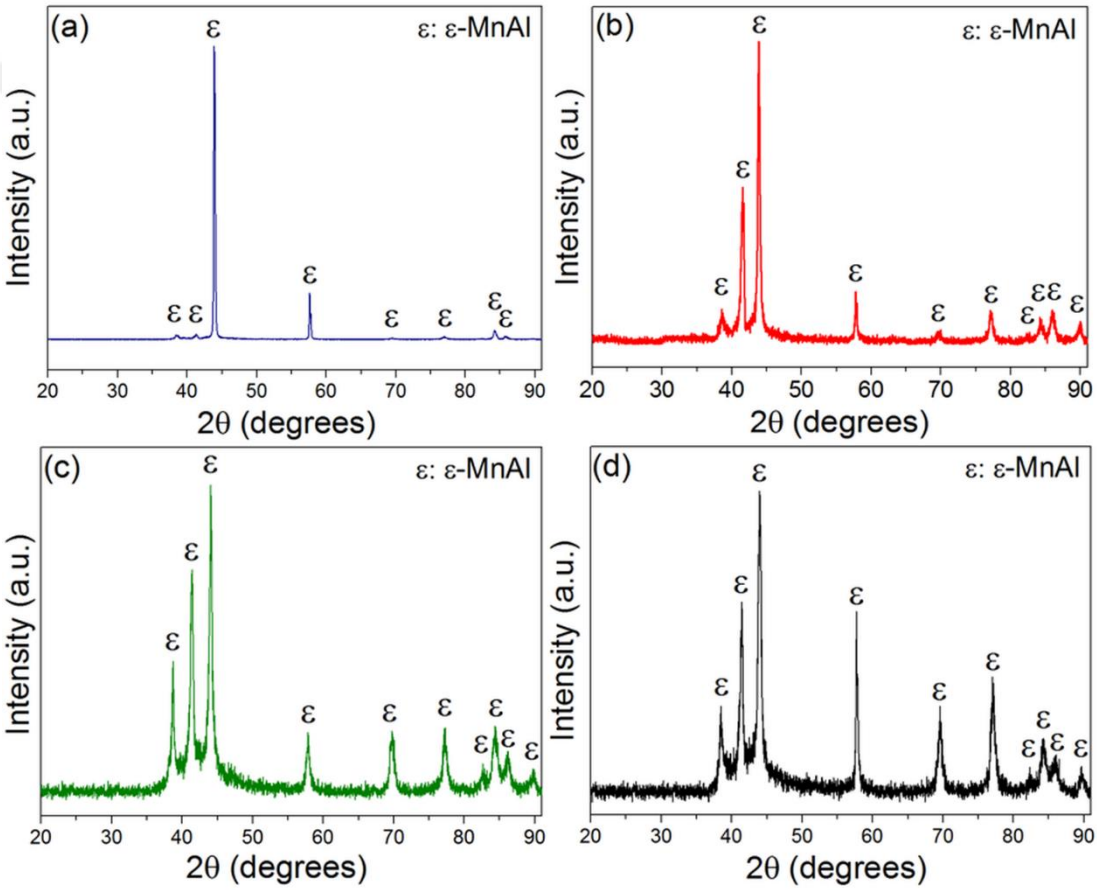

Figure 3. 11 Conventional XRD spectra of sample (a) S1, (b) S2, (c) S3, and (d) S4 after solutionizing.

Table 3. 1 EDS results of the samples S1, S2, S3, and S4. Mn and Al ratios of the alloys are given in atomic and weight percentages.

Sample Name	Mn		Al	
	wt%	at%	wt%	at%
S1	67.5 ± 0.3	50.55 ± 0.3	32.55 ± 0.3	49.55 ± 0.3
S2	70.0 ± 0.2	53.4 ± 0.2	30.0 ± 0.2	46.6 ± 0.2
S3	71.5 ± 0.1	55.2 ± 0.1	28.5 ± 0.1	44.8 ± 0.1
S4	73.0 ± 0.5	57.0 ± 0.5	27.0 ± 0.5	43.0 ± 0.5

3.4.1. Synchrotron Analyses

Figure 3. 12 shows the HEXRD data on 2D-films obtained while heating the solutionized alloys from room temperature to 500 °C with a heating rate of 10 °C/min within a furnace attached to the synchrotron beamline. Diffraction patterns were found to be different for alloys with less Mn (S1 and S2) and for the alloys with larger amounts of Mn (S3 and S4). A broad peak having low intensity was observed around 9° (2θ) in S1 and S2, whereas that signal was missing for the specimens S3 and S4. It is known that ε and the intermediate ε'-phase have overlapping diffraction patterns. The only characteristic peak of ε'-phase is at 8.9° (2θ). 2D synchrotron film plots suggest that ε' and ε-phase were present at room temperature in S1 and S2, on the other hand; as-quenched state of S3 and S4 had only ε-phase.

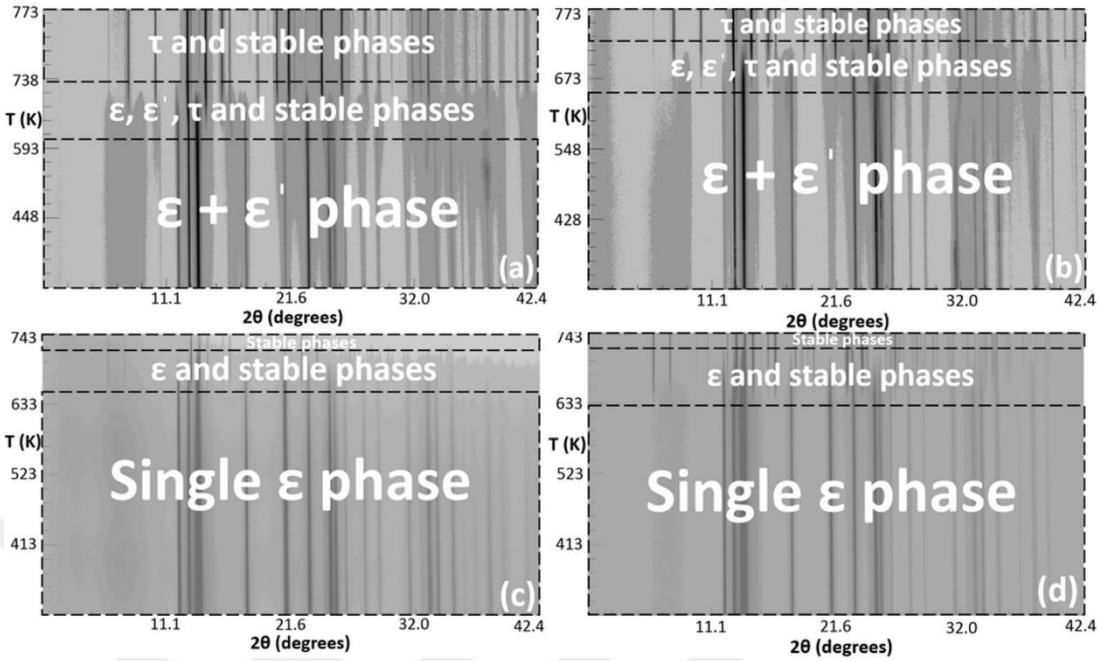

Figure 3. 12 2-D film synchrotron plots of (a) S1 (b) S2, (c) S3 and (d) S4.

The sequence of phase transformations was found to be similar in S1 and S2 while it was different for S3 and S4 specimens. Figure 3. 12(a) and (b) shows that ε and ε' slowly disappear and the peaks of metastable τ-phase appear upon heating. ε+ε' matrix completely diminishes after 467°C. τ-phase formation was followed by the stable non-magnetic phases at elevated temperatures. On the contrary, in S3 and S4 alloys (Figure 3. 12(c) and (d)) room temperature ε-phase directly transforms into stable phases with increasing temperature, surpassing the ferromagnetic τ-phase transformation.

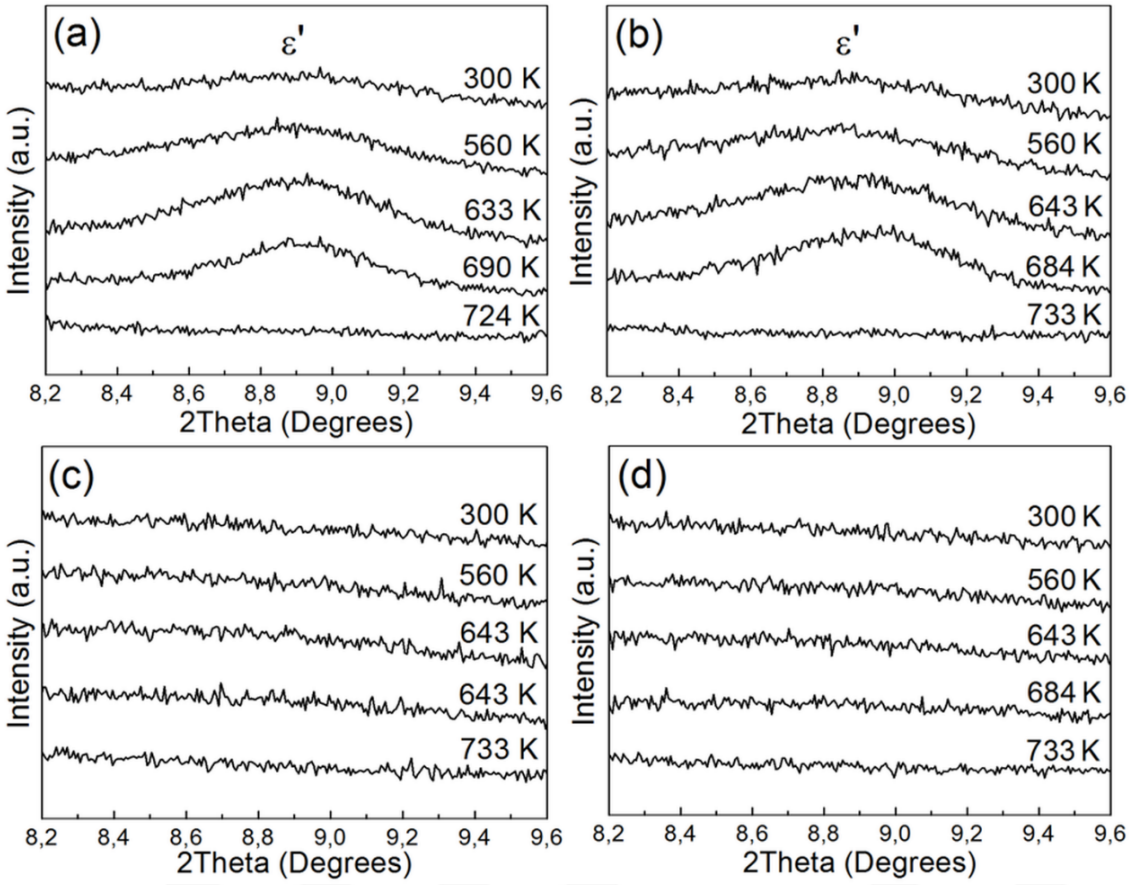

Figure 3. 13 HEXRD patterns of the alloys (a) S1, (b) S2, (c) S3 and (d) S4 within 8,2 -9,6° a 2Θ range of 8.2-9.6° showing the evolution of ε' peak at different temperatures.

Detailed representation of the high energy X-ray pattern shows the change in the ε'-phase peak intensity with respect to temperature (Figure 3. 13). Increasing annealing temperature leads to a growing intensity of the peaks of the ε' phase in S1 and S2 alloys. It is clearly seen that ε'-phase was already present in quenched state for S1 and S2. In alloy S1 (Figure 3. 13a), the hump at room temperature around 8.9° (2Θ) sharpens at 633 K (360°C) and vanishes around 724 K (451°C). In alloy S2 (Figure 3. 13b), a similar pattern was observed but the temperature at which the hump grows into a peak was different. The intensity of ε'-peak reaches its maximum value at 684 K (411°C) and then the peak disappears completely at 733 K (460°C). This suggests that matrix has already ε' nuclei at room temperature. It is not certain whether ε→ε'

ordering takes place or already-present ε' nuclei grow with increasing temperature but it is clear that growth or ordering takes place only up to a certain limit and ε' disappears with further increase in temperature.

It should also be noted that the intensity of the ε'-peak in S1 and S2 was relatively low that it is very difficult to distinguish its presence by any characterization technique other than high energy XRD. Characteristic ε' peak at 8.9° (2Θ) corresponds to 27° (2Θ) in conventional XRD (CuKα). It is likely that Figure 3. 11(a) and (b) have an ε' peak at 27° (2Θ); but, it is not possible to detect due to its low intensity.

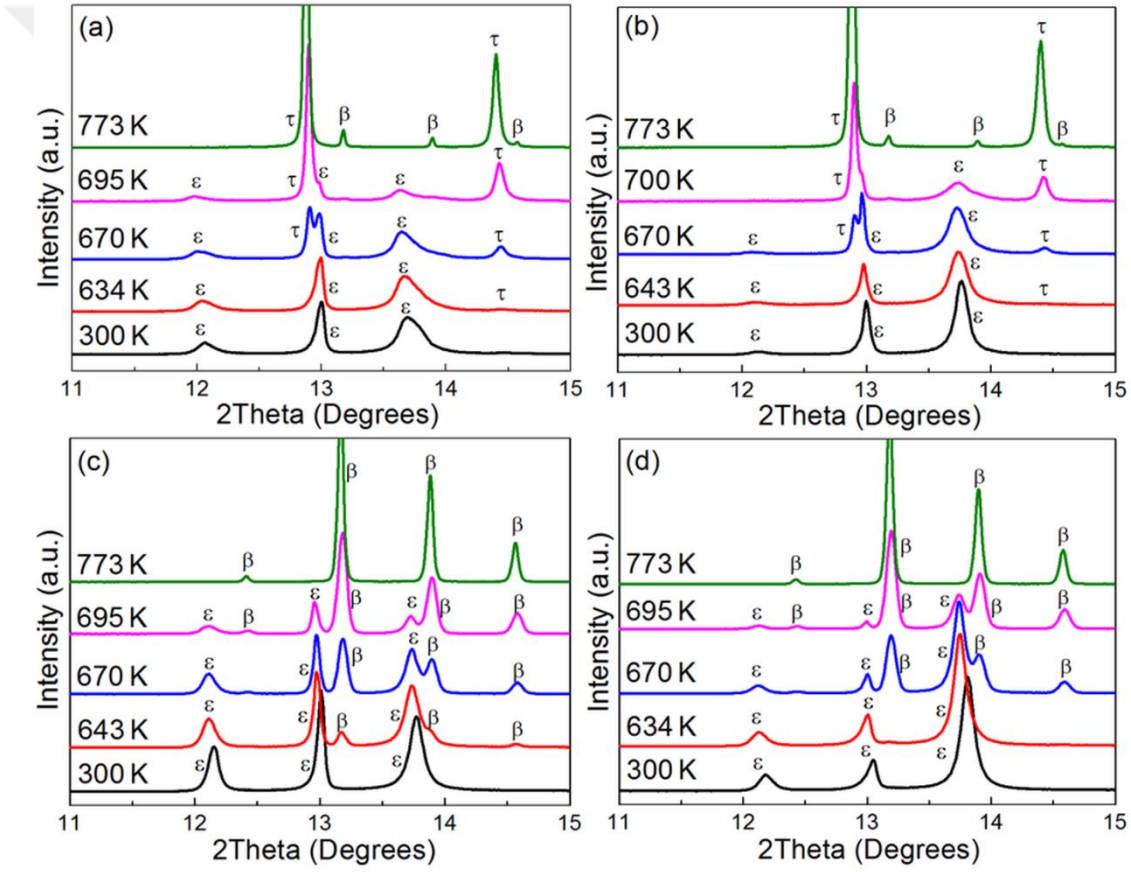

Figure 3. 14 HEXRD patterns of the alloys (a) S1, (b) S2, (c) S3 and (d) S4 within a 2Θ range of 11-15° showing the formation of τ-MnAl peak upon heating.

HEXRD patterns of the alloys S1, S2, S3 and S4 between 2θ values of 11-15° is provided in Figure 3. 14. In alloys S1 and S2, ferromagnetic τ-phase forms with increasing temperature (Figure 3. 14(a), (b)). Upon annealing, peak intensities of the ε and ε'-phases decrease and τ-phase increases. This corresponds to a decreasing phase content and indicates that the ε'+ε matrix is transforming into τ-phase. However, in alloys S3 and S4, the τ-phase peaks were not observed (Figure 3. 14(c), (d)). The change in transformation scheme indicates the significance of the ε'-phase in terms of τ-phase formation. When ε'-phase was absent at the quenched state, as in the case of S3 and S4 alloys, τ-phase cannot be obtained. It is likely that ε'-phase serves as nucleation sites for the τ-phase.

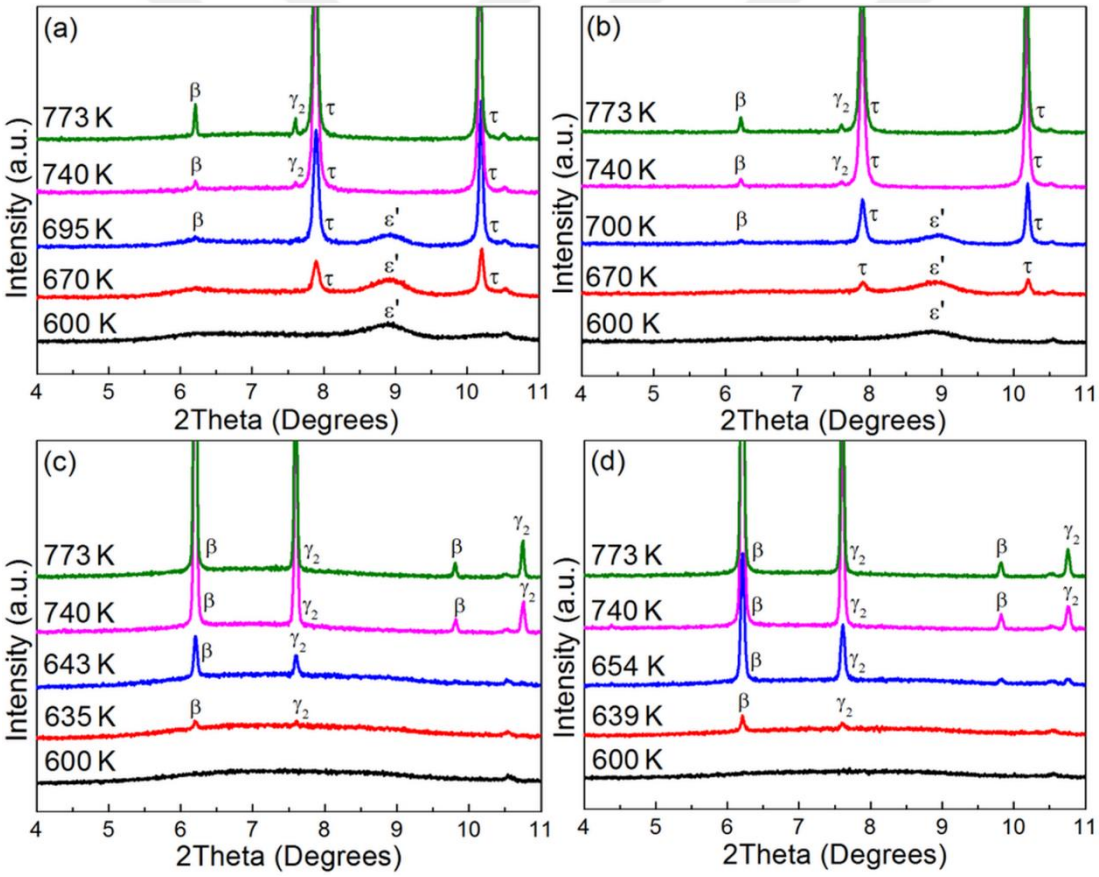

Figure 3. 15 High energy X-ray diffraction patterns of the alloys (a) S1, (b) S2, (c) S3 and (d) S4 within 4-11° (2Θ) range showing the formation of the stable phases upon heating.

Figure 3. 15 shows the high energy X-ray diffraction patterns of the alloys S1, S2, S3 and S4 between 4-11° (2θ). It is observed that prolonged annealing results in decomposition of the τ phase to the equilibrium γ2 and β-Mn phases. Stable phases were formed in all samples independent of composition. It is observed that β-Mn is formed earlier than γ2 phase. Therefore, it can be concluded that the decomposition is a two-step reaction which is in good agreement with the literature [108]. Figure 3. 15 also indicates that the transformation temperatures vary with the composition. Formation and stability range of each phase is listed in Table 3. 2. ε+ε' matrix transforms into τ-phase at 633 K (360°C) and 643 K (370°C) for S1 and S2, respectively (Figure 3. 15 a, b) whereas stable non-magnetic phases form subsequently at 695 K (422°C) and 700 K (427 °C) (Figure 3. 15a, b). Hence, there is a difference of 55-60 K between the formation of τ-phase and equilibrium phases.

Temperature at which stable phases formed was around 695 K (422°C) for S1 and S2 alloys while transformation temperature decreases to 635 K (362°C) for samples S3 and S4 (Figure 3. 15c, d). This suggests that presence of ε'-phase not only promotes the τ-phase formation but also retards the transformation to the stable phases. Formation temperatures and stability range of each phase is listed in Table 3. 2.

Table 3. 2 Critical transformation temperatures of ε, ε', τ and stable phases.

Sample Name	**Phase Type and Range**			
	ε	**ε'**	**τ**	**Stable Phases**
S1	300-741 K (27-468°C)	300-633†-724 K (27-360†-451°C)	634-773 K (361-500°C)	695-773 K (422-500°C)
S2	300-740 K (27-467°C)	300-643†-733 K (27-370†-460°C)	643-773 K (370-500°C)	700-773 K (427-500°C)
S3	300-729 K (27-456°C)	-	-	635-773 K (362-500°C)
S4	300-729 K (27-456°C)	-	-	639-773 K (366-500°C)

†Temperature at which ε' peak starts to intensify.

3.4.2. Differential Scanning Calorimetry Analysis

DSC analysis was carried out to identify the thermal behavior of the samples. A similar experimental procedure with synchrotron analysis was used in DSC experiments for comparison and correlation with the HEXRD data. As-quenched samples were annealed up to 500 °C with a heating rate of 10 K/min in DSC and quenched to maintain the microstructure. The purpose of using similar heating rates was to mimic HEXRD experiments so that isochronal phase changes can be identified. XRD analysis prior to DSC experiments confirmed that ε-phase was obtained at room temperature. The heating curves obtained in DSC are given in Figure 3. 16. Most distinctive differences are the shape of the curves and the positions of the peaks. The heating pattern of the S1 and S2 are similar to each other; but, different than S3 and S4. For S1 and S2, a small hump at around 520 K (247°C) was followed by a peak at around 680 K (407°C). This finding is in good agreement with the synchrotron data showing a low intensity ε' diffraction peak at 8.9° (2Θ) in specimens S1 and S2 (Figure 3. 13(a) and (b)). The increase in the intensity of the ε' peak was attributed to the growth of ε' nuclei. It is likely that the hump observed in DSC scans of S1 and S2 alloys (520 K-247 °C) corresponds to the growth of the ε'-phase. The small hump was missing in the DSC scans of specimens S3 and S4 and the major peak was observed at a relatively lower temperature (640 K-367°C). HEXRD patterns of S3 and S4 (Figure 3. 13(c) and (d)) do not show a Bragg reflection at 8.9° (2Θ), which confirms the absence of ε'.

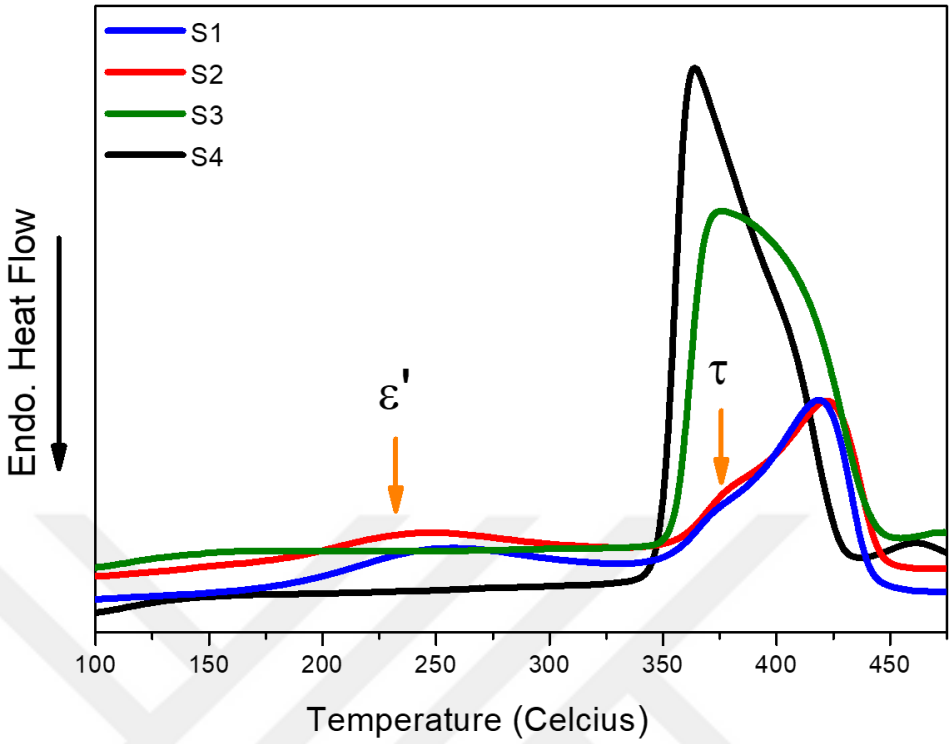

Figure 3. 16 DSC heating curves of S1, S2, S3 and S4 with a heating rate of 10 K/min from room temperature to 773 K (500 °C).

Heating path of S1 and S2 alloys suggests an overlap of the main peak with a shoulder peak appearing at 650 K (377°C). The shoulder peak is marked with an arrow on Figure 3. 16. Correlating with the synchrotron data (Figure 3. 15(a) and (b)), it can be speculated that the shoulder peak in S1 and S2 specimens correspond to the formation of τ-phase. On the other hand, DSC heating curve of S3 and S4 was found to display a sharp single peak leaning towards lower temperatures. The shoulder peak is absent in S3 and S4. The remaining transition can be attributed to the formation of stable phases. This finding is in good agreement with the XRD data presented in Figure 3. 15(c) and (d) indicating that only stable phases are formed and τ-phase is missing.

b) Activation Energy Determination

In order to observe the effect of the composition on activation energy, isochronal kinetic analyses were carried out on samples S1, S2 and S4. Alloys were heated from room temperature to 500°C with heating rates of 10, 20, 30, and 40 °C/min. Heat flow

is plotted with respect to temperature. A baseline was interpolated and subtracted from the original data. All DSC traces were fitted into Gaussian function using OriginPro 9.0 software and converged Gaussian fit of experiments with a heating rate of 10 °C/min and DSC data is provided in Figure 3. 17(a) and (b), respectively.

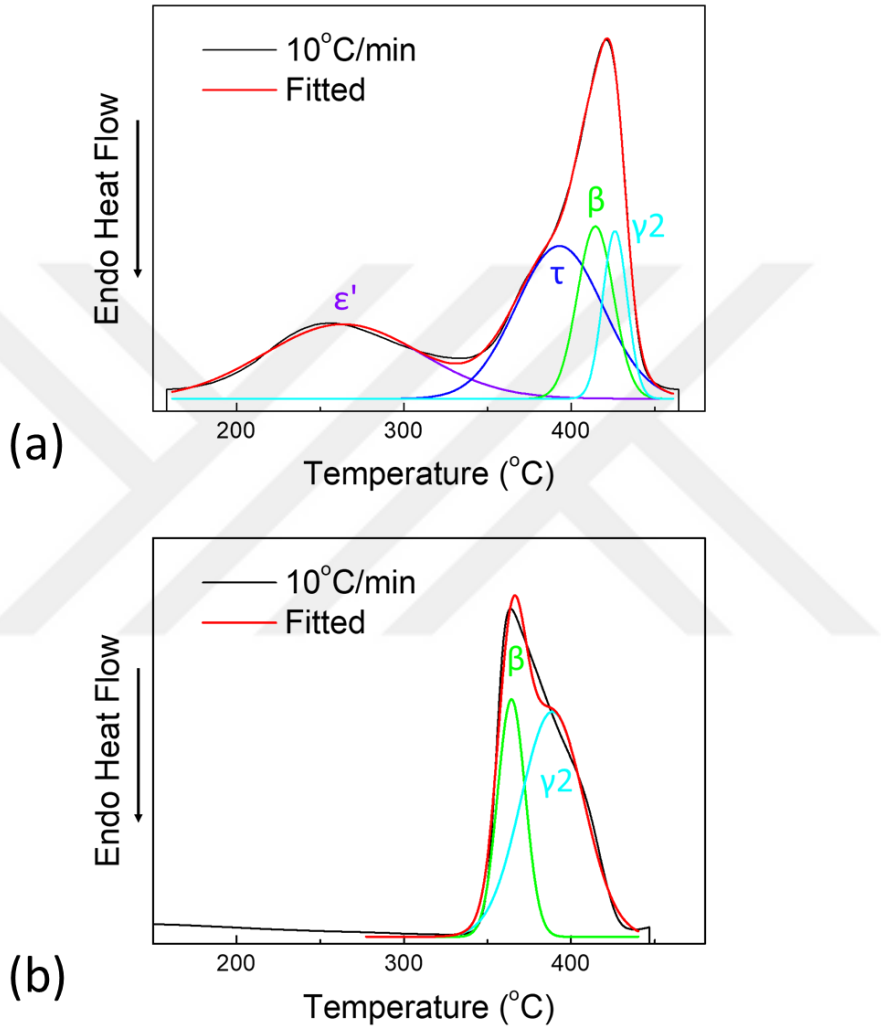

Figure 3. 17 Gaussian fitted DSC scans for (a) S1 alloy and (b) S4 alloy both with a heating rate of 10 °C/min. Black line represents the original data and red line represents the Gaussian fit.

Overlapping peaks were deconvoluted. In correlation with in-situ HEXRD experiments, DSC scans of S1 and S2 alloys suggest that ε' transformation takes place at a relatively low temperature and this transformation is followed by ferromagnetic τ-

phase formation. With increasing temperature at around 450°C, stable phases, β and γ2 forms subsequently. It is observed that the fitted curves of S4 has only two deconvoluted peaks suggesting the transformation into stable phases (Figure 3. 17b). Critical temperatures required for Kissinger and Ozawa analyses are determined from the fitted curves. Onset, peak and offset temperatures of each alloy are listed in Table 3. 3.

Table 3. 3 Onset, peak and offset temperatures of S1, S2 and S4 alloys heated at a rate of 10°C in DSC.

Sample	**Phase**	**DSC Temperature (°C)**		
		onset	Peak (Tp)	offset
S1	ε'	172	266	368
	τ	340	393	446
	β	390	414	
	γ2	410	426	
S2	ε'	178	257	341
	τ	348	396	467
	β	394	419	
	γ2	412	432	
S4	β	344	364	
	γ2	350	388	

Kissinger and Ozawa plots were constructed as explained in Chapter 3.3.3. For a set of DSC curves with different heating rates ln(Rate/T_p^2) was plotted against 1000/Tp for Kissinger approach and ln(Rate) versus 1000/Tp was plotted for Ozawa analysis. Figure 3. 18(a) and Figure 3. 18(c) shows the corresponding Kissinger and Ozawa plots of S1 and S2 alloys for τ-phase, respectively. Figure 3. 18(b) and (d) shows the

corresponding Kissinger and Ozawa plots of S1 and S2 alloys for β-phase. The slope of the curves determine the activation energy as explained in Chapter 3.3.3.

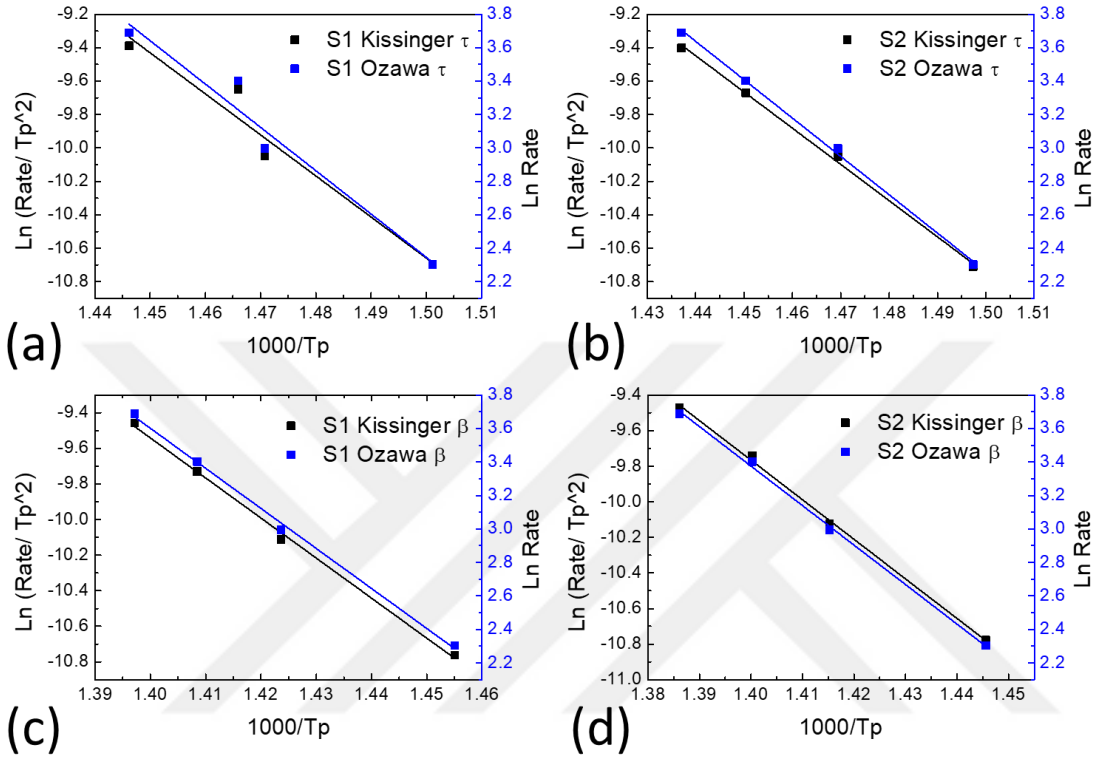

Figure 3. 18 Kissinger and Ozawa plots for (a) S1 alloy τ-phase, (b) S2 alloy τ-phase, (c) S1 alloy β-phase and (d) S2 alloy β–phase.

The activation energies calculated using Kissinger and Ozawa approaches are similar and these values are tabulated and provided in Table 3. 4. Energy that is required to initiate τ-MnAl transformation is found to be similar to the activation energy of stable phase transformation. It is observed that stable phases of S1 and S2 alloys have higher activation energies than S4 alloy. It may be related to the fact that the formation temperature of stable phases are 60°C lower for S4 alloy as indicated in Table 3. 2. Stable phases in S4 alloy, having a lower activation energy, forms readily at a lower temperature. This suggests that ε' not only promoted the ferromagnetic τ-phase but also stabilized it by delaying the formation of cubic equilibrium β and γ2 phases.

Table 3. 4 Calculated activation energies for S1, S2 and S4 samples with Kissinger and Ozawa approaches.

Phase	Kissinger E_a (kJ/mol)			Ozawa E_a (kJ/mol)		
	S1	S2	S4	S1	S2	S4
τ-MnAl	204	194	-	215	205	-
β-MnAl	187	194	115	199	206	126
γ2	181	191	110	193	203	122

3.4.3. Magnetic Measurements

Magnetic hysteresis curves obtained for the samples after DSC analysis are given in Figure 3. 19. Alloys S1, S2, S3 and S4 were heated from room temperature to 500 °C with a heating rate of 10 °C/min under N_2 gas atmosphere and quenched subsequently. Magnetic properties of those samples were measured by vibrating sample magnetometer (VSM). According to HEXRD spectra presented on Figure 3. 15, S1 and S2 have ferromagnetic τ-phase and stable phases while S3 and S4 should have only stable phases. As expected, alloys S1 and S2 showed ferromagnetic behavior due to the presence of τ-phase (Figure 3. 19). Coercivity and remanence of S1 was found to be 640 Oe and 23 emu/g, respectively. S2 had relatively stronger magnetic behavior having a coercivity of 1560 kOe and remanence of 26 emu/g. BH_{max} values of S1 and S2 are calculated to be 0.76 and 0.34 MGOe, respectively (Figure 3. 20). On the other hand, S3 and S4 were paramagnetic in nature as τ-phase was not observed. With further increase of Mn, ε'-phase diminishes and thus, τ-phase cannot be obtained.

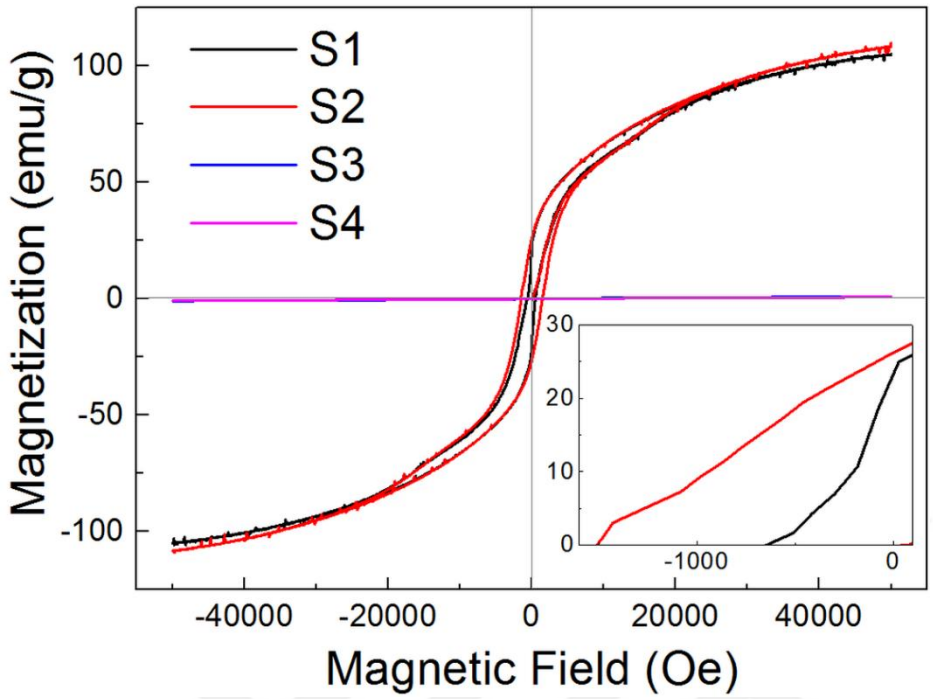

Figure 3. 19 Hysteresis curves of S1, S2, S3 and S4. Inset shows the second quadrant of the B-H curve of S1 and S2 specimens.

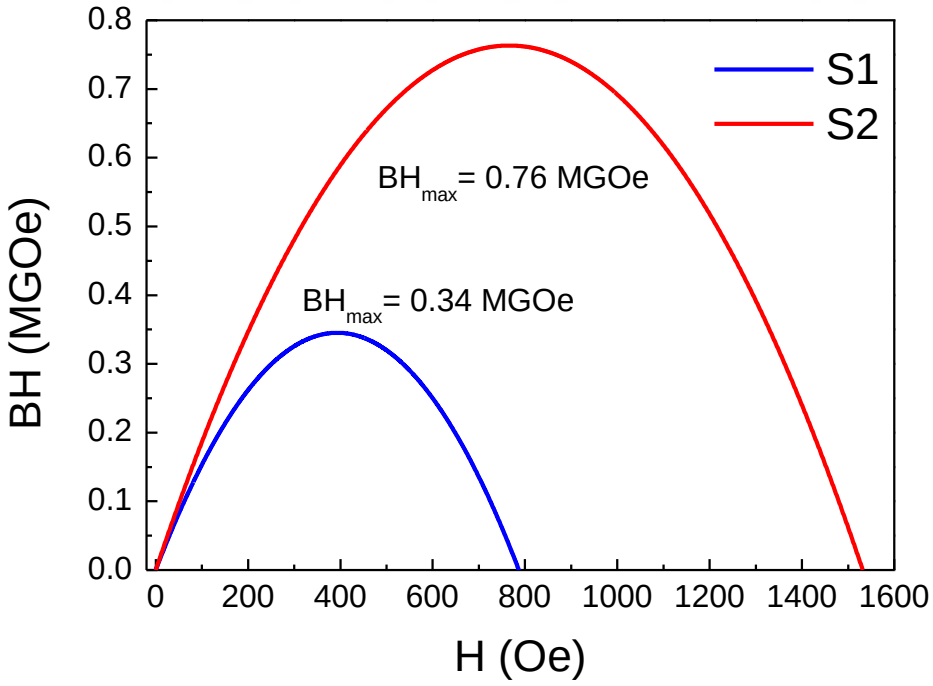

Figure 3. 20 Dependence of energy product on field strength for samples S1 and S2.

3.4.4. Transmission Electron Microscopy Analyses

In order to study the growth behavior of τ-phase, advanced morphological and microscopic analyses were conducted on the synchrotron samples. TEM samples were prepared from alloys S1, S2, S3 and S4 using focus ion beam (FIB) microscopy as discussed in Chapter 3.3. Bright field TEM micrographs on Figure 3. 21 revealed the presence of a defected like matrix. Crystal structure of the ε is known to be hexagonal. By considering the allowed and forbidden reflections, {hkl} indices are determined. The resulting diffraction patterns are in good correlation with the synchrotron data thereby, the presence of ε at room temperature has been confirmed.

At high magnifications, an analysis of the atomic scale images reveals the presence of several defect-like structures in various regions of the microstructure. It is already known from the synchrotron analysis that S1 and S2 should consist of ε and ε'-phases. It is speculated that the defected region is ε'-phase, whereas the matrix consists of large ε-phase grains.

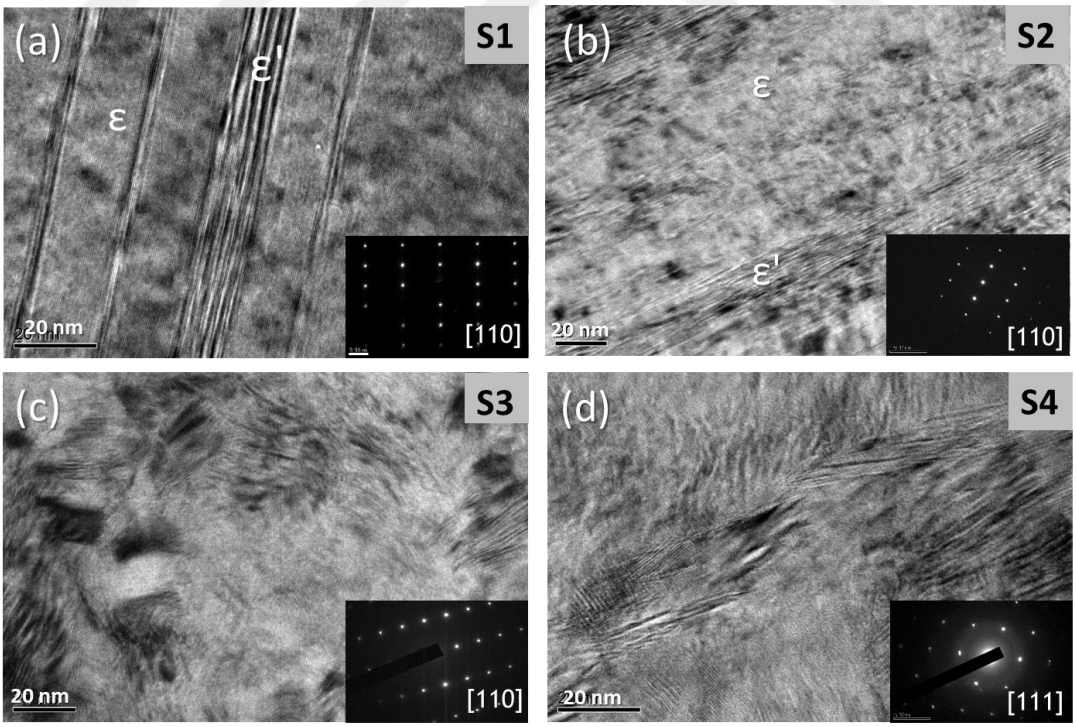

Figure 3. 21 Bright field TEM images of samples (a) S1 (b) S2 (c) S3 (d) S4, insets showing the selected area diffraction patterns and zone axes.

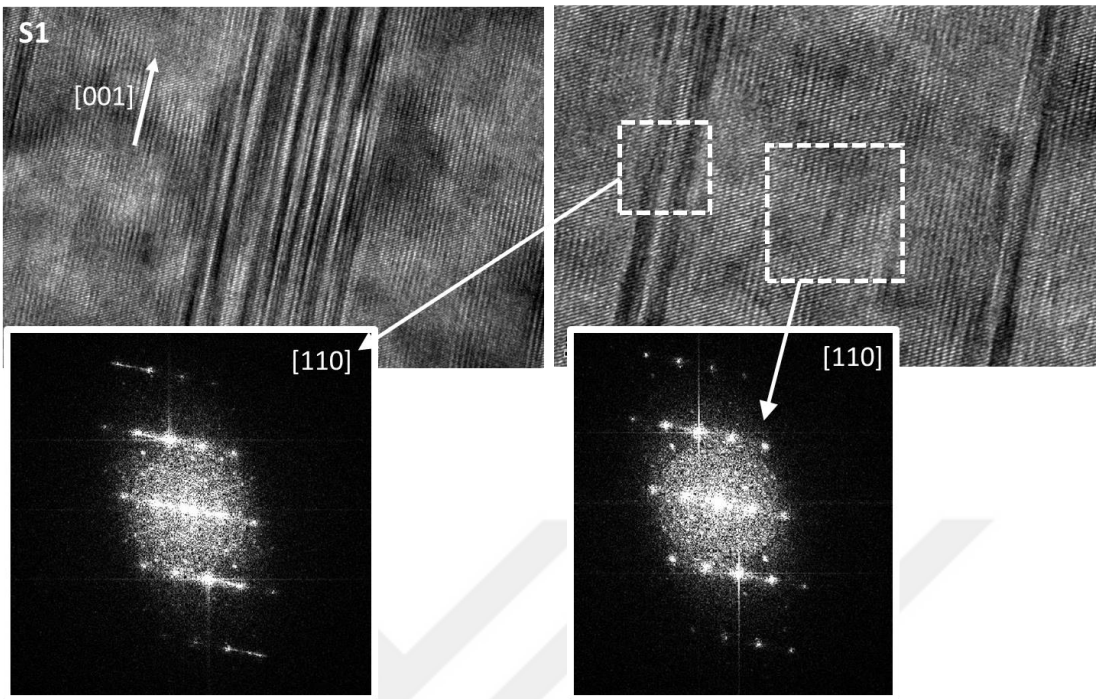

Figure 3. 22 HRTEM images and corresponding FFT images obtained from S1.

HRTEM images and corresponding fast Fourier transform (FFT) images obtained from the sample S1 ($Mn_{67.5}Al_{32.5}$) are provided in Figure 3. 22. Fast Fourier transform (FFT) of an HRTEM image carry a similar information to diffraction patterns observed on TEM as they both represent reciprocal lattice. Fast Fourier transformation basically consists of applying an algorithm to the corresponding TEM image (real space) and obtaining the diffraction pattern in reciprocal space. FFT is performed on the HRTEM images to identify the nature of the distortion; however, a distinct change in crystal structure is not observed. Thin plate-like ε'-phase cause long streaks in the diffraction pattern. In our study, the direction of the ε' is determined to be [001] as provided in Figure 3. 22.

In order to theoretically visualize the cell and index the diffraction patterns, Carine software was used. The relationship between ε and ε' is well established in literature and explained in detail on Chapter 3.2. Among three variants of ε'-phase, variant 1 (ε'_1) $(0001)\varepsilon$ // $(001)\varepsilon'$ and $[11\bar{2}0]\varepsilon$ // $[010]\varepsilon'$ was selected as it is the major variant that yields τ-phase according to the study of Wiezorek and coworkers [111]. Epitaxial

relationship parameters were adjusted accordingly in Carine software and the resulting images are presented in Figure 3. 23.

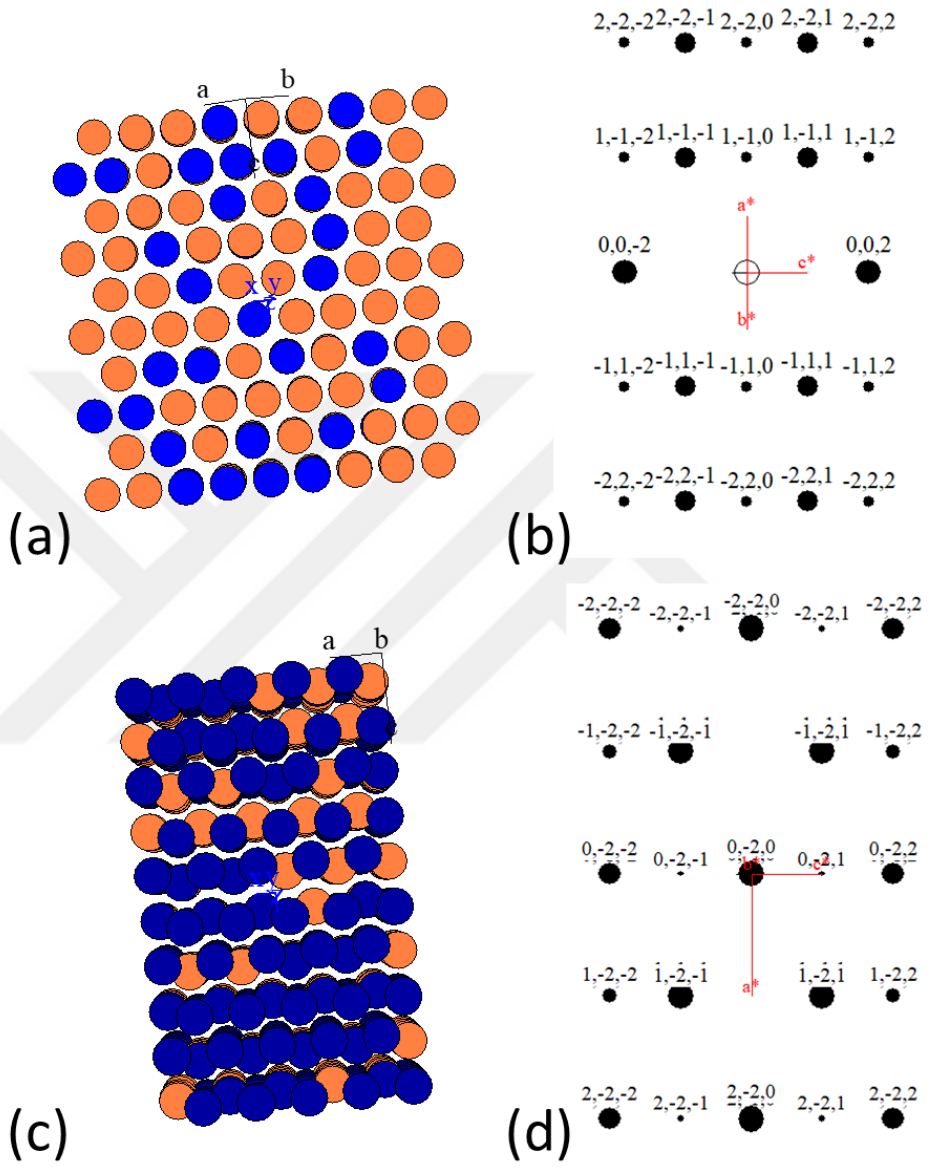

Figure 3. 23 (a) Schematic illustration of the ε-phase atomic structure along [110] zone axis, (b) corresponding diffraction pattern of ε along [110] zone axis, (c) atomic structure of ε' when rotated along ε [110], (d) corresponding diffraction pattern of ε' when rotated along ε [110].

It is observed that when ε' structure is rotated along ε (110), theoretical diffraction patterns of ε and ε'-phases are almost the same. Thereby, it becomes difficult to distinguish between two phases. In order to identify ε'-phase, another zone axis must have been used. The possible zone axes to identify ε' phase from diffraction pattern were determined as (001), (100) and (111) from Carine software. However; within the limits given by the tilt angle of 30° in TEM, we couldn't manage to tilt the sample into these zone axes from (110) zone axes.

A 2D simulation model of ε and ε' phase is created and the orientation relationship between ε and ε' is applied to QSTEM (Quantitive scanning transmission electron microscopy) image simulations (Figure 3. 24). QSTEM is a code for simulating TEM and STEM images using a multislice algorithm [120]. The software includes seven different tools namely; convert2cfg, gbmaker, imageSim, qmb, qstem, showimage and virtualGoniometer. Firstly, a box of atoms is created through a configurational file of atomic weights, atom positions of Mn and Al. Gbmaker (grain boundary maker) tool uses this simulation box in order to create a-new input for qstem program. Qstem tool slices the simulation box into used to many sections along their zone axis in order to represent the selected crystallographic defects in TEM and STEM images.

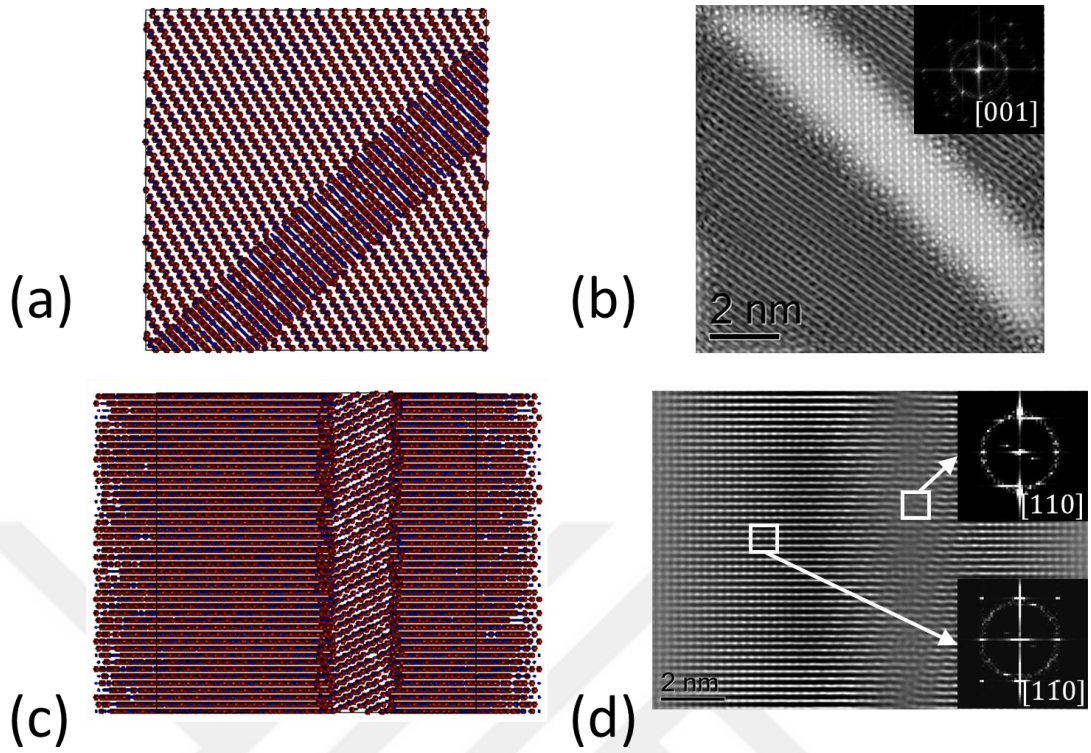

Figure 3. 24 (a) 2D model of MnAl box with ε' variant oriented along [001] zone axis, (b) HRTEM image simulation of MnAl box with ε' variant along [001] zone axis; inset showing the FFT image, (c) 2D model of MnAl box with ε' variant oriented along [110] zone axis, (d) HRTEM image simulation of MnAl box with ε' variant oriented along [110] zone axis. The insets show FFT images of the marked areas.

2D model of the simulation box is oriented along [001] zone axis as in Figure 3. 24(a) and the corresponding HRTEM image simulation is shown in Figure 3. 24(b). The inset shows the FFT image. 2D model of the simulation box is then oriented along [110] zone axis Figure 3. 24(c) and the corresponding HRTEM image simulation of MnAl box with ε' variant oriented along [110] zone axis is provided in Figure 3. 24(d). The insets show FFT images of the marked areas. No significant changes has been observed between the ε' and ε-phase. This finding confirms that it is difficult to identify ε'-phase through diffraction pattern analysis along [110] zone axis.

When TEM analysis is correlated with synchrotron analysis, it is observed that ε'-phase is present at quenched state in S1 and S2 alloys. The presence of ε'-phase in S1 and S2 alloys can be explained by several theories. In one theory, ε'-phase may have been formed at high temperatures and retained at quenching. As ε' is a metastable phase, it is not shown on the phase diagram. XRD pattern of ε and ε'-phases are almost the same, there is only a few different peaks and their intensities are relatively low even under synchrotron radiation. Thereby, it is not possible to detect the presence of ε'-phase at high temperatures through conventional XRD (CuKα) techniques. In another theory, ε' may have been formed during quenching. It is already known from the literature that ε'-phase is an ordered derivative of the ε-phase. It is likely that ordering destroys the cubic symmetry during quenching. The defect like morphology of the ε'-phase may as well be due to a lattice contraction during ordering.

In order to understand and visualize the temperature effects on ε→τ transformation, in-situ heating TEM experiments were carried out as explained on Chapter 3.3. A τ forming composition (S2) and a composition that doesn't yield τ-phase (S4) are selected for comparison. Still frames extracted from the dynamic video sequence during in-situ heating TEM experiment of sample S2 are presented in Figure 3. 25. A dense pattern of planar defects were observed at room temperature. It is hypothesized that the planar defects are ε'-phase as it is already confirmed in DSC and synchrotron analyses that ε'-phase and ε-phase coexist in the same matrix. As temperature increases, defect arrays (ε') become denser and eventually transforms into τ-phase at 390°C. Upon further annealing, stable phases readily forms at around 520°C. At 550°C, sample mostly consists of stable phases along with some τ-phase and trace amount of ε-phase residuals.

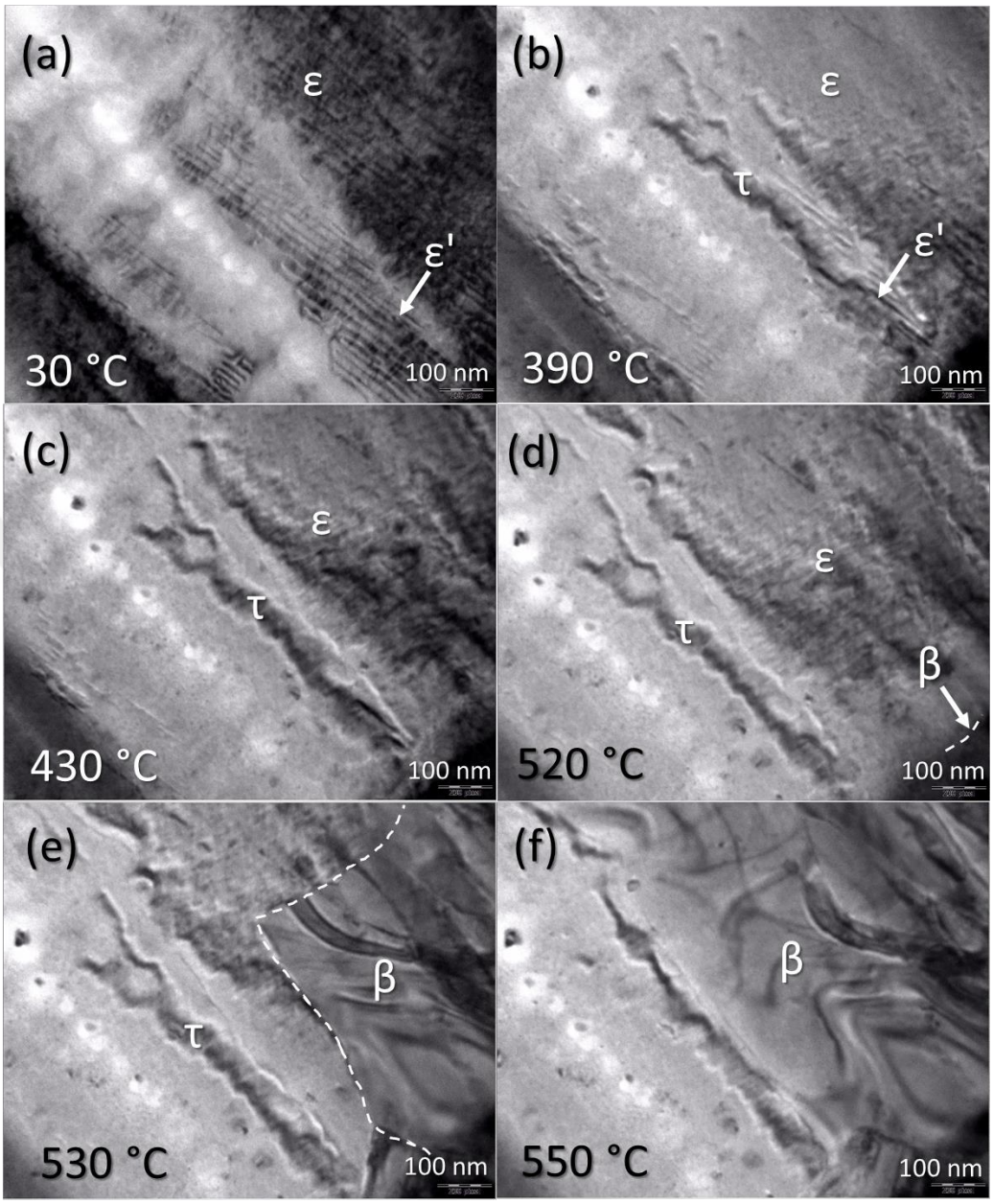

Figure 3. 25 Screenshots extracted from the dynamic video sequence during in-situ heating TEM experiment of S2 at temperatures of (a)30, (b) 390, (c) 430, (d) 450, (e) 460 and (f) 500°C. Dashed lines indicate the grain boundary between ε and β-phases.

Same experiment was carried out for sample S4. Screenshots extracted from the dynamic video sequence in-situ heating TEM experiment of sample S4 are shown in Figure 3. 26. Planar defect arrays observed at room temperature in S2 were missing in case of S4. In good agreement with XRD results, τ-MnAl formation was not observed

and ε-phase directly transformed into stable phases. The transformation temperature found to be lower than S2. Stable phase transformation started at 520°C in S2 whereas, the value dropped to 460°C for S4 alloy. This finding is consistent with the synchrotron and DSC analyses suggesting that ε'-phase retards the stable phase formation. At 550°C, whole sample was decomposed into β-Mn and γ2.

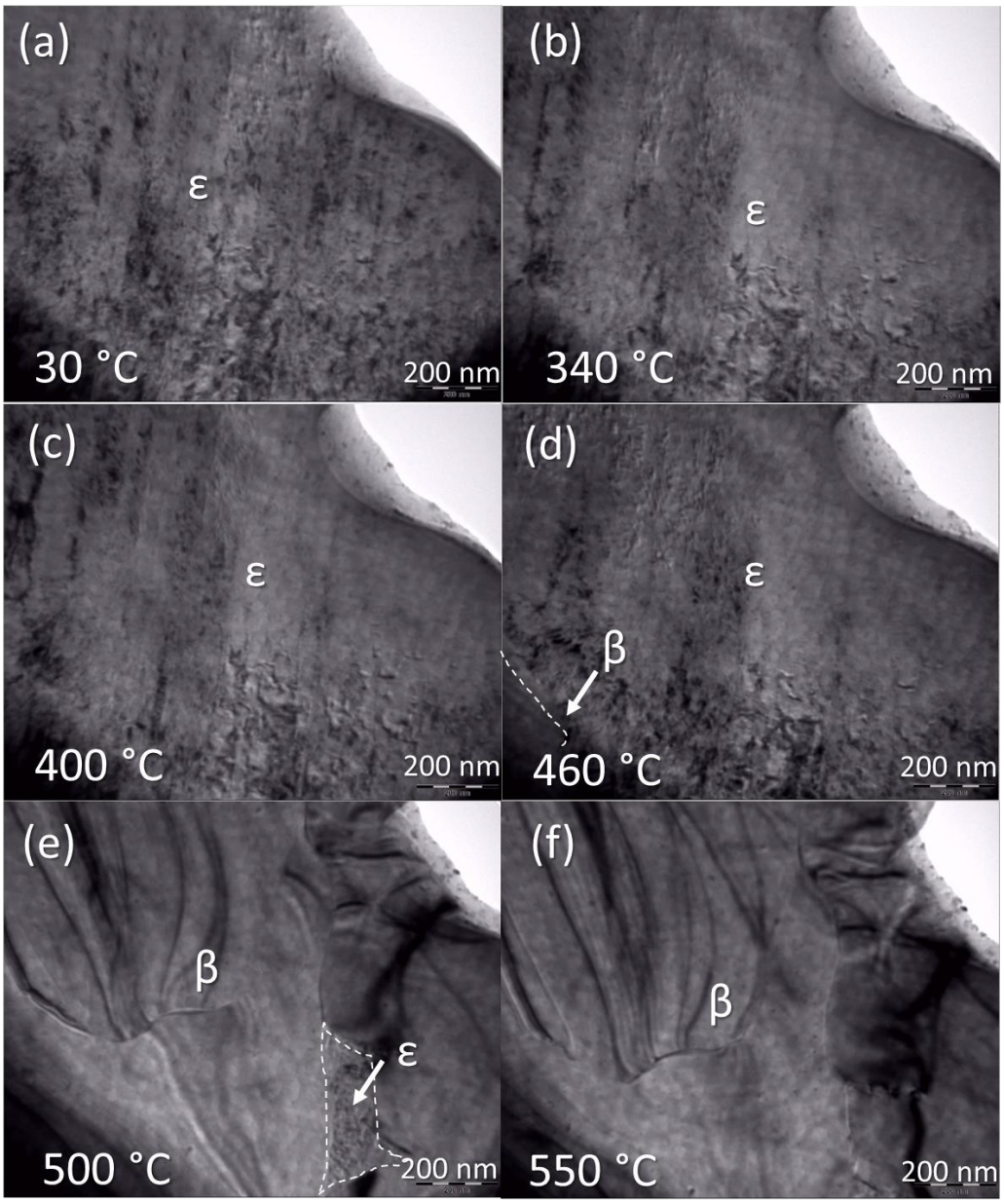

Figure 3. 26 Screenshots extracted from the dynamic video sequence during in-situ heating TEM experiment of S4 at temperatures of (a)30, (b) 340, (c) 400, (d) 470, (e) 480 and (f) 500°C. Dashed lines indicate the grain boundary between ε and β-phases.

Through in-situ TEM experiments, it is speculated that the evolution of the τ-MnAl phase involves a nucleation and growth process wherein, the nucleation takes place heterogeneously along the ε' phase grain boundaries. Grain boundaries with high interfacial energy and relatively weak bonding are often the preferred nucleation sites for heterogeneous nucleation. It is likely that the martensitic shear mechanism is dominant during ε'→τ transformation.

It is once again confirmed that particles of intermediate ε'-phase are not always present in the quenched state. ε'-phase was missing in S3 alloy suggesting that disorder-order reaction is dependent on the composition. Only a certain composition range results in ε'-phase and thereby in ferromagnetic τ-phase. Critical composition range is found to be 70 Mn% by weight. Compositional order do not take place with further increase in Mn content.

The transformation temperatures observed through different characterization techniques are summarized in Table 3. 5. It should be noted that all of the experiments are carried out in varying conditions. The vacuum level, calibration of devices, even the room temperature may affect the accuracy of the data. However, it is still possible to comment on the transformation scheme through the temperature change with respect to the pattern/trend. The overall temperature change in each composition gives a brief idea on the transformation sequence. It is observed that τ-phase forms prior to the equilibrium phases in S1 and S2 alloys. Equilibrium phases simultaneously form a short while after the τ-phase. Therefore, there is only a narrow temperature range in which τ-MnAl is stable without γ2 and β-phases. In order to promote the magnetic properties, one must stay in the temperature range where ε-to-τ transformation takes place while the formation of the β is delayed. It is also observed that equilibrium (β and γ2) phases in τ forming compositions (S1 and S2) form readily compared to the equilibrium phases in compositions without τ phase (S4). This suggests that ε' and τ-phases pin the stable phases and delay their formation.

Table 3. 5 Comparison of the transformation temperatures obtained using various characterization techniques.

Transformation Temp / Composition	Phase	DSC Temperature (°C)			SYNCH Temperature (°C)			in situ TEM Temperature (°C)		
		onset	peak	offset	onset	peak	offset			
S1	**eps pr**	172	266	368	N/A	360	451			
	tau	340	393	446	361	N/A	N/A			
	beta	390	414	N/A	422	N/A	N/A			
	gama2	410	426	N/A		N/A	N/A			
S2	**eps pr**	178	257	341	N/A	411	460	N/A	400	430
	tau	348	396	467	370			390	N/A	N/A
	beta	394	419	N/A	427	N/A	N/A	520	N/A	N/A
	gama2	412	432	N/A		N/A	N/A	520	N/A	N/A
S4	**beta**	344	364	N/A	366			470	N/A	N/A
	gama2	350	388	N/A				470	N/A	N/A

In order to study the growth behavior of τ-phase, TEM analysis is conducted on the interrupted quenched S2 samples at critical transformation temperature values obtained from DSC data (Figure 3. 16). It was observed that a step-like DSC signal around 210°C was followed by a hump at 375°C and the maximum intensity peak appeared at 480°C. Accordingly, S2 alloy was heated up to temperatures of 210, 375, 480°C in DSC and immediately quenched afterwards.

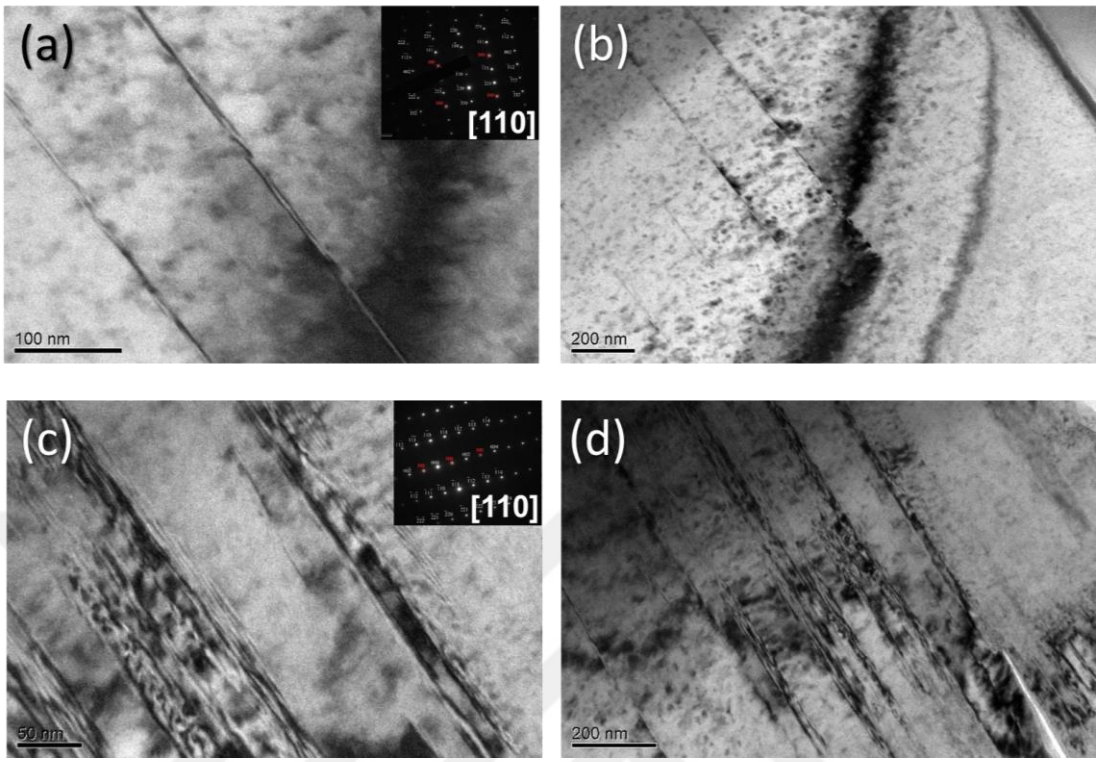

Figure 3. 27 Bright-field TEM images of sample (a), (b) at room temperature and (c), (d) quenched at 210°C. Insets show the diffraction patterns and zone axis.

Similar to Figure 3. 21, stacking fault-like defects along a specific crystallographic orientation was observed at room temperature in Figure 3. 27(a) and (b). The large grains are identified as ε-phase through the diffraction patterns. TEM micrographs of interrupted quenched samples at 210°C consists of large ε-phase grains. At low magnifications, an analysis of the micrographs reveal the increase in the density of defect-like structure throughout various regions of the microstructure (Figure 3. 27(c) and (d)). It has been postulated that further annealing results in increased defect density thereby, creating more heterogeneous nucleation sites for τ-phase formation. The sample was characterized to be paramagnetic at room temperature through VSM measurements.

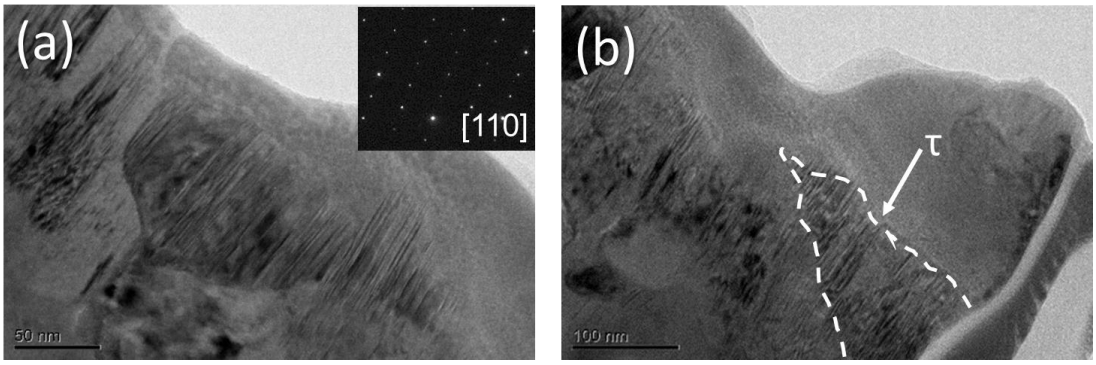

Figure 3. 28 Two bright-field TEM images obtained from different locations on the sample quenched at 375°C. Arrow and dashed line at (b) indicates the morphologically plate-like τ-phase.

Figure 3. 28 shows the BF TEM images of S2 alloy quenched at 375°C. High density of defect-like structures were observed in the ε+ε' matrix along with τ-phase. It can be speculated that this faulting is ε'-phase and it gives rise to the martensitic shear, which transforms' into a ferromagnetic τ-phase. Plate-like morphology of the τ-phase suggests a shear transformation.

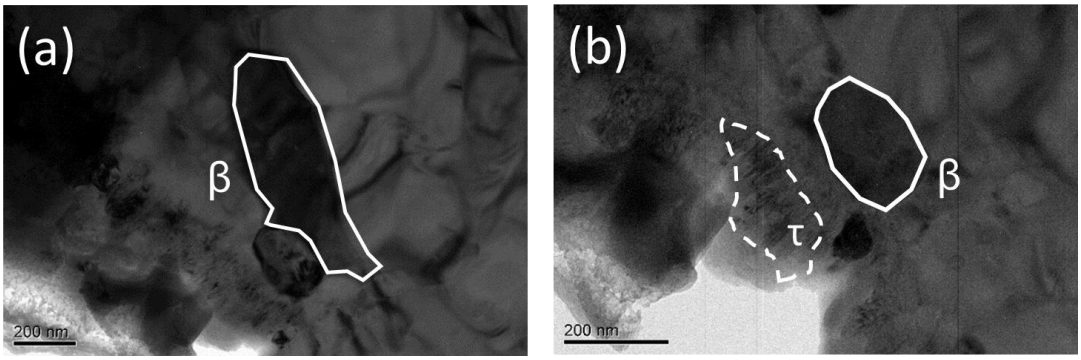

Figure 3. 29 Two bright field TEM images obtained from different locations on the sample quenched at 480°C. The grains marked on (a) and (b) are identified as stable β-phase. Dashed line indicates the morphologically plate-like τ-phase.

Two BF TEM images from different locations on the quenched samples at 480°C were provided in Figure 3. 29. Samples quenched at 480°C consists of morphologically

plate-like τ-phase along with large grains (~200 nm). The sample was tilted to the zone axes and diffraction patterns were recorded. SAED analysis allowed the detailed identification of the phases. The diffraction patterns were indexed and it was determined that all of the grains are β phase which is again consistent with the results obtained from synchrotron analysis, suggesting that the equilibrium phases are formed right after τ-phase.

3.5. CONCLUSIONS

Based upon the results obtained from in-situ HEXRD as well as DSC and magnetic measurements of MnAl-based alloy, phase transformation hierarchy of the compositions that lead to the formation of metastable ferromagnetic τ-phase have been developed.

Previous studies indicated that ε→τ transformation may occur either by massive mode, shear mode or a combination of both (hybrid). Studies suggesting massive transformation claim that shear mechanism is invalid, ε→τ transformation is independent of the ε' ordering and it can proceed without the ε'-phase [104], [113]–[115], [121]. However, the data presented in this work suggests ε'-phase is a strong prerequisite for the formation of τ-phase. Alloys having less Mn (S1 and S2) already had ε'-phase within the ε-matrix at room temperature. It is likely that already-present ε' nuclei grow with increasing temperature up to a limit. ε'-phase disappears with further increase in temperature and transforms into ferromagnetic τ-phase. This finding is in good correlation with shear [77], [101], [104], [105], [107], [122] and hybrid mode studies [111] which state that τ-phase was generated due to the direct shear of the ordered ε'-phase regions.

Overall results indicate that the composition of MnAl-based alloys affect both the sequence and the temperature of phase transformations. Alloys with Mn content less than 70wt% (S1, S2) had a parent phase mixture consisting of ε and ε' phases at the quenched state. It was observed that the peak of ε'-phase becomes narrower during annealing. This finding indicated that room temperature alloys already had ε' nuclei,

which formed during rapid quenching and grow with an increase in temperature. Presence of ε' may have been unnoticed by previous studies due to low intensity peaks at small 2Theta degrees even under synchrotron radiation. Conventional CuKα may fail to identify these peaks. ε'-nuclei may have been formed at high temperatures and retained at quenching or may have been a result of the rapid solidification.

Growth of ε'-phase was followed by a phase transformation into ferromagnetic τ-phase. Prolonged annealing resulted in the decomposition of ε, ε' and τ-phase into stable phases. Alloys containing τ-phase were found to be ferromagnetic via VSM. On the other hand, disorder (ε) to order (ε') reaction is found to be dependent on the composition. Alloys which have more than 70 wt% of Mn (S3, S4) consisted of only ε-phase at the quenched state. Upon annealing, ε-phase directly transformed into equilibrium phases. HEXRD patterns and DSC scans both confirmed that ε'-phase was missing and the formation of τ-MnAl was surpassed. VSM data showed that the samples were paramagnetic due to the absence of τ-phase. This finding suggested that the formation of magnetic τ-MnAl cannot proceed in the absence of ε'-phase and ε'-phase is a strong prerequisite for permanent magnetism in MnAl alloys.

It is observed that compositional ordering do not take place as Mn content increases. Only a certain composition range results in the formation of the ε'-phase and only that composition range results in the τ-phase formation. Mn70% (wt) was found to be the limit for ε' and τ-phase formation. In order to determine the compositional extremities within the τ-phase region, compositions having less than Mn 67% (by weight) should also be examined.

In situ TEM imaging confirmed the transformation sequence of ε+ε'→τ→stable phases for S2 alloy. ε and ε'-phases were observed at room temperature and transformed into τ-phase upon annealing. Stable phases followed τ-phase formation spontaneously. It was speculated that ε-phase first transforms into the ordered ε'-phase. The composition doesn't change and there is a definite orientation relationship between ε' and τ suggesting that τ-phase was formed via martensitic shear of the ε'-phase.

CHAPTER 4

3D PRINTING

4.1. INTRODUCTION

Even though magnetic nanoparticles have better magnetic properties than their bulk counterparts, they can't be implemented into an application in the powders form easily. They need to be compacted into a bulk figure. For this purpose, they must be either sintered or bonded to become suitable for utilization. Many sintered magnets are brittle, hard and difficult to machine to their final forms. On the other hand, polymer-bonded materials are easily machinable and they can be useful as multifunctional elements for different applications.

In this part of the study, it is aimed to create a three dimensional final product from the magnetic powders utilized in Chapter 3. For this reason, magnetic particles are bonded with polymeric matrix. By fabricating composites with magnetic particles, it is aimed to impart magnetism into polymeric materials and in the meantime, create a final product from magnetic nanoparticles. A novel, cost-effective, environmentally friendly process; 3D printing was used for manufacturing the polymer bonded rare-earth free MnAl magnets with arbitrary shape. By 3D printing, magnets can be produced in complex shapes with precisely customized magnetic properties and precisely located magnetic parts, which would be totally inconceivable with other techniques.

4.2. POLYMER BONDED MAGNETIC MATERIALS

Polymer-bonded magnetic materials are conventionally manufactured through the consolidation of magnetic powders with a synthetic resin or a polymeric matrix. According to the application needs, the polymer matrix can be a thermoset, as the

epoxy resin used in compression molded magnets, or a thermoplastic, like nylon used in injection molded magnets, or an elastomer used for extruded magnets.

The most commonly utilized polymer matrix composites are high performance, lightweight materials that are produced by dispersing strong additives/fibers in a polymeric matrix [123]. These additives may vary from graphene to nanotubes, nanowires and nanoparticles. The additive ratio can be as high 60 vol. % depending on the application. However in case of nanocomposites, this proportion can be lowered to almost 2% [124].

Optimal process parameters depend on the particle distribution, size, shape and filler content. Good adhesion between magnetic particles and polymer matrix material is essential for structural integrity and stable magnetic properties of the final composite material.

It is a well-known fact that the magnetic properties of the nanocomposite increase with the filler content. The filler content can also be increased by mixing powders with different particle size and size distribution. The resulting optimized powder mixture will have small particles filling the interparticle spaces of the larger particles [125] which would in turn increase the packing density and improve the magnetic properties.

Particle synthesis parameters as well as composite magnet production methods can also change the characteristics and potential application of bonded magnets. More precisely, synthesis conditions and process parameters of starting alloys determine their microstructure and their magnetic properties and accordingly magnetic properties of polymer-bonded magnets.

Magnetic properties (remanence, coercivity, and maximum energy product) of the polymer-bonded composites is also a function of the magnetic powder content. The use of different amounts of magnetic powders for the production of polymer-bonded composites result in a final magnet with different magnetic properties. The effect of weight (volume) fraction of the powders have been reported in literature for some

magnetic alloys. NdFeB alloy is identified as one of the most suitable magnetic fillers for the polymer bonding technology. Different types of NdFeB compositions proved to have different magnetic outputs reflected in properties of the final composites. Hysteresis curves for bonded NdFeB/epoxy type magnets with different magnetic particle compositions are presented in Figure 4. 1 [125].

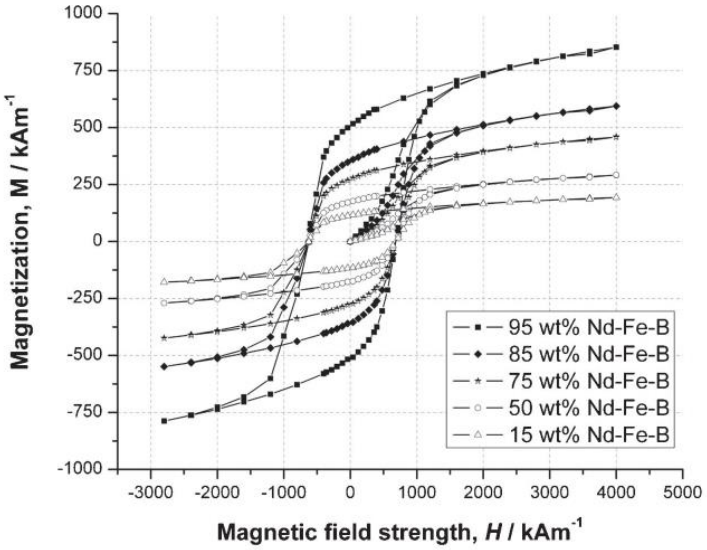

Figure 4. 1 Hysteresis curves for NdFeB bonded magnets with different magnetic powder content showing the increase in Mr and Ms [125].

Hysteresis curves show that the highest energy density correspond to the magnetic composite with the highest amount of magnetic component [126].

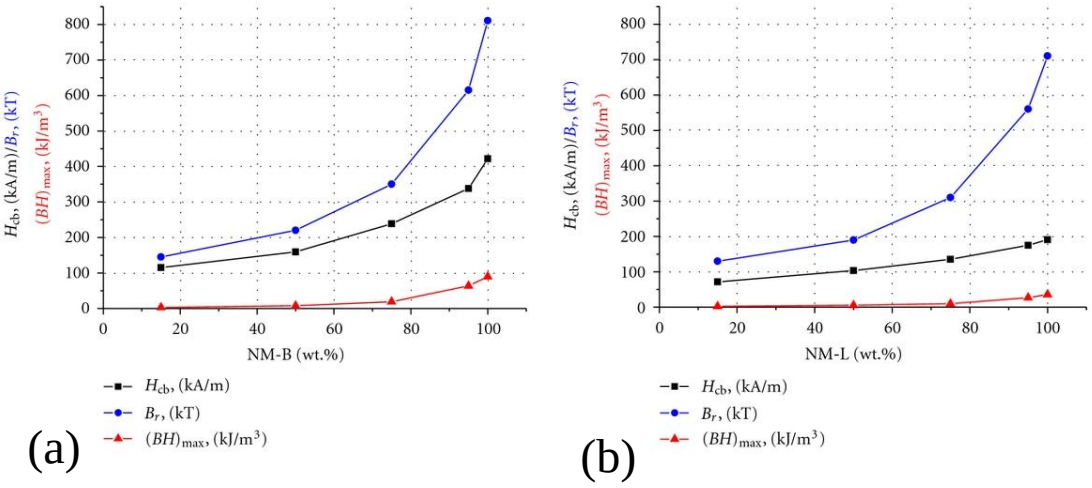

Figure 4. 2 Changes in the magnetic properties with respect to the weight percent of (a) high-Nd and (b) low-Nd content powders in polymer matrix.

Figure 4. 2 shows the increasing trend for three magnetic parameters with increasing amounts of Nd-Fe-B particles in the epoxy matrix. As expected, magnetic properties improve for both low- and high-Nd content composites with increasing Nd-Fe-B content. It is calculated that BH_{max} decreases 1.4, 11.3, and 30 times for composites with Nd particle content of 95, 50, and 15 wt.%, respectively. For composites with low-Nd content, BH_{max} decreases 1.3, 6.4, and 13 times for filler contents of 95, 50, and 15 wt.%, respectively. These results suggest that the nanostructure of the starting NdFeB particles has an impact on magnetic properties of the composites in different manner. The decrease in magnetic properties with a decrease in the magnetic filler content is more pronounced in the composites with high-Nd content. Therefore, for applications requiring high remanence, composites with low-Nd content can be successfully applied. In addition, it should be noted that low-Nd alloy is economically more acceptable due to lower Nd content.

Conventional bonded magnets are fabricated mainly by compression, injection and extrusion molding methods [127] and hence there are design limitations. Currently,

there is no single-unit production technology available for the fabrication of magnets with intricate shapes.

In this study, in order to incorporate magnetic properties, rare-earth free MnAl powders were introduced into a polymeric (polylactide) matrix and the conventional bonded magnet production methods were interchanged with 3D printing technology.

4.3. 3D PRINTING

Traditional manufacturing methods depend on casting, grinding, welding, cutting and extrusion techniques to fabricate components that need to be assembled together. Some of these processes, subtractive ones in particular, result in the loss of the original material; where all of which results in loss of energy during production. 3D printing, an additive manufacturing (AM) technology, layer by layer builds near-net shape components successively using data from 3D CAD models. Each of these printed layers is a thinly-sliced, horizontal cross-section of the final object. Printed product needs no assembly in this method. 3D printing technology does not need any sequential step for the final shaping and thus it is easier to fabricate novel architectures and optimize the final shapes without restrictions imposed by the conventional methods. Fabricating objects with the use of additive manufacturing technology not only utilizes less energy as opposed to subtractive manufacturing technologies; but also minimizes material waste [128][129].

Printing begins with the preparation of a digital file, in which the final shape has been coded and the computer software slices the design into multilayers. These layers are then printed on top of each other using the 3D printer ink, usually a thermoplastic polymers in the case of polymeric 3D printers, until the 3D object is finalized.

As 3D printers has become less expensive and more accessible, a variety of new printing materials have become available. To name a few, polymers, metals, glass, edible food, human tissue can be used as inks in 3D printing. Combination of these raw materials is also possible with the 3D printing technologies.

Early application areas of 3D printers involved printing of small-scale commercial and educational tools and household appliances. Today, 3D printer technology is used in rapid prototyping, industrial and architectural design [130], fashion [131], defense, food industry [132], aerospace and automotive industry [133], biotechnology [134] and tissue engineering [135], [136]. Photos of a few examples of 3D printed prototypes are shown in Figure 4. 3.

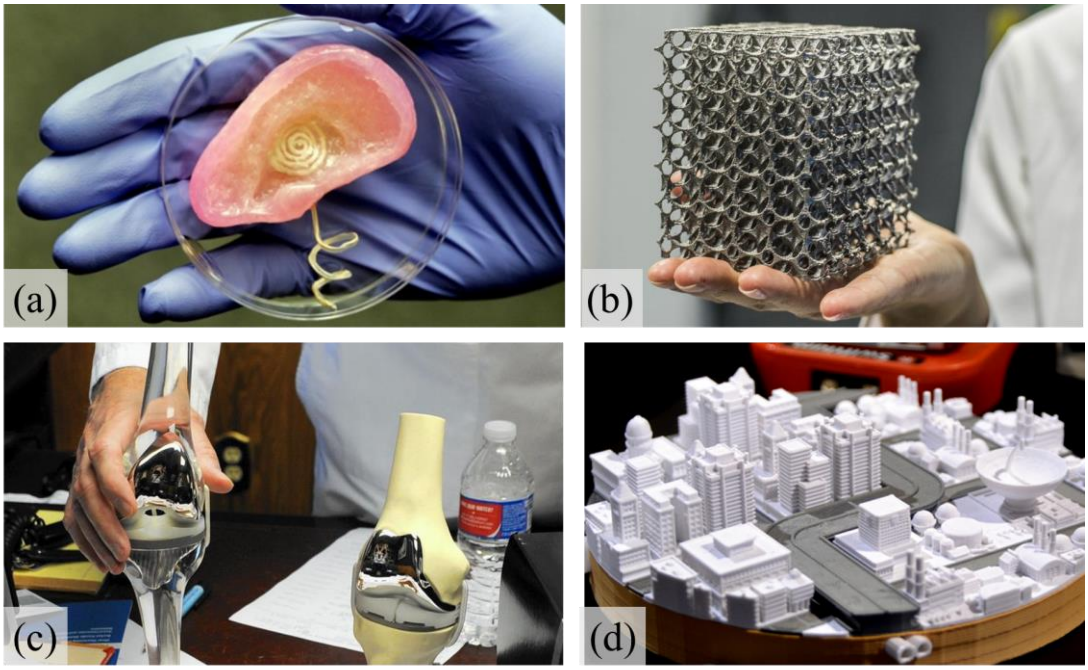

Figure 4. 3 (a) 3D printed bionic ear; first attempt to blend human tissue and electronics [137]; (b) a metal object printed by 3D systems cooperation; (c) a customized 3D printed knee replacement (right) as compared to a traditional knee implant (left) [138]; (d) a 3D printed architectural model [139].

4.3.1 Types of 3D Printing

3-D printing techniques include selective laser sintering (SLS), stereolithography (SL) and fused deposition modeling (FDM) [140], [141]. Selective laser sintering uses laser to selectively fuse the materials into 3D products; whereas stereolithography utilizes an ultraviolet laser to link photopolymer chains. In fused deposition modeling, also

known as fused filament fabrication, polymer filament is heated into a semi-molten state and deposited layer by layer to form the final shape. Mostly, thermoplastic polymers such as polylactide (PLA) and acrylonitrile butadiene styrene (ABS) are preferred as a filament (ink) due to their low melting temperatures relative to metals and ceramics and their ability to return to their solid state after deposition. PLA is preferred over ABS nowadays as it is biodegradable, biocompatible and bioderived [142].

Even though 3D printing has been popular among researchers in the past decade, there is only one work by Huber and co-workers [143] that combines this technology with permanent magnets. In this work, a polymer bonded rare-earth magnet was printed with the Builder 3D printer from Code P. NdFeB powders were utilized as magnetic fillers inside a PA11 polymer matrix. They compared the magnetic properties with injection molded samples and reported that the volumetric mass density of the printed magnet is directly proportional to the remanence of the printed polymer bonded magnet.

By 3D printing a permanent magnet, intricate and complex magnet designs can be created using a computer, printed with millimetric accuracy and directly implemented for use. It is also possible to integrate soft and hard magnetic materials at different parts of a single component and obtain complex designs with tailored magnetic properties.

In this work, synthesized MnAl powders are used to fabricate a composite rare-earth free permanent magnet using 3D printing method.

4.4 EXPERIMENTAL PROCEDURE

$Mn_{72}Al_{28}$ alloys that were fabricated and characterized in Chapter 3, were used as the fillers in this part of the study. At first, arc-melted MnAl ingots were crushed into powders with mortar and pestle and sieved under 200 mesh. Experimental procedure

used for the fabrication of magnetic composites is schematically illustrated in Figure 4. 4.

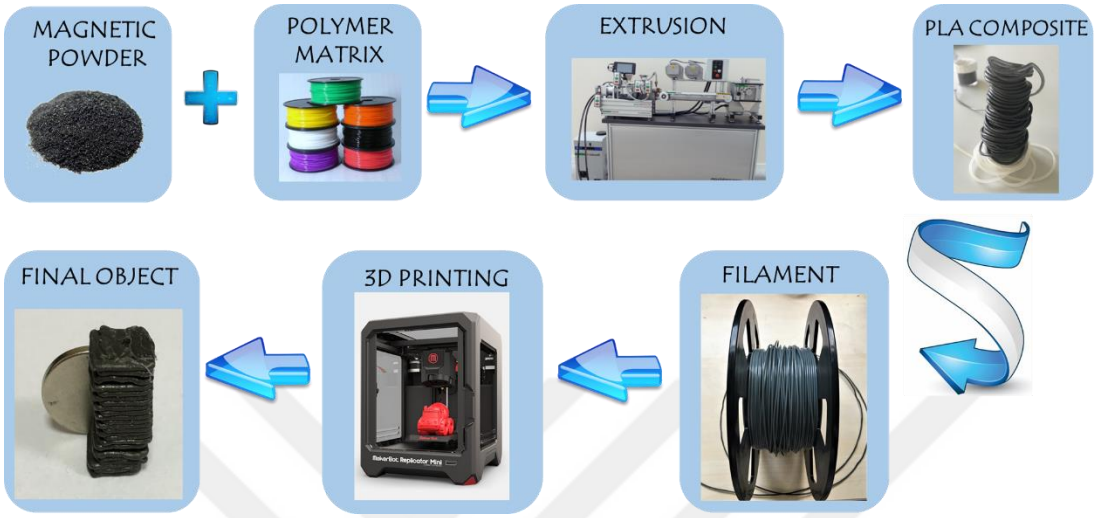

Figure 4. 4 Schematic illustration of the experimental procedure.

In this study, polymer matrix was chosen as PLA, as it is the most common supply material (filament) for 3D printers. In order to obtain a magnetic filament, a commercially available PLA filament (MakerBot) was mixed with MnAl powders. For this purpose, a twin screw extruder (Rondol twin screw extruder) was used. This extruder is designed in 5 zones (as shown in Figure 4. 5) to homogeneously disperse the additives (in this case; MnAl powders) into the polymeric matrix (in this case; PLA). The materials were fed through the feeding zone and followed the zones 1, 2, 3 and 4 respectively. All of the zones have different temperatures to impart sufficient energy to break any aggregates. Temperatures at the feed zone and zone 1, 2, 3 and 4 was set to 150, 195, 200, 195 and 160 °C respectively.

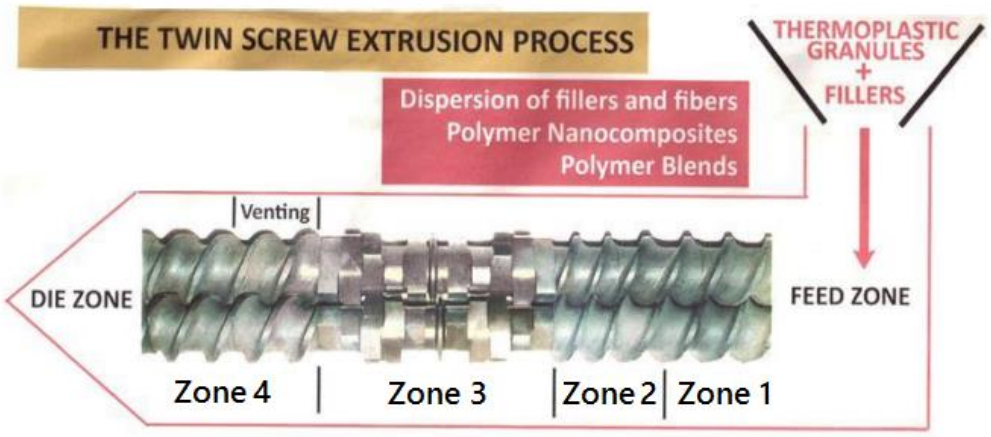

Figure 4. 5 Twin-screw extruder configuration and profile [144].

PLA and magnetic MnAl powders were separately fed into the extruder from the feed zone and the final shape is obtained at the die zone. The opening at the die zone was 1.75 mm. The filament manufactured from the extruder was then fed into the 3D printer. A commercially available fused deposition model printer (Makerbot Replicator Mini) and a custom made 3D printer converted from a Computer Numerically Controlled (CNC) machine were utilized in this part of the study. Photos of both printers used in this work are provided in Figure 4. 6.

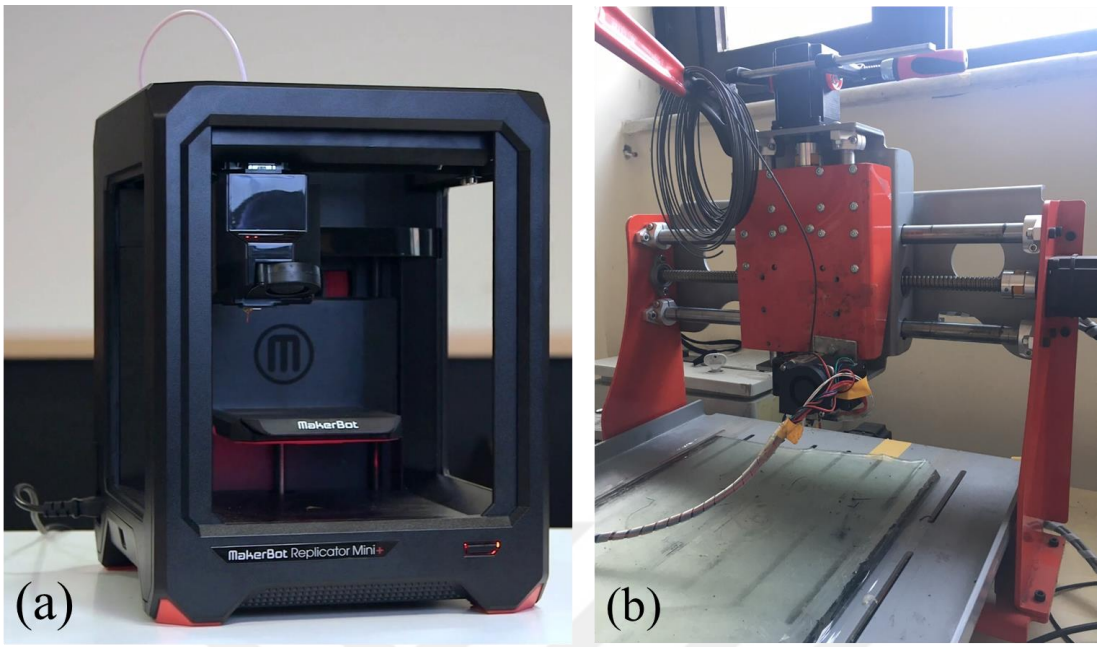

Figure 4. 6 Photos of (a) Makerbot Replicator Mini and (b) custom made 3D printer converted from a CNC machine.

PLA was used as the supply material (filament) in both printers. The extruder pulls and retracts the filament into the printer in precise amounts by the encoder wheel. If the filament is jammed or depleted, filament presence sensor quits printing. Filament was heated to a molten state inside the extruder assembly and forced out from the heated nozzle at a predetermined diameter. The extruded filament was deposited on the building platform layer by layer according to the digital design file. PLA hardens immediately and the final object was created. A photo of the components of the extruder assembly of Makerbot Replicator Mini are provided in Figure 4. 7.

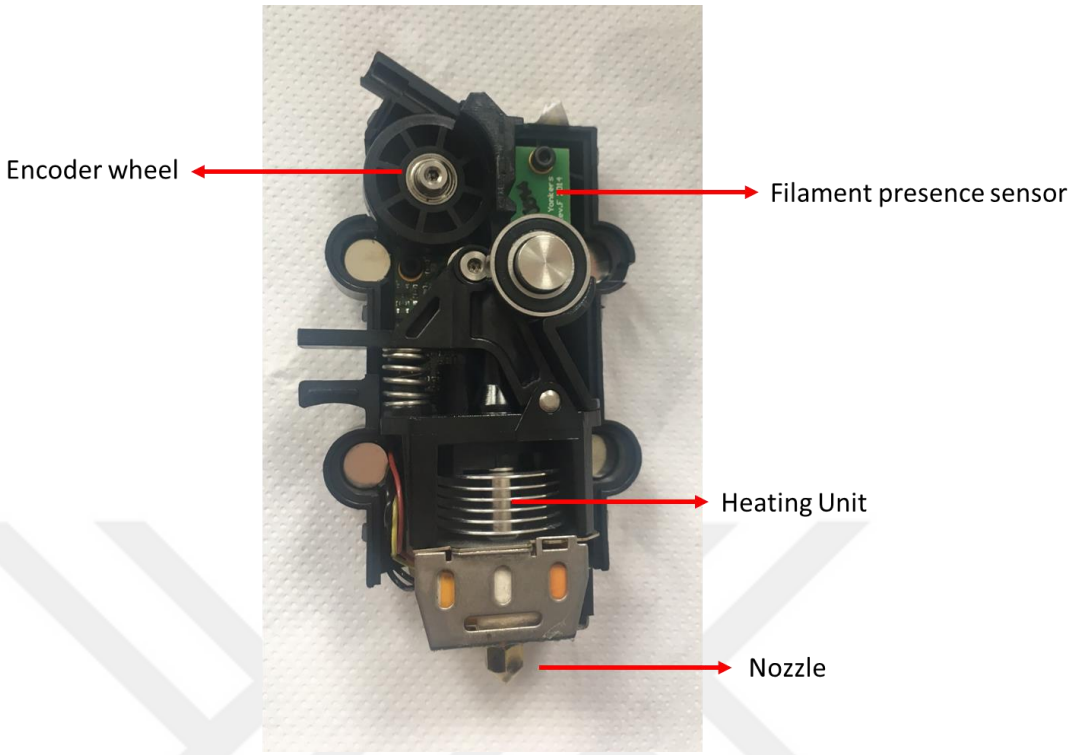

Figure 4. 7 Photo of the extruder assembly showing the components of Makerbot Replicator Mini.

The end product is not yet magnetic, as the particles were not in a magnetized state. At the very end of the process, printed object was exposed to a strong external magnetic field, converting it into a permanent magnet. Lake Shore electromagnet power supply was utilized and the end product was magnetized to 2 Tesla. Lake Shore's model LS-4005 consists of two adjustable coils, a terminal block and a water cooling unit, suited to many applications including susceptibility measurements, Hall effect studies and magnetic resonance demonstrations. As a sensing device, 3D Hall sensor (Magnet-Physik FH51) was used to confirm the magnitude of the applied magnetic field. Magnet-Physik FH51 sensor has a measurement range of 20 mT to 2T, and can measure frequency ranges of DC and AC from 20 Hz to 10kHz. Magnetic measurements were carried out using a vibrating sample magnetometer (VSM) under an applied field of 2 Tesla at room temperature in Department of Physics Engineering Hacettepe University. Detailed information on VSM is provided in Chapter 2.6.4.

4.5 RESULTS AND DISCUSSION

4.5.1 Extrusion of the composite PLA filament

For 3D printing composites with high filling fraction, the fluidity of the material is important. As the filler content increases, the viscosity of the compound decreases, leading to jamming in the nozzle and cavities in the final shape. For this reason, the matrix material should show sufficient fluidity and must contain only small particles.

The effect of the particle quantity inside the filament was investigated for optimization. In the preliminary tests, PLA and MnAl powders were combined and physically agitated in order to observe the physical changes. It is already known from the literature that the minimum amount of powders to make a bonded magnet is around 15 wt. % [125]. PLA was heated to a molten state (215°C) and MnAl powders at 15, 20, 30, 40, 50 wt. % were fed to PLA and mixed manually. It became very difficult to stir the mixture at a loading of 40 wt. % as the plasticity decreased significantly. The hardened filament was also found to be brittle. Brittleness of the mixture would cause problems during printing; thereby, the filler content was kept below 40 wt. % throughout the experiments.

In order to manufacture a long magnetic rod to be fed into printer, PLA and MnAl powders were mixed by extrusion. Even though the opening diameter at the die zone was 1.75 mm, the exact sample diameter was changed with the screw speed. The sample diameter was especially important in the current case as the feed of the 3D printer was determined by the physical dimensions of the feed zone. It was not possible to feed a filament thicker than the original one into the 3D printer and at the same time, it was not feasible to feed a thinner filament as it may cause variations in the layer thickness. It was observed that the sample got thicker with decreasing speed, whereas it got thinner with the increasing speed. The screw speed was manually set to values between 50-60 RPM to obtain a rod shape with a diameter of around 0.8 mm. The rod was left as is after the die zone and the extruded sample was collected on the table in the form of a spiral due to the gravitational forces. Photos of the final filament is shown

in Figure 4. 8. Transparent PLA was transformed into grey through the addition of the magnetic MnAl powders. The color gradient can be seen in the photo provided in Figure 4. 8 (b).

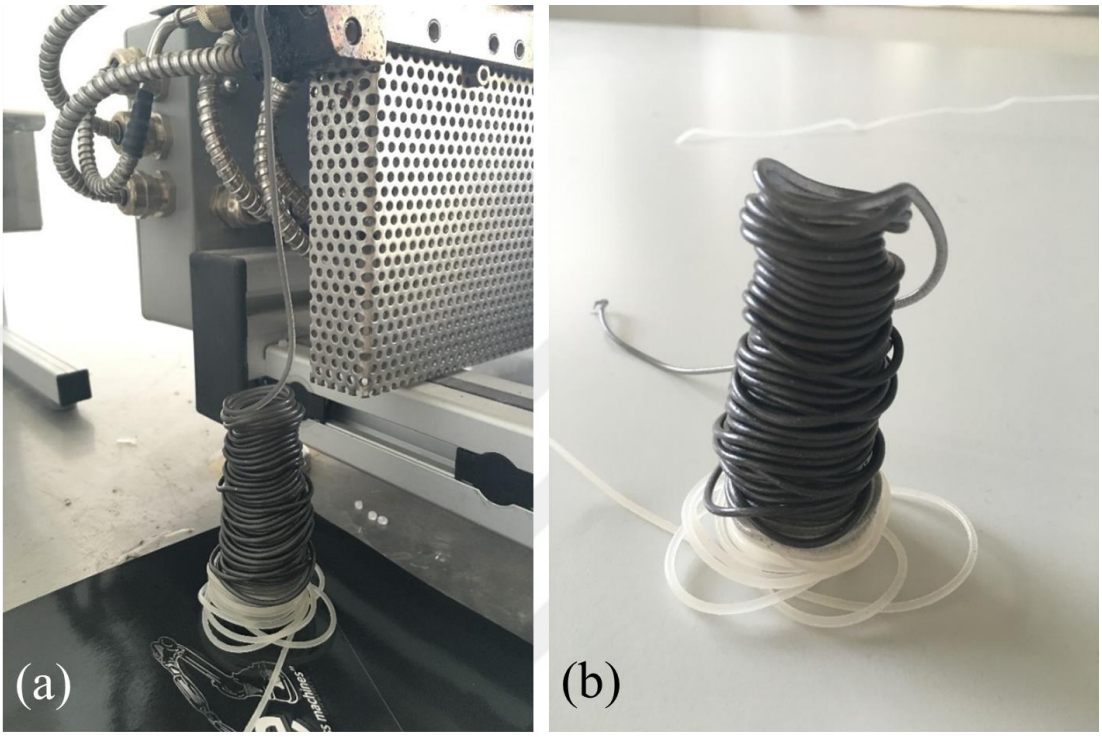

Figure 4. 8 Photos of (a) PLA filament mixed with MnAl powders after extrusion and (b) spiral filament showing the color gradient.

Low and high magnification SEM micrographs of the filament after extrusion are provided in Figure 4. 9 (a) and (b), respectively. Cross-sectional images suggested that MnAl powders are randomly and homogeneously distributed throughout the sample. Powders are not just scattered on the surface but embedded within the matrix and extrusion method proved to be high effective in mixing MnAl powders with PLA matrix. Irregularly shaped particles with faceted corners were observed in the SEM images. Particle sizes of the powders were found to range from 5 to 60 μm. Image J analysis revealed the filler area fraction in this particular cross-section as 10%.

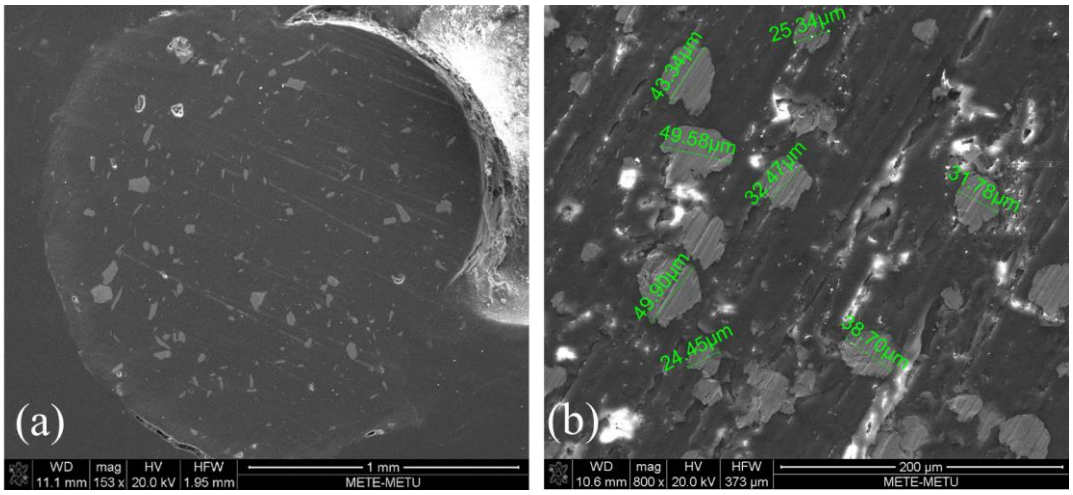

Figure 4. 9 SEM micrographs in (a) low and (b) high resolution showing PLA mixed with magnetic powders.

For comparison, a commercial iron (Fe) based PLA filament was purchased from Proto-Pasta. PLA matrix with encapsulated Fe particles is available on the market and is advertised by its ability to attract magnetic fields and have a rustable, rustic look over time. Figure 4. 10 shows high and low resolution SEM micrographs of the commercially available PLA/Fe filament. It is observed that the particle size distribution was almost the same with respect to the MnAl/PLA filament fabricated in this study. Volume percent of the Fe particles encapsulated in PLA matrix was observed to be higher than MnAl/PLA filament fabricated in this study.

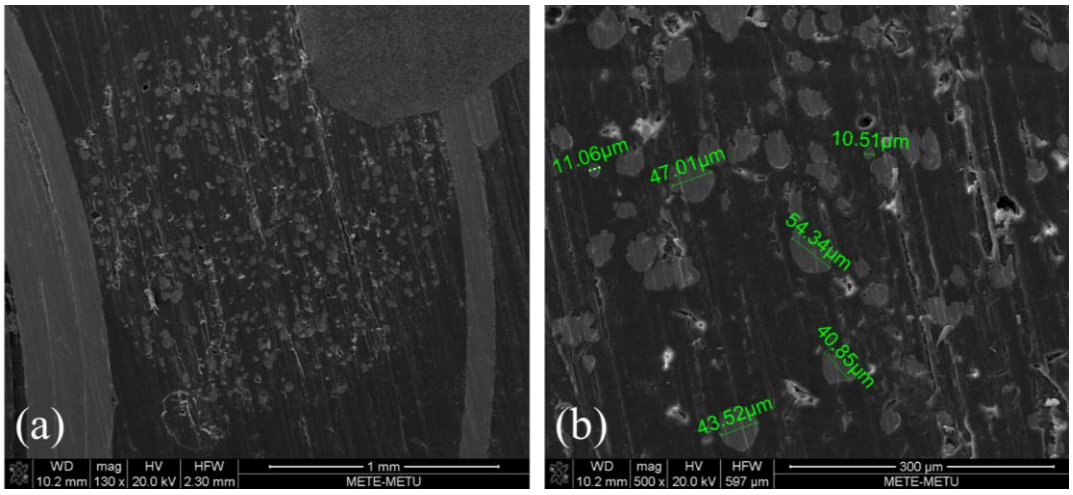

Figure 4. 10 High (a) and low (b) resolution SEM micrographs of the commercially available PLA/Fe filament.

4.5.2 3D Printing of a polymer composite magnet

Following extrusion, in order to feed the composite into the 3D printer, it was necessary to reshape the spiral filament back to its original flat rod form. The sample was heated by a torch to a relatively low temperature at which stretching from both ends reshapes the material without any damage given to the filament coil.

Printing temperature was adjusted according to the thermal behavior of PLA. DSC experiments were carried out on PLA filament in order to define the critical melting temperatures for 3D printing. DSC curve obtained for this sample is given in Figure 4. 11. It is observed that the glass transition temperature was found to be around 70 ºC. The melting temperature of the PLA filament was found as 150 ºC; thereby, extruder temperature was set at a higher temperature.

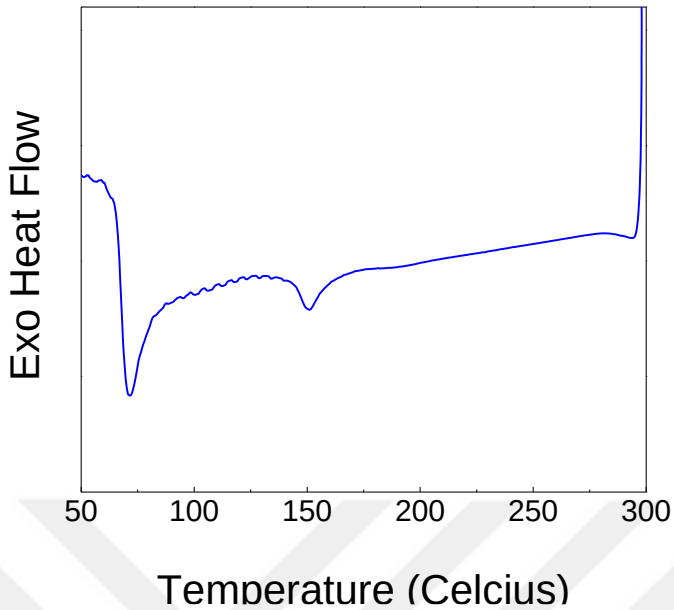

Figure 4. 11 DSC curve of the commercial PLA filament used in 3D printing.

A commercial 3D printer (Makerbot Replicator Mini) and a custom made 3D printer converted from a CNC machine were used in this study. Both printers had the same working principle. At first, filament spool was heated to just above its softening point. Then this semi-molten filament was forced out from a heated nozzle with the aid of an extruder and the object is created layer by layer on the building platform. Individual layers adhere to each other during printing and immediately return its solid state. The extruder moves in X and Y direction, where building platform moves in Z direction.

Several prototypes were printed during the preliminary studies from the 3D printer in order to get accustomed to the working principles of the printer. Photos of some of these prototypes are shown in Figure 4. 12.

Figure 4. 12 Photos of two prototypes printed using the custom made 3D printer.

It was observed that extruder randomly stops pushing the filament through the nozzle in the middle of a printing process causing pauses in printing and irregularities between the layers. A failed layer causes total print failure and thereby, it is especially important to have a smooth run in 3D printing. When the extruder was dismantled, it is observed that the feed was jamming at the very end of the nozzle. Magnetic powders blocked the nozzle mainly due to two reasons. Either the nozzle was excessively heated resulting in a too fast printing speed or the amount of the particles inside the filament was too much to fit into the opening. Temperature and printing speed values were more or less similar in most printers; thereby, the effect of nozzle size was investigated. In order to overcome this problem, the standard nozzle with a tip diameter of 0.4 mm was replaced with a larger nozzle of 1 mm in custom made printer. As Makerbot Replicator Mini is a commercial printer, it was not possible to replace the nozzle. Even if one changes the nozzle setup manually, Makerbot software doesn't allow any changes and doesn't recognize these differences in the setup. Increasing the nozzle diameter proved to be efficient for the custom made printer and printing process was finished without further issues. Printing parameters for both printers utilized in this work are provided in Table 4. 1.

Table 4. 1 Printing parameters for the 3D printers utilized in this work.

Parameter	Makerbot Replicator Mini	Custom made
Extruder temperature	215 °C	215 °C
Filament diameter	1.75 mm	1.75 mm
Nozzle diameter	0.4 mm	1 mm
Printer speed	20 mm/s	20 mm/s
Layer thickness	0.4 mm	1 mm
Layer resolution	100 micron	100 micron
Fill density	0.6 %	10%
Bed temperature	Ambient	Ambient

The printer heats the filament and applies the ink point by point onto the desired locations using a nozzle. The result was a three-dimensional object composed of roughly 80 wt. % PLA and 20 wt. % magnetic powder, calculated through simple mass calculations. It was observed that even though both printers had a similar working principle, there were some differences in terms of print quality. Photos of two blocks printed with different printers are shown in Figure 4. 13. Makerbot printer is an end-user commercial printer thereby, its components are fixed. It only allows a few parameters to be changed. As custom made 3D printer is customized, its components are adjustable and most of the parameters can be easily tuned. Nozzle size was fixed for the Makerbot (0.4 mm) printer and clogging was more common in Makerbot printer. It took more time and effort to create an object as there were many interruptions due to stuck filament pieces in the nozzle. Custom made printer with a larger nozzle (1 mm) has no jamming issues; however, the final object had several issues. The first one was the misalignment in the print layers as shown in Figure 4. 13(b). It was observed that the layers gradually leaned over. A shifted print is usually caused by mechanical issues with the stepper motor or if the tool head is moving too fast. The printer had no feedback system to detect any misalignments, so it would just

keep printing as if nothing has changed. The other problem was the restriction of the layer thickness. The smallest layer thickness one can set for the custom made printer was 1 mm, confined by the nozzle diameter. Decreasing the layer thickness resulted in better resolution as shown in Figure 4. 13(a) but printing time, possibility of having artifacts and errors increases. Print layers were visible in both objects; however, if desired surface can be polished to obtain a glossier finish.

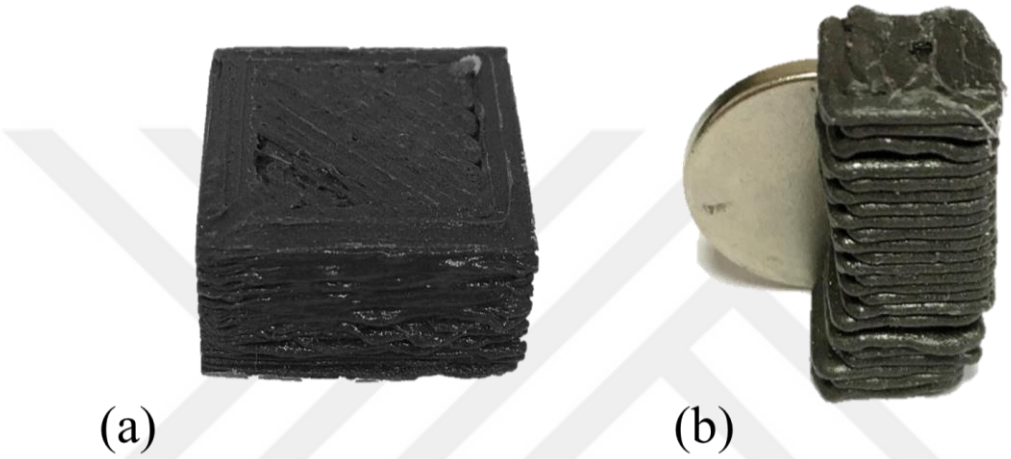

Figure 4. 13 Photo of the 3D printed block from Makerbot Mini, (b) 3D printed block from custom made printer.

Figure 4. 14 shows a 3D printed magnetic propeller used in wheel speed detection both in marine applications and ground vehicles. Other application areas of magnetic polymer composites include thin film coating, packing of electronic circuits, electromagnetic and RF interference (EMI/RFI) shielding for electronic devices [145], [146].

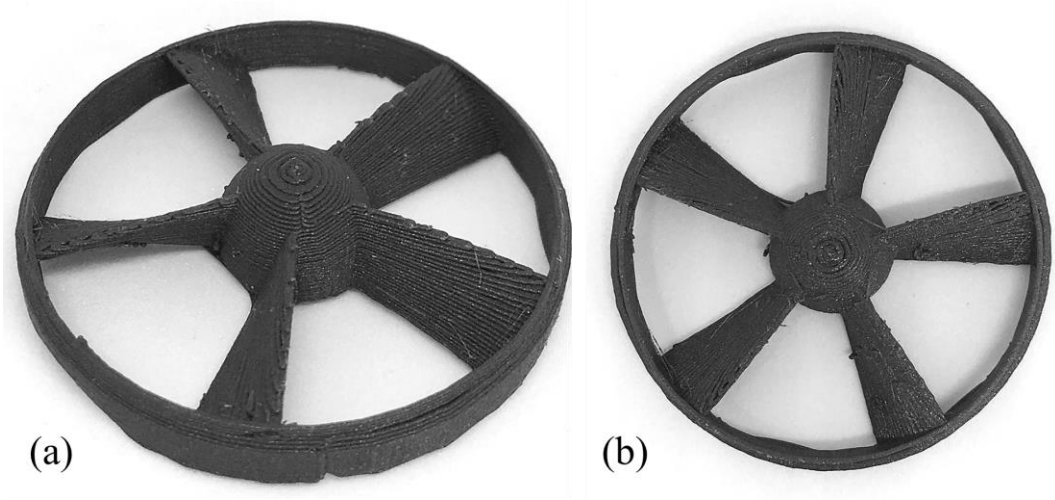

Figure 4. 14 Photo of the 3D printed magnetic propeller used in wheel speed detection both in marine applications and ground vehicles.

The next step was to fully magnetize the object by an external source to the saturation point. For this purpose, an electromagnet power supply was used to apply an external magnetic field of 2 Tesla and a Hall sensor was utilized to confirm the magnitude of the applied magnetic field.

VSM measurements were carried to monitor the magnetic characteristics of the printed composites. Hysteresis curves of the samples are provided in Figure 4. 15. Magnetically induced MnAl powders already had soft magnetic properties and when they are introduced into a PLA matrix, magnetic properties got deteriorated as expected. Polymer bonded material showed paramagnetic behavior. It was observed that the magnets stick to prints made in this study, but the printed objects do not function as magnets by themselves.

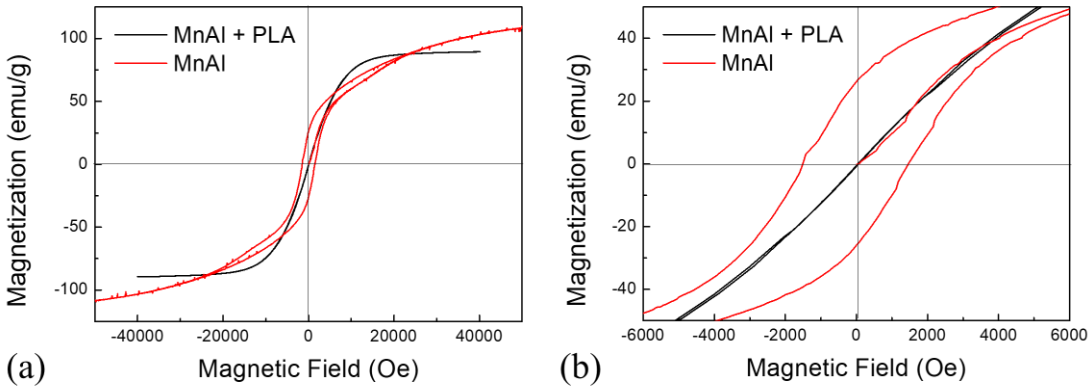

Figure 4. 15 (a) Hysteresis curve of MnAl powders alone and same powders encapsulated in PLA (b) Dependence of energy product on field strength.

4.6 CONCLUSIONS

In this part of the study, 3D printing was presented as a novel manufacturing method for permanent magnets in composite structure. 3D printing is a new tool to precisely tune the function of a product. It has the potential to enhance the available options when designing and printing objects. 3D printing has been the center of attention in the past decade due to being time effective, low-cost and environmental friendly. However, there has been only one publication that combines this technique with NdFeB permanent magnets. In this work, instead of rare-earth magnets, rare-earth free magnet powders synthesized and characterized in Chapter 3 are utilized in 3D printing of composite magnets. A filament of magnetic powders embedded in a polymer binding material was produced through extrusion. MnAl powders were used as the magnetic fillers. A commercial 3D printer and a custom made 3D printer were used for printing. Custom made printer was very easy to adjust and had an easily customizable software. Makerbot printer didn't allow modifications and was strict both in terms of printer design and in software. Melting temperature of PLA was determined as 150°C and printing temperature was adjusted accordingly.

Magnetic properties of bonded magnets were affected by the weight (volume) ratio and magnetic properties of the magnetic filler. Weight ratio was confined by the plasticity and the nozzle diameter. It was observed that the high density of particles

were blocking the nozzle tip and preventing the filament from freely extruding when the nozzle diameter is 0.4 mm. In addition, plasticity decreased significantly and material became brittle. Clogging and brittleness issues were solved only when a nozzle size of 1 mm was used with a filament containing powders 20% by weight.
Even though the weight ratio is determined by the printing parameters, it is known that as the weight ratio of magnetic inside the polymer increases, magnetic properties improve. It is confirmed in this study that the magnetic powders provided soft magnetic properties to the polymer, however; the magnetism was not as strong as a rare-earth polymer bonded magnet.

Overall, it can be stated that it is possible to print a polymer bonded magnet with 3D printing. 3D printing provides design flexibility and enable the manufacturing of complex structures. This study confirms that a magnet with the desired shape could be printed with 3d printers. For the structure and magnetic properties of the final composite material, factors such as nozzle diameter, volume of the feed, particle distribution, and particle size should be taken into consideration.

Concerns of cost and possibility of jamming the nozzle feed limits the magnetic powder content. Thereby, a compromise should be made to obtain the most efficient magnetic material.

CHAPTER 5

CONCLUSION AND FUTURE RECOMMENDATIONS

5.1 CONCLUSIONS

Most of the current permanent magnet industry depends on rare-earth (RE) based magnets. Despite their significantly high magnetic properties, strategical importance of RE elements has induced extensive research towards improvement of RE-free permanent magnets. As important as rare-earth elements are, getting access to those materials are confined by social and political issues. There has been an effort to minimize the use of these elements or eliminate them completely in permanent magnets.

For this reason, two rare-earth free compositions have been studied in this thesis. AlNiCo magnets are the closest successors of rare-earth magnets and their only drawback is the low coercivity. In order to improve the coercivity, AlNiCo powders of different sizes are produced with plasma reaction and ball milling. It is observed that coercivity increases with decreasing particle size. Especially in the case of plasma synthesized powders, the core/shell structure contributed to the enhancement of magnetization due to the effective exchange coupling. A protective oxide layer of Fe_3O_4 on the surface of plasma synthesized AlNiCo nanoparticles was revealed by the STEM EDS data. The magnetically hard core provides high coercivity whereas the magnetically soft shell increases the magnetic flux density. As a combination of this behavior and the coupling between the core and shell, a relatively square hysteresis loop is achieved. The oxide coating not only contributed to an increase in coercivity but also to the protection of the metallic nanoparticles against further oxidation. The interfacial exchange interaction between the magnetically hard core and magnetically soft shell hard and soft magnetic phases may yield finely tailored materials for various

magnetic applications.

The second alloy that has been selected was MnAl-based. The phase transformation hierarchy of the compositions that lead to the formation of metastable ferromagnetic τ-phase was investigated.

Based upon the results obtained from in-situ HEXRD, in situ TEM as well as DSC and magnetic measurements of MnAl-based alloy, it is observed that ε'-phase is a strong prerequisite for the formation of τ-phase. Samples having ε'-phase within the ε-matrix at room temperature found to be magnetic at elevated temperatures. It is observed that ε'-phase transforms into ferromagnetic τ-phase upon annealing. In addition, the composition of MnAl-based alloys affect both the sequence and the temperature of phase transformations. Alloys with Mn content less than 70wt% (S1, S2) had a parent phase mixture consisting of ε and ε' phases at the quenched state. Growth of ε'-phase was followed by a phase transformation into ferromagnetic τ-phase. Prolonged annealing resulted in the decomposition of ε, ε' and τ-phase into stable phases. However, alloys with Mn content higher than 70wt% was found to be paramagnetic. The alloys consist of only ε-phase at the quenched state. Upon annealing, ε-phase directly transformed into equilibrium phases surpassing the τ-MnAl formation. Overall it is suggested that the formation of magnetic τ-MnAl cannot proceed in the absence of ε'-phase.

In Chapters 2 and 3, rare-earth free magnetic powders were fabricated and characterized. However, synthesized magnetic powders cannot be used as a final product and conventional powder processing methods are expensive and labor-intensive. A low cost, commercially available printer and a custom made 3D printer converted from a CNC machine were used. A special filament having MnAl powders embedded in a polymer matrix was produced by extrusion. It is known from the literature that as the magnetic powder content increases, the magnetic properties tend to be stronger. However, the exact value should be optimized considering factors such as degree of plasticity, density and cost. It is observed that if the particle density was

higher than 40%, filament became brittle. Another problem was the jamming of the printer in the middle of the print. The powders accumulated and encoder wheel could not push the filament through the opening. The jamming problem is mostly solved by changing the nozzle diameter. After optimization, magnets having various and intricate shapes can be created for particular applications. Even though there have been couple of issues, 3D printing has the potential to enhance the functionality of a magnetic material.

5.2 FUTURE RECOMMENDATIONS

In Chapter 2, it is observed that magnetic properties of AlNiCo alloys improve with decreasing particle size. Plasma is a novel and indispensable tool to synthesize nanopowders in large scale. Plasma system is mainly used in industry and there are only a limited number of institutions with plasma equipment. Thus, the academic research and development should continue to explore its viability on different alloy systems. There are still some issues (contamination etc.), however, if they are eliminated, the same plasma experiments could be carried out on different compositions. It is known in literature that FeCo phase is the origin of magnetism in AlNiCo alloys. It would worth trying to synthesize bare FeCo nanoparticles with the plasma system. As an alternative, and for comparison, it would also be important to synthesize MnAl nanopowders with this technique to investigate the phase transformation in nanoscale.

In Chapter 3, the main problem was the characterization of ε'-phase and distinguish the ε'-phase from ε-phase. In TEM, diffraction patterns were found to be similar at [110] zone axis, which is confirmed by the QSTEM analysis. It was impossible to tilt the sample to a distinctive zone due to mechanical angle limitations. A different sample at a particular orientation could have been prepared by FIB for further investigations. It is not certain whether ε→ε' ordering takes place or already-present ε' nuclei grow with increasing temperature. Rietveld analysis could be an important tool to observe the quantitative phase changes. It is likely that the amount of τ-phase formed is a

function of the ε'-phase formed during quenching.

Compositional extremities within the τ-phase region should be determined. It is found that one end of the τ forming range corresponds to Mn 70% (by weight). However, the other end is not determined. Same experiments should be carried out with various compositions to find the composition with the least Mn content that can yield τ-phase.

MnAl alloys with Mn content less than 70% showed soft magnetic properties but they might behave as a hard magnetic material in nanosizes. If that is the case, it would be even better to feed these plasma synthesized hard magnetic nanopowders into a polymer and 3D print an object.

The nanopowders synthesized in plasma would have a spherical shape which would better suit 3D printing in terms of filament flow dynamics. In this respect, one can also use the smallest nozzle for printing which would increase the printing resolution. As an alternative, MnAl nanopowders could be synthesized using ball mill which would provide a comparison platform of similar magnetic materials obtained through different processes.

As an alternative to polymer 3D printers, one can try directly printing MnAl nanopowders with a metal 3D printer. Without the polymeric matrix, it is highly probable to obtain a stronger magnetic material.

The increased magnetic filler content is detrimental for the plasticity of the filament though it is known to improve the magnetic properties. In such a case, it might be an option to use a plasticizer during filament production such as PEG (polyethylene glycol).

It is also possible to use fused filament machines with multiple extruder heads. They can be used to print materials with multiple functions. They not only increase the overall print speed, but may also impart various properties to the final print. Magnets with locally varying magnetic properties can be printed with different magnetic powders ranging from soft magnetic alloys to hard magnetic alloys. It is also possible

to use different materials within a single magnet to create a smooth transition between strong and weak magnetism. This would allow tailoring the magnetic properties which cannot be produced with conventional methods.

REFERENCES

[1] D. J. Craik and R. S. Tebble, “Magnetic Domains,” *Reports Prog. Phys.*, vol. 24, no. 1, p. 116, 1961.

[2] W. D. Callister and D. G. Rethwisch, *Materials science and engineering : an introduction*. 2014.

[3] J. M. D. Coey, *Magnetism and Magnetic Materials*. Cambridge University Press, 2009.

[4] F. Bloch, “Zur Theorie des Austauschproblems und der Remanenzerscheinung der Ferromagnetika,” *Zeitschrift f{ü}r Phys.*, vol. 74, no. 5, pp. 295–335, 1932.

[5] R. Skomski and D. J. Sellmyer, “Intrinsic and Extrinsic Properties of Advanced Magnetic Materials,” in *Handbook of Advanced Magnetic Materials*, vol. 37, no. 47, 2006, pp. 1–57.

[6] R. Skomski and D. J. Sellmyer, “Anisotropy of rare-earth magnets,” *J. Rare Earths*, vol. 27, no. 4, pp. 675–679, Aug. 2009.

[7] W. D. Corner, “Permanent magnets,” *Phys. Technol.*, vol. 19, no. 4, pp. 158–165, Jul. 1988.

[8] M.-F. Rossignol and J.-P. Yonnet, “Permanent magnets,” in *Magnetism: Materials and Applications*, É. du Trémolet de Lacheisserie, D. Gignoux, and M. Schlenker, Eds. New York, NY: Springer New York, 2005, pp. 3–88.

[9] K. J. Overshott and B. Polytechnic, “Magnetism : It is Permanent,” vol. 138, no. 1, pp. 1–13, 1991.

[10] D. C. Jiles, “Introduction to magnetism and magnetic materials,” p. 537, 1998.

[11] F. E. Luborsky, “Permanent Magnets in Use Today,” *J. Appl. Phys.*, vol. 37, no. 3, p. 1091, 1966.

[12] M. Sagawa, S. Fujimura, N. Togawa, H. Yamamoto, and Y. Matsuura, “New material for permanent magnets on a base of Nd and Fe (invited),” *J. Appl. Phys.*, vol. 55, no. 6, p. 2083, 1984.

[13] F. Herbst, J. J. Croat, and F. E. Pinkerton, “Relationships between crystal structure and magnetic properties in Nd2Fe14B,” *Phys. Rev. B*, vol. 29, no. 7, pp. 4176–4178, Apr. 1984.

[14] J. J. Croat, F. Herbst, R. W. Lee, and F. E. Pinkerton, “Pr-Fe and Nd-Fe based materials,” *J. Appl. Phys.*, vol. 55, no. 6, pp. 2078–2082, 1984.

[15] M. Sagawa, S. Fujimura, H. Yamamoto, Y. Matsuura, and K. Hiraga, “Permanent magnet materials based on the rare earth-iron-boron tetragonal compounds,” *IEEE Trans. Magn.*, vol. 20, no. 5, pp. 1584–1589, Sep. 1984.

[16] K. H. Müller *et al.*, “New permanent magnets,” *J. Magn. Magn. Mater.*, vol. 226–230, pp. 1370–1376, May 2001.

[17] J. J. Croat, J. F. Herbst, R. W. Lee, and F. E. Pinkerton, “High-energy product Nd-Fe-B permanent magnets ,” *Applied Physics Letters* , vol. 44, no. 1. p. 148, 1984.

[18] J. M. D. Coey, “Permanent magnet applications,” *J. Magn. Magn. Mater.*, vol. 248, no. 3, pp. 441–456, 2002.

[19] R. Skomski, “Nanomagnetics (Topical Rev),” *J. Phys. Condens. Matter*, vol. 15, pp. 841–896, 2003.

[20] M. Rahman and G. Slemon, “Promising applications of Ne-F-B magnets in electrical machines,” *IEEE Trans. Magn.*, vol. 21, no. 5, pp. 1712–1716, Sep. 1985.

[21] S. H. Liou and Y. D. Yao, “Development of high coercivity magnetic force microscopy tips,” *J. Magn. Magn. Mater.*, vol. 190, no. 1, pp. 130–134, 1998.

[22] C.-T. Lin *et al.*, “Facile Preparation of a Platinum Silicide Nanoparticle-Modified Tip Apex for Scanning Kelvin Probe Microscopy,” *Nanoscale Res. Lett.*, vol. 10, p. 401, Oct. 2015.

[23] D. Kingsnorth, “IMCOA - Rare Earths: Reducing our dependence upon China,” in *Metal Pages Rare Earths Conference Beijing*, 2011.

[24] “Metal Pages.” [Online]. Available: http://www.metal-pages.com/metalprices/rareearths/.

[25] J. M. D. Coey, “Permanent magnets: Plugging the gap,” *Scr. Mater.*, vol. 67, no. 6, pp. 524–529, 2012.

[26] T. Mishima, “British Patents,” 1931.

[27] B. D. Cullity and C. D. Graham, *Introduction to Magnetic Materials*. 2009.

[28] Q. Xing *et al.*, “Phase and elemental distributions in alnico magnetic materials,” *IEEE Trans. Magn.*, vol. 49, no. 7, pp. 3314–3317, 2013.

[29] K. J. De Vos, “Microstructure of Alnico alloys,” *J. Appl. Phys.*, vol. 37, no. 3, p. 1100, 1966.

[30] G. Marcon, R. Peffen, and H. Lemaire, “A contribution to the study of AlNiCo 5 thermal treatment in magnetic field,” *IEEE Trans. Magn.*, vol. 14, no. 5, pp. 688–689, 1978.

[31] M. McCaig, *Permanent Magnets in Theory and Practice*. Pentech Press, 1977.

[32] U. Jeong, X. Teng, Y. Wang, H. Yang, and Y. Xia, “Superparamagnetic colloids: Controlled synthesis and niche applications,” *Adv. Mater.*, vol. 19, no. 1, pp. 33–60, 2007.

[33] R. F. Butler and S. K. Banerjee, “Theoretical single-domain grain size range in magnetite and titanomagnetite,” *J. Geophys. Res.*, vol. 80, no. 29, pp. 4049–4058, 1975.

[34] E. F. Kneller and F. E. Luborsky, “Particle size dependence of coercivity and remanence of single-domain particles,” *J. Appl. Phys.*, vol. 34, no. 3, pp. 656–658, 1963.

[35] J. Sung Lee, J. Myung Cha, H. Young Yoon, J.-K. Lee, and Y. Keun Kim, “Magnetic multi-granule nanoclusters: A model system that exhibits universal size effect of magnetic coercivity,” *Sci. Rep.*, vol. 5, no. 1, p. 12135, 2015.

[36] V. Skumryev, S. Stoyanov, Y. Zhang, G. Hadjipanayis, D. Givord, and J. Nogues, “On beating the superparamagnetic limit with exchange bias,” *Nature*, vol. 423, no. 6942, pp. 850–853, 2003.

[37] R. M. Young and E. Pfender, “Generation and behavior of fine particles in thermal plasmas-A review,” *Plasma Chem. Plasma Process.*, vol. 5, no. 1, pp. 1–37, 1985.

[38] F. E. Kruis, H. Fissan, and A. Peled, “Synthesis of nanoparticles in the gas phase for electronic, optical and magnetic applications—a review,” *J. Aerosol Sci.*, vol. 29, no. 5–6, pp. 511–535, 1998.

[39] M. I. Boulos, “The inductively coupled R.F. (radio frequency) plasma,” *High Temp. Mater. Process. An Int. Q. High-Technology Plasma Process.*, vol. 1, no. 1, pp. 17–39, 1997.

[40] M. I. Boulos, “Thermal Plasma Processing,” *IEEE Trans. Plasma Sci.*, vol. 19, no. 6, pp. 1078–1089, 1991.

[41] M. I. Boulos, “Radio frequency plasma developments, scale-up and industrial applications,” *High Temp. Chem. Process.*, vol. 1, pp. 401–411, 1992.

[42] R. Henne, “Thermal Plasmas for Material Processing,” *Contrib. to Plasma Phys.*, vol. 39, no. 5, pp. 385–397, 1999.

[43] S. . Girshick *et al.*, “Thermal plasma synthesis of ultrafine iron particles,” *J. Aerosol Sci.*, vol. 24, no. 3, pp. 367–382, 1993.

[44] M. D. Shinde *et al.*, “Synthesis of uncapped silver nanoparticles using DC arc plasma technique: effect of change in plasma gas on morphological properties,” *Int. J. Nanotechnol.*, vol. 7, no. 9–12, pp. 1110–1119, Jan. 2010.

[45] X. Li, A. Chiba, M. Sato, and S. Takahashi, “Synthesis and characterization of nanoparticles of Alnico alloys,” *Acta Mater.*, vol. 51, no. 18, pp. 5593–5600, 2003.

[46] S. Ohno and M. Uda, “Generation Rate of Ultrafine Metal Particles in ‘Hydrogen Plasma-Metal’ Reaction,” *Nippon Kinzoku Gakkaishi*, vol. 48, pp. 640–646, 1984.

[47] T. Watanabe and M. Tanaka, “Thermal Plasma Processing for Functional Nanoparticle Synthesis,” *16th Asean Reg.*, no. 1, pp. 47–50, 2009.

[48] L. Spanhel, H. Weller, and A. Henglein, “Photochemistry of semiconductor colloids. 22. Electron ejection from illuminated cadmium sulfide into attached titanium and zinc oxide particles,” *J. Am. Chem. Soc.*, vol. 109, no. 22, pp. 6632–6635, Oct. 1987.

[49] A. Henglein, “Small-particle research: physicochemical properties of extremely small colloidal metal and semiconductor particles,” *Chem. Rev.*, vol. 89, no. 8, pp. 1861–1873, Dec. 1989.

[50] G. C. Lavorato *et al.*, “Magnetic Interactions and Energy Barrier Enhancement in Core / Shell Bimagnetic Nanoparticles,” 2015.

[51] E. Lima *et al.*, “Bimagnetic CoO Core/CoFe2O4 Shell Nanoparticles: Synthesis and Magnetic Properties,” *Chem. Mater.*, vol. 24, pp. 512–516, 2012.

[52] X. Sun, N. F. Huls, A. Sigdel, and S. Sun, “Tuning Exchange Bias in Core/Shell FeO/Fe 3 O 4 Nanoparticles,” *Nano Lett.*, vol. 12, pp. 246–251, 2012.

[53] S. . Oldenburg, R. . Averitt, S. . Westcott, and N. . Halas, “Nanoengineering of optical resonances,” *Chem. Phys. Lett.*, vol. 288, no. 2–4, pp. 243–247, 1998.

[54] S. Kalele, S. W. Gosavi, J. Urban, and S. K. Kulkarni, “Nanoshell Particles: Synthesis, Properties and Applications,” *Curr. Sci.*, vol. 91, no. 8, pp. 1038–1052, 2006.

[55] J. Ye *et al.*, “Surface morphology changes on silica-coated gold colloids,” *Colloids Surfaces A Physicochem. Eng. Asp.*, vol. 322, no. 1–3, pp. 225–233, 2008.

[56] L. Wang *et al.*, “Monodispersed core-shell Fe3O4@Au nanoparticles.,” *J. Phys. Chem. B*, vol. 109, no. 46, pp. 21593–21601, Nov. 2005.

[57] F. Bao, J.-F. Li, B. Ren, R.-A. Gu, and Z.-Q. Tian, “Synthesis and Characterization of Au@Co and Au@Ni Core−Shell Nanoparticles and Their Applications in Surface-Enhanced Raman Spectroscopy,” *J. Phys. Chem. C*, vol. 112, no. 2, pp. 345–350, Jan. 2008.

[58] N. Zhang, Y. Gao, H. Zhang, X. Feng, H. Cai, and Y. Liu, “Preparation and characterization of core-shell structure of SiO2@Cu antibacterial agent,” *Colloids Surfaces B Biointerfaces*, vol. 81, no. 2, pp. 537–543, 2010.

[59] H. Zeng, J. Li, J. P. Liu, Z. L. Wang, and S. Sun, “Exchange-coupled nanocomposite magnets by nanoparticle self-assembly.,” *Nature*, vol. 420, no. 6914, pp. 395–398, Nov. 2002.

[60] H. Fan *et al.*, “Self-assembly of ordered, robust, three-dimensional gold

nanocrystal/silica arrays.," *Science*, vol. 304, no. 5670, pp. 567–571, Apr. 2004.

[61] X. F. Zhang *et al.*, "Synthesis, growth mechanism and magnetic properties of SiO2-coated Co nanocapsules," *Acta Mater.*, vol. 55, no. 11, pp. 3727–3733, 2007.

[62] T. Liu, H. Y. Shao, and X. G. Li, "Oxidation behaviour of Fe 3 Al nanoparticles prepared by hydrogen plasma–metal reaction," *Nanotechnology*, vol. 14, no. 5, pp. 542–545, 2003.

[63] F. Caruso, "Nanoengineering of Particle Surfaces," *Adv. Mater.*, vol. 13, no. 1, pp. 11–22, 2001.

[64] S. Mornet *et al.*, "Magnetic nanoparticle design for medical applications," *Prog. Solid State Chem.*, vol. 34, no. 2–4, pp. 237–247, 2006.

[65] Z. Li, L. Wei, M. Y. Gao, and H. Lei, "One-Pot Reaction to Synthesize Biocompatible Magnetite Nanoparticles," *Adv. Mater.*, vol. 17, pp. 1001–1005, 2005.

[66] J. Liu, J. Xu, Z. Liu, X. Liu, and R. Che, "Hierarchical magnetic core-shell nanostructures for microwave absorption: Synthesis, microstructure and property studies," *Sci. China Chem.*, vol. 57, no. 1, pp. 3–12, 2014.

[67] R. Ghosh Chaudhuri and S. Paria, "Core/Shell Nanoparticles: Classes, Properties, Synthesis Mechanisms, Characterization, and Applications," *Chem. Rev.*, vol. 112, no. 4, pp. 2373–2433, Apr. 2012.

[68] H. Zeng, S. Sun, J. Li, Z. L. Wang, and J. P. Liu, "Tailoring magnetic properties of core/shell nanoparticles," *Appl. Phys. Lett.*, vol. 85, no. 5, pp. 792–794, 2004.

[69] L. Zhang and A. Manthiram, "Chemical synthesis, microstructure, and magnetic properties of chains composed of ultrafine Fe–Co–B particles," *Appl. Phys. Lett.*, vol. 80, 1996.

[70] B. Aktekin, “Induction Plasma Synthesis of Mg-Ni Nanoparticles,” 2013.

[71] D. B. Williams and C. B. Carter, *Transmission Electron Microscopy*, vol. 13, no. 3. Springer New York, 1996.

[72] K. J. De Vos, “The relationship between microstructure and magnetic properties of AlNiCo alloys,” 1966.

[73] E. A. Périgo, S. Nakahara, Y. Pittini-Yamada, Y. De Hazan, and T. Graule, “Magnetic properties of soft magnetic composites prepared with crystalline and amorphous powders,” *J. Magn. Magn. Mater.*, vol. 323, no. 15, pp. 1938–1944, 2011.

[74] S. Arajs, N. Amin, and E. E. Anderson, “Magnetic coercivity of Fe3O4 particle systems,” *J. Appl. Phys.*, vol. 69, no. 8, pp. 5122–5123, 1991.

[75] I. Kong, S. H. Ahmad, M. H. Abdullah, and A. N. Yusoff, “The Effect Of Temperature On Magnetic Behavior Of Magnetite Nanoparticles And Its Nanocomposites,” *NANO-Sci-Tech*, pp. 830–834, 2008.

[76] T. Suetsuna, S. Suenaga, T. Takahashi, and K. Harada, “Synthesis of self-forming core/shell nanoparticles of magnetic metal/nonmagnetic oxide,” *Acta Mater.*, vol. 78, pp. 320–327, 2014.

[77] T. Ohtani *et al.*, “Magnetic properties of Mn-Al-C permanent magnet alloys,” *IEEE Trans. Magn.*, vol. 13, no. 5, pp. 1328–1330, 1977.

[78] Q. Zeng, I. Baker, J. B. Cui, and Z. C. Yan, “Structural and magnetic properties of nanostructured Mn–Al–C magnetic materials,” *J. Magn. Magn. Mater.*, vol. 308, no. 2, pp. 214–226, Jan. 2007.

[79] A. Chaturvedi, R. Yaqub, and I. Baker, “Microstructure and Magnetic Properties of Bulk Nanocrystalline MnAl,” *Metals (Basel).*, vol. 4, no. 1, pp. 20–27, 2014.

[80] H. Köno, “On the Ferromagnetic phase in MnAl System,” *J. Phys. Soc. Japan*, vol. 13, no. 12, pp. 1444–1451, 1958.

[81] C. Müller, H. Stadelmaier, B. Reinsch, and G. Petzow, “Metallurgy of the magnetic τ-phase in Mn-Al and Mn-Al-C,” *Zeitschrift für Met.*, vol. 87, no. 7, pp. 594, 1996.

[82] R. Skomski, “Phase formation in L10 magnets,” *J. Appl. Phys.*, vol. 101, no. 9, pp. 1–4, 2007.

[83] D. E. Laughlin, K. Srinivasan, M. Tanase, and L. Wang, “Crystallographic aspects of L10 magnetic materials,” *Scripta Materialia*, vol. 53, no. 4, pp. 383–388, 2005.

[84] C. Yanar, J. M. K. Wiezorek, V. Radmilovic, and W. A. Soffa, “Massive transformation and the formation of the ferromagnetic L10 phase in manganese-aluminum-based alloys,” *Metall. Mater. Trans. A*, vol. 33A, no. 8, pp. 2002–2413, 2002.

[85] N. Singh, V. Mudgil, K. Anand, A. K. Srivastava, R. K. Kotnala, and A. Dhar, “Influence of processing on structure property correlations in τ-MnAl rare-earth free permanent magnet material,” *J. Alloys Compd.*, vol. 633, pp. 401–407, 2015.

[86] T. E. Prost, “Magnetic Properties Study of the Mn-Al System with Additions of B or C and Mechanical Milling Techniques,” 2012.

[87] T. B. Massalski, *Binary Alloy Phase Diagrams*, vol. 2. 1990.

[88] E. Fazakas, L. K. Varga, and F. Mazaleyrat, “Preparation of nanocrystalline Mn-Al-C magnets by melt spinning and subsequent heat treatments,” *J. Alloys Compd.*, vol. 434–435, no. SPEC. ISS., pp. 611–613, 2007.

[89] Z. W. Liu, C. Chen, Z. G. Zheng, B. H. Tan, and R. V Ramanujan, “Phase transitions and hard magnetic properties for rapidly solidified MnAl alloys doped with C, B, and rare earth elements,” *J. Mater. Sci.*, vol. 47, no. 5, pp. 2333–2338, 2012.

[90] J. Z. Wei *et al.*, “tau-MnAl with high coercivity and saturation magnetization,” *AIP Adv.*, vol. 4, no. 127113, pp. 1–11, 2014.

[91] Y. J. Kim and J. H. Perepezko, “Formation of a metastable ferromagnetic ?? phase during containerless melt processing and rapid quenching in Mn-Al-C alloys,” *J. Appl. Phys.*, vol. 71, no. 2, pp. 676–680, 1992.

[92] A. Yamaguchi, Y. Tanaka, K. Yanagimoto, I. Sakaguchi, and N. Kato, “Development of P/M Mn-Al-C Alloy Permanent Magnet,” *Bull. Jpn. Inst. Met.*, p. 28:422, 1989.

[93] J. Y. Law *et al.*, “Study of phases evolution in high-coercive MnAl powders obtained through short milling time of gas-atomized particles,” *J. Alloys Compd.*, vol. 712, pp. 373–378, 2017.

[94] T. Saito, “Magnetic properties of Mn–Al system alloys produced by mechanical alloying,” *J. Appl. Phys.*, vol. 93, no. 8686, 2003.

[95] T. Saito, “Magnetic properties of Mn–Al–C alloy powders produced by mechanical grinding,” *J. Appl. Phys.*, vol. 97, no. 10F304, 2005.

[96] Q. Zeng, I. Baker, and Z. C. Yan, “Nanostructured Mn-Al permanent magnets produced by mechanical milling,” *J. Appl. Phys.*, vol. 99, no. 8, p. 08E902, 2006.

[97] B. Foreback and I. Baker, “Permanent Magnets from Mechanically Milled Mn54Al46 Alloys,” 2008.

[98] W. Lu *et al.*, “Low-energy mechanically milled τ-phase MnAl alloys with high

coercivity and magnetization," *J. Alloys Compd.*, vol. 675, pp. 163–167, 2016.

[99] F. Jiménez-Villacorta, J. Marion, J. Oldham, M. Daniil, M. Willard, and L. Lewis, "Magnetism-Structure Correlations during the ε→τ Transformation in Rapidly-Solidified MnAl Nanostructured Alloys," *Metals (Basel).*, vol. 4, no. 1, pp. 8–19, 2014.

[100] Y. Sakka, M. Nakamura, and K. Hoshimoto, "Rapid quenching and properties of hard magnetic materials in MnAl-X (X = Ti, Cu, Ni, C, B) systems," *J. Mater. Sci.*, vol. 24, pp. 4331–4338, 1989.

[101] J. Van Landuyt, G. Van Tendeloo, J. J. Van Den Broek, and H. Donkersloot, "Permanent magnetism and microstructure in τ-AlMn(C)," *J. Magn. Magn. Mater.*, vol. 15–18, no. PART 3, pp. 1451–1452, 1980.

[102] S. Kojima *et al.*, "Crystal transformation and orientation of Mn-Al-C hard magnetic alloy," *AIP Conf. Proc.*, vol. 24, no. 1975, pp. 768–769, 1975.

[103] J. J. Van Den Broek, H. Donkersloot, G. Van Tendeloo, and J. Van Landuyt, "Phase transformations in pure and carbon-doped Al45Mn55 alloys," *Acta Metall.*, vol. 27, pp. 1497–1504, 1979.

[104] Y. J. Kim and J. H. Perepezko, "The thermodynamics and competitive kinetics of metastable tau phase development in MnAl-base alloys," *Mater. Sci. Eng. A*, vol. A163, no. 1, pp. 127–134, 1993.

[105] D. C. Crew, P. G. McCormick, and R. Street, "MnAl and MnAlC permanent magnets produced by mechanical alloying," *Scr. Metall. Mater.*, vol. 32, no. 3, pp. 315–318, 1995.

[106] I. Janotova *et al.*, "Phase analysis and structure of rapidly quenched Al-Mn systems," *J. Alloys Compd.*, vol. 707, pp. 137–141, 2017.

[107] P. Muellner, B. E. Buergler, H. Heinrich, A. S. Sologubenko, and G. Kostorz,

"Observation of the shear mode of the ε→τ phase transformation in a Mn-Al-C single crystal," *Philos. Mag. Lett.*, vol. 82, no. 2, pp. 71–79, 2002.

[108] W. H. Dreizler and A. Menth, "Transformation kinetics of the ferromagnetic alloy Mn-Al-C," *IEEE Trans. Magn.*, vol. 15, no. 6, p. 1775, 1979.

[109] A. S. Sologubenko, P. Müllner, H. Heinrich, M. Woligarten, and G. Kostorz, "The effect of composition and stress on the selection of epsilon to tau transformation modes in MnAI-C," *J. Phys. IV Fr.*, vol. 112, pp. 1071–1074, 2003.

[110] P. Müllner, B. E. Bürgler, H. Heinrich, A. S. Sologubenko, and G. Kostorz, "Observation of the shear mode of the ε → τ phase transformation in a Mn-Al-C single crystal," *Philos. Mag. Lett.* , 2010.

[111] J. M. K. Wiezorek, A. K. Kulovits, C. Yanar, and W. A. Soffa, "Grain boundary mediated displacive-diffusional formation of τ-phase MnAl," *Metall. Mater. Trans. A Phys. Metall. Mater. Sci.*, vol. 42A, pp. 594–604, 2011.

[112] A. S. Sologubenko, P. Müllner, H. Heinrich, and G. Kostorz, "On the plate-like τ-phase formation in MnAl–C alloys," *Zeitschrift für Met.*, vol. 95, no. 6, pp. 486–491, 2004.

[113] D. P. Hoydick, E. J. Palmiere, and W. A. Soffa, "Microstructural development in MnAl-base permanent magnet materials: New perspectives," *J. Appl. Phys.*, vol. 81, no. 8, pp. 5624–5626, 1997.

[114] D. P. Hoydick, E. J. Palmiere, and W. A. Soffa, "On the formation of the Metastable L1o phase in Manganese-Aluminum-Base Permanent Magnet Materials," *Scr. Mater.*, vol. 36, no. 2, pp. 151–156, 1997.

[115] C. Yanar, V. Radmilovic, W. A. Soffa, and J. M. K. Wiezorek, "Evolution of

microstructure and defect structure in L10-ordered manganese aluminide permanent magnet alloys," *Intermetallics*, vol. 9, no. 10–11, pp. 949–954, 2001.

[116] A. S. Sologubenko, P. Müllner, H. Heinrich, M. Woligarten, and G. Kostorz, "On the plate-like tau phase formation in MnAl-C alloys," *Met. / Organ der Dtsch. Gesellschaft für Met.*, vol. 95, no. 6, pp. 486–491, 2004.

[117] H. E. Kissinger, "Reaction Kinetics in Differential Thermal Analysis," *Anal. Chem.*, vol. 29, no. 11, pp. 1702–1706, 1957.

[118] T. Ozawa, "A New Method of Analyzing Thermogravimetric Data," *Bull. Chem. Soc. Jpn.*, vol. 38, no. 11, pp. 1881–1886, 1965.

[119] S. A. Arrhenius, "Über die Dissociationswärme und den Einfluß der Temperatur auf den Dissociationsgrad der Elektrolyte," *Zeitschrift für Phys. Chemie*, vol. 4, p. 96–116., 1889.

[120] C. Koch, "Determination of core structure periodicity and point defect," 2002.

[121] V. M. Gundyrev, M. A. Uimin, A. E. Ermakov, and O. B. Andreeva, "Transformation in MnAl-C Alloys," *Phys. status solidi*, vol. 91, no. 1, pp. K55–K58, 1985.

[122] J. J. V. D. B. Broek and H. Donkersloot, "Phase Transformations in Pure and Carbon-Doped Al45Mn55 Alloys," *Acta Metall.*, vol. 27, pp. 1497–1504, 1979.

[123] T. Keller, "Recent all-composite and hybrid fibre-reinforced polymer bridges and buildings," *Prog. Struct. Eng. Mater.*, vol. 3, no. 2, pp. 132–140, 2001.

[124] T. Ramanathan *et al.*, "Functionalized graphene sheets for polymer nanocomposites," *Nat. Nanotechnol.*, vol. 3, no. 6, pp. 327–331, Jun. 2008.

[125] A. Grujić, J. Stajić-Trošić, M. Stijepović, and J. Stevanović, "Market and

applications of bonded magnets," *Econ. Manag. Inf. Technol.*, vol. 1, no. 2, pp. 151–158, 2012.

[126] A. Grujić, J. Stajić-trošić, and M. Stijepović, "Magnetic and Dynamic Mechanical Properties of Nd-Fe-B Composite Materials with Polymer Matrix," *Met. Ceram. Polym. Compos. Var. Uses*, p. 684, 2011.

[127] M. Hamano, "Overview and outlook of bonded magnets in Japan," *J. Alloys Compd.*, vol. 222, no. 1–2, pp. 8–12, 1995.

[128] C. Balletti, M. Ballarin, and F. Guerra, "3D printing: State of the art and future perspectives," *J. Cult. Herit.*, vol. 26, pp. 172–182, 2017.

[129] I. Gibson, D. W. D. W. Rosen, and B. Stucker, *Additive Manufacturing Technologies: Rapid Prototyping to Direct Digital Manufacturing*, vol. 54. 2009.

[130] J.-Y. Lee, J. An, and C. K. Chua, "Fundamentals and applications of 3D printing for novel materials," *Appl. Mater. Today*, vol. 7, pp. 120–133, 2017.

[131] J. Tarmy, "The Future of Fashion Is 3D Printing Clothes at Home." [Online]. Available: https://www.bloomberg.com/news/articles/2016-04-15/3d-printing-is-poised-to-bring-haute-couture-into-the-home.

[132] Z. Liu, M. Zhang, B. Bhandari, and Y. Wang, "3D printing: Printing precision and application in food sector," *Trends Food Sci. Technol.*, 2017.

[133] J. Stanfield, "NASA Tests First 3-D Printed Rocket Engine Part Made with Two Different Alloys." [Online]. Available: https://www.nasa.gov/topics/technology/manufacturing-materials-3d/index.html.

[134] B. C. Gross, J. L. Erkal, S. Y. Lockwood, C. Chen, and D. M. Spence, "Evaluation of 3D printing and its potential impact on biotechnology and the

chemical sciences," *Anal. Chem.*, vol. 86, no. 7, pp. 3240–3253, 2014.

[135] H.-W. Kang, S. J. Lee, I. K. Ko, C. Kengla, J. J. Yoo, and A. Atala, "A 3D bioprinting system to produce human-scale tissue constructs with structural integrity," *Nat. Biotechnol.*, vol. 34, no. 3, pp. 312–319, 2016.

[136] S. V Murphy and A. Atala, "3D bioprinting of tissues and organs," *Nat. Biotechnol.*, vol. 32, pp. 773–785, 2014.

[137] M. S. Mannoor *et al.*, "3D printed bionic ears," *Nano Lett.*, vol. 13, no. 6, pp. 2634–2639, 2013.

[138] J. O'Hearn, "Harford surgeon uses 3D technology for knee replacement." [Online]. Available: http://www.baltimoresun.com/news/maryland/harford/belair/ph-ag-3d-knee-0923-20150925-story.html.

[139] "Architecture: Build detailed, durable models with 3D printing." [Online]. Available: http://www.stratasys.com/industries/architecture.

[140] C. K. Chua and K. F. Leong, *3D Printing and Additive Manufacturing: Principles and Applications*, Fifth Edit. World Scientific Publishing Co. Pte. Ltd., 2017.

[141] S. Ahn, M. Montero, D. Odell, S. Roundy, and P. K. Wright, "Anisotropic material properties of fused deposition modeling ABS," *Rapid Prototyp. J.*, vol. 8, no. 4, pp. 248–257, 2002.

[142] Ramon, "PLA vs. ABS Plastic – The Pros and Cons," *3D Insider*. [Online]. Available: http://3dinsider.com/pla-vs-abs-plastic-pros-cons/.

[143] C. Huber *et al.*, "3D print of polymer bonded rare-earth magnets, and 3D magnetic field scanning with an end-user 3D printer," *Appl. Phys. Lett.*, vol. 109, no. 16, pp. 1–5, 2016.

[144] H. El-Dessouky and C. Lawrence, *Nanoparticles dispersion in processing functionalised PP/TiO2 nanocomposites: Distribution and properties*, vol. 13. 2011.

[145] D. D. . Chung, “Materials for Electromagnetic Interference Shielding,” *J. Mater. Eng. Perform.*, vol. 9, no. 3, pp. 418–424, 2000.

[146] C. Stancu, P. V Notingher, V. Ionita, V. Marinescu, and D. Panaitescu, “Structure and Properties of Polyethylene-Based Magnetic Composites,” *Ann. Univ. Craiova, Electr. Eng. Ser.*, no. 38, 2014.

APPENDIX A: PERMISSION LICENCES

ELSEVIER LICENSE
TERMS AND CONDITIONS

Aug 27, 2017

This Agreement between Mrs. Ayse Genc ("You") and Elsevier ("Elsevier") consists of your license details and the terms and conditions provided by Elsevier and Copyright Clearance Center.

License Number	4177061419787
License date	Aug 27, 2017
Licensed Content Publisher	Elsevier
Licensed Content Publication	Journal of Magnetism and Magnetic Materials
Licensed Content Title	Synthesis of AlNiCo core/shell nanopowders
Licensed Content Author	A.M. Genc, M.V. Akdeniz, T. Ozturk, Y.E. Kalay
Licensed Content Date	Nov 1, 2016
Licensed Content Volume	417
Licensed Content Issue	n/a
Licensed Content Pages	5
Start Page	112
End Page	116
Type of Use	reuse in a thesis/dissertation
Portion	full article
Format	both print and electronic
Are you the author of this Elsevier article?	Yes
Will you be translating?	No
Title of your thesis/dissertation	Development of Rare Earth Free Permanent Magnets
Expected completion date	Oct 2017
Estimated size (number of pages)	120

Requestor Location Mrs. Ayse Genc
Middle East Technical University
Metallurgical and Materials Engineering D209
ANKARA, 06800 Turkey
Attn: Mrs. Ayse Genc

Total 0.00 USD

Terms and Conditions

INTRODUCTION

1. The publisher for this copyrighted material is Elsevier. By clicking "accept" in connection with completing this licensing transaction, you agree that the following terms and conditions apply to this transaction (along with the Billing and Payment terms and conditions established by Copyright Clearance Center, Inc. ("CCC"), at the time that you opened your Rightslink account and that are available at any time at http://myaccount.copyright.com).

GENERAL TERMS

2. Elsevier hereby grants you permission to reproduce the aforementioned material subject to the terms and conditions indicated.

3. Acknowledgement: If any part of the material to be used (for example, figures) has appeared in our publication with credit or acknowledgement to another source, permission must also be sought from that source. If such permission is not obtained then that material may not be included in your publication/copies. Suitable acknowledgement to the source must be made, either as a footnote or in a reference list at the end of your publication, as follows:

"Reprinted from Publication title, Vol /edition number, Author(s), Title of article / title of chapter, Pages No., Copyright (Year), with permission from Elsevier [OR APPLICABLE SOCIETY COPYRIGHT OWNER]." Also Lancet special credit - "Reprinted from The Lancet, Vol. number, Author(s), Title of article, Pages No., Copyright (Year), with permission from Elsevier."

4. Reproduction of this material is confined to the purpose and/or media for which permission is hereby given.
5. Altering/Modifying Material: Not Permitted. However figures and illustrations may be altered/adapted minimally to serve your work. Any other abbreviations, additions, deletions and/or any other alterations shall be made only with prior written authorization of Elsevier Ltd. (Please contact Elsevier at permissions@elsevier.com). No modifications can be made to any Lancet figures/tables and they must be reproduced in full.
6. If the permission fee for the requested use of our material is waived in this instance, please be advised that your future requests for Elsevier materials may attract a fee.
7. Reservation of Rights: Publisher reserves all rights not specifically granted in the combination of (i) the license details provided by you and accepted in the course of this licensing transaction, (ii) these terms and conditions and (iii) CCC's Billing and Payment terms and conditions.
8. License Contingent Upon Payment: While you may exercise the rights licensed immediately upon issuance of the license at the end of the licensing process for the transaction, provided that you have disclosed complete and accurate details of your proposed use, no license is finally effective unless and until full payment is received from you (either by publisher or by CCC) as provided in CCC's Billing and Payment terms and conditions. If full payment is not received on a timely basis, then any license preliminarily granted shall be deemed automatically revoked and shall be void as if never granted. Further, in the event that you breach any of these terms and conditions or any of CCC's Billing and Payment terms and conditions, the license is automatically revoked and shall be void as if never granted. Use of materials as described in a revoked license, as well as any use of the materials beyond the scope of an unrevoked license, may constitute copyright infringement and publisher reserves the right to take any and all action to protect its copyright in the materials.
9. Warranties: Publisher makes no representations or warranties with respect to the licensed material.

10. Indemnity: You hereby indemnify and agree to hold harmless publisher and CCC, and their respective officers, directors, employees and agents, from and against any and all claims arising out of your use of the licensed material other than as specifically authorized pursuant to this license.

11. No Transfer of License: This license is personal to you and may not be sublicensed, assigned, or transferred by you to any other person without publisher's written permission.

12. No Amendment Except in Writing: This license may not be amended except in a writing signed by both parties (or, in the case of publisher, by CCC on publisher's behalf).

13. Objection to Contrary Terms: Publisher hereby objects to any terms contained in any purchase order, acknowledgment, check endorsement or other writing prepared by you, which terms are inconsistent with these terms and conditions or CCC's Billing and Payment terms and conditions. These terms and conditions, together with CCC's Billing and Payment terms and conditions (which are incorporated herein), comprise the entire agreement between you and publisher (and CCC) concerning this licensing transaction. In the event of any conflict between your obligations established by these terms and conditions and those established by CCC's Billing and Payment terms and conditions, these terms and conditions shall control.

14. Revocation: Elsevier or Copyright Clearance Center may deny the permissions described in this License at their sole discretion, for any reason or no reason, with a full refund payable to you. Notice of such denial will be made using the contact information provided by you.

Failure to receive such notice will not alter or invalidate the denial. In no event will Elsevier or Copyright Clearance Center be responsible or liable for any costs, expenses or damage incurred by you as a result of a denial of your permission request, other than a refund of the amount(s) paid by you to Elsevier and/or Copyright Clearance Center for denied permissions.

LIMITED LICENSE

The following terms and conditions apply only to specific license types:

15. Translation: This permission is granted for non-exclusive world English rights only unless your license was granted for translation rights. If you licensed translation rights you may only translate this content into the languages you requested. A professional translator must perform all translations and reproduce the content word for word preserving the integrity of the article.

16. Posting licensed content on any Website: The following terms and conditions apply as follows: Licensing material from an Elsevier journal: All content posted to the web site must maintain the copyright information line on the bottom of each image; A hyper-text must be included to the Homepage of the journal from which you are licensing at http://www.sciencedirect.com/science/journal/xxxxx or the Elsevier homepage for books at http://www.elsevier.com; Central Storage: This license does not include permission for a scanned version of the material to be stored in a central repository such as that provided by Heron/XanEdu.

Licensing material from an Elsevier book: A hyper-text link must be included to the Elsevier homepage at http://www.elsevier.com . All content posted to the web site must maintain the copyright information line on the bottom of each image.

Posting licensed content on Electronic reserve: In addition to the above the following clauses are applicable: The web site must be password-protected and made available only to bona fide students registered on a relevant course. This permission is granted for 1 year only.

You may obtain a new license for future website posting.

17. For journal authors: the following clauses are applicable in addition to the above:

Preprints:

A preprint is an author's own write-up of research results and analysis, it has not been peer reviewed, nor has it had any other value added to it by a publisher (such as formatting, copyright, technical enhancement etc.).

Authors can share their preprints anywhere at any time. Preprints should not be added to or enhanced in any way in order to appear more like, or to substitute for, the final versions of articles however authors can update their preprints on arXiv or RePEc with their Accepted Author Manuscript (see below).

If accepted for publication, we encourage authors to link from the preprint to their formal publication via its DOI. Millions of researchers have access to the formal publications on ScienceDirect, and so links will help users to find, access, cite and use the best available version. Please note that Cell Press, The Lancet and some society-owned have different preprint policies. Information on these policies is available on the journal homepage.

Accepted Author Manuscripts: An accepted author manuscript is the manuscript of an article that has been accepted for publication and which typically includes author incorporated changes suggested during submission, peer review and editor-author communications.

Authors can share their accepted author manuscript: immediately via their non-commercial person homepage or blog by updating a preprint in arXiv or RePEc with the accepted manuscript via their research institute or institutional repository for internal institutional uses or as part of an invitation-only research collaboration work-group directly by providing copies to their students or to research collaborators for their personal use for private scholarly sharing as part of an invitation-only work group on commercial sites with which Elsevier has an agreement. After the embargo period via non-commercial hosting platforms such as their institutional repository via commercial sites with which Elsevier has an agreement. In all cases accepted manuscripts should: link to the formal publication via its DOI, bear a CC-BY-NC-ND license - this is easy to do if aggregated with other manuscripts, for example in a repository or other site, be shared in alignment with our hosting policy not be added to or enhanced in any way to appear more like, or to substitute for, the published journal article.

Published journal article (JPA): A published journal article (PJA) is the definitive final record of published research that appears or will appear in the journal and embodies all value-adding publishing activities including peer review co-ordination, copy-editing, formatting, (if relevant) pagination and online enrichment.

Policies for sharing publishing journal articles differ for subscription and gold open access articles:

Subscription Articles: If you are an author, please share a link to your article rather than the full-text. Millions of researchers have access to the formal publications on ScienceDirect, and so links will help your users to find, access, cite, and use the best available version. Theses and dissertations which contain embedded PJAs as part of the formal submission can be posted publicly by the awarding institution with DOI links back to the formal publications on ScienceDirect. If you are affiliated with a library that subscribes to ScienceDirect you have additional private sharing rights for others' research accessed under that agreement. This includes use for classroom teaching and internal training at the institution (including use in course packs and courseware programs), and inclusion of the article for grant funding purposes.

Gold Open Access Articles: May be shared according to the author-selected end-user license and should contain a CrossMark logo, the end user license, and a DOI link to the formal publication on ScienceDirect. Please refer to Elsevier's posting policy for further information.

18. For book authors the following clauses are applicable in addition to the above: Authors are permitted to place a brief summary of their work online only. You are not allowed to download and post the published electronic version of your chapter, nor may you scan the printed edition to create an electronic version. Posting to a repository: Authors are permitted to post a summary of their chapter only in their institution's repository.

19. Thesis/Dissertation: If your license is for use in a thesis/dissertation your thesis may be submitted to your institution in either print or electronic form. Should your thesis be published commercially, please reapply for permission. These requirements include permission for the Library and Archives of Canada to supply single copies, on demand, of the complete thesis and include permission for Proquest/UMI to supply single copies, on demand, of the complete thesis. Should your thesis be published commercially, please reapply for permission. Theses and dissertations which contain embedded PJAs as part of the formal submission can be posted publicly by the awarding institution with DOI links back to the formal publications on ScienceDirect.

Elsevier Open Access Terms and Conditions

You can publish open access with Elsevier in hundreds of open access journals or in nearly 2000 established subscription journals that support open access publishing. Permitted third party re-use of these open access articles is defined by the author's choice of Creative Commons user license. See our open access license policy for more information.

Terms & Conditions applicable to all Open Access articles published with Elsevier: Any reuse of the article must not represent the author as endorsing the adaptation of the article nor should the article be modified in such a way as to damage the author's honour or reputation. If any changes have been made, such changes must be clearly indicated. The author(s) must be appropriately credited and we ask that you include the end user license and a DOI link to the formal publication on ScienceDirect. If any part of the material to be used (for example, figures) has appeared in our publication with credit or acknowledgement to another source it is the responsibility of the user to ensure their reuse complies with the terms and conditions determined by the rights holder.

Additional Terms & Conditions applicable to each Creative Commons user license: CC BY: The CC-BY license allows users to copy, to create extracts, abstracts and new works from the Article, to alter and revise the Article and to make commercial use of the Article (including reuse and/or resale of the Article by commercial entities), provided the user gives appropriate credit (with a link to the formal publication through the relevant DOI), provides a link to the license, indicates if changes were made and the licensor is not represented as endorsing the use made of the work. The full details of the license are available at http://creativecommons.org/licenses/by/4.0.

CC BY NC SA: The CC BY-NC-SA license allows users to copy, to create extracts, abstracts and new works from the Article, to alter and revise the Article, provided this is not done for commercial purposes, and that the user gives appropriate credit (with a link to the formal publication through the relevant DOI), provides a link to the license, indicates if changes were made and the licensor is not represented as endorsing the use made of the work. Further, any new works must be made available on the same

conditions. The full details of the license are available at http://creativecommons.org/licenses/by-nc-sa/4.0.

CC BY NC ND: The CC BY-NC-ND license allows users to copy and distribute the Article, provided this is not done for commercial purposes and further does not permit distribution of the Article if it is changed or edited in any way, and provided the user gives appropriate credit (with a link to the formal publication through the relevant DOI), provides a link to the license, and that the licensor is not represented as endorsing the use made of the work. The full details of the license are available at http://creativecommons.org/licenses/by-nc-nd/4.0. Any commercial reuse of Open Access articles published with a CC BY NC SA or CC BY NC ND license requires permission from Elsevier and will be subject to a fee.

Commercial reuse includes: Associating advertising with the full text of the article, charging fees for document delivery or access, article aggregation, systematic distribution via e-mail lists or share buttons.

Posting or linking by commercial companies for use by customers of those companies.

CURRICULUM VITAE

AYŞE MERVE GENÇ ÜNALAN

Department of Metallurgical and Materials Engineering

Middle East Technical University, D209,

06800, Ankara, TURKEY

e-mail: aysemervegenc@gmail.com

mobile: +90 (532) 243 6254

FORMAL EDUCATION

- ***Doctor of Philosophy,*** Department of Metallurgical and Materials Engineering (February 2011-Oct 2017), Middle East Technical University (METU), Ankara, TURKEY.
  Dissertation: "Development of rare-earth free permanent magnets"
  Supervisor: Assoc. Prof. Dr. Y. Eren Kalay
  Co-supervisor: Prof. Dr. Vedat Akdeniz
- ***Master of Science,*** Norman B. Keevil Institute of Mining Engineering (Sept 2009), University of British Columbia (UBC), BC, CANADA.
  Dissertation: "Power draw measurements as a method of characterization of particle aggregation"
  Supervisor: Prof. Dr. Janusz Laskowski
- ***Bachelor of Science***, Department of Mining Engineering (June 2007), Hacettepe University, Ankara, TURKEY.

ACADEMIC RESEARCH EXPERIENCE

- Teaching Assistant, Department of Metallurgical and Materials Engineering (2011-2017) Middle East Technical University (METU), Ankara, TURKEY.

- Research Assistant, Norman B. Keevil Institute of Mining Engineering (2007-2009) University of British Columbia (UBC), BC, CANADA.

AWARDS AND ACHIEVEMENTS

- Hacettepe University Student Achievement Award for graduating with the highest GPA in Mining Department (July, 2007),
- İhsan Doğramacı Outstanding Achievement Award for graduating with the highest GPA in Mining Engineering (October, 2007),
- University of British Columbia International Student Scholarship for a Master's Degree in Applied Science (August, 2007).

PUBLICATIONS

1. A. M. Genc, V. Akdeniz, T. Ozturk, Y. E. Kalay, Synthesis of AlNiCo core/shell nanopowders, Journal of Magnetism and Magnetic Materials, 2016, Volume 417, p. 112-116.
2. O. Acar, A. M. Genc, I. Kalay, Y. E. Kalay, Effect of composition on the phase transformations of Mn-Al Alloys, Journal of Alloys and Compounds (submitted)
3. A. M. Genc, I. Kilickaplan, J. S. Laskowski, Effect of pulp rheology on flotation of nickel sulphide ore with fibrous gangue particles, Canadian Metallurgical Quarterly, 51(4), 2012, p. 368-375.
4. A. M. Genc, I. Kilickaplan, J. S. Laskowski, Pulp rheology in the flotation of serpentinised ultramafic Nickel Sulfide Ore and Its Effect on Flotation, Proceedings of the 8th University of British Columbia Mcgill-University of Alberta International Symposium on the Fundamentals of Mineral Processing, 2010, p. 13 -19.
5. A. M. Genc, J. S. Laskowski, Power draw measurements as a research tool in studying flotation of the Nickel Sulfide ore with fibrous gangue, Proceedings of

the 8th University of British Columbia-McGill University of Alberta International Symposium on the Fundamentals of Mineral Processing, 2010, p. 75-91.

PRESENTATIONS

1. Power Draw Measurements as a Research Tool in Studying Flotation of the Nickel Sulfide Ore with Fibrous Gangue, A.M. Genc, J.S. Laskowski, COM 2010, CANADA.
2. Pulp Rheology in the Flotation of Serpentinised Ultramafic Nickel Sulfide and Its Effect on Flotation, A. M. Genc, I. Kılıckaplan, J.S. Laskowski, COM 2010, CANADA.
3. The Effects of Pre-Peak Formation in MRO Structure, T. Demirtas, A.M. Genc, Y.E. Kalay, EMK 2011, TURKEY.
4. Particle Size Dependence on Magnetic Properties of AlNiCo Powders, A. M. Genc, Y. E. Kalay, TMS 2014, USA.
5. Production and Characterization of AlNiCo Nanopowders, A. M. Genc, Y.E. Kalay, TMS 2015, USA.
6. Characterization of Mn-Al Magnetic Alloys, O. Acar, A.M. Genc, Y. E. Kalay, I. Kalay, TMS 2015, USA.
7. Development of AlNiCo Nanopowders with Improved Coercivity, A.M. Genc, M.V. Akdeniz, T. Ozturk, Y.E. Kalay, MRS Fall 2015, USA.
8. Development of Rare-Earth Free Permanent Magnets, A.M. Genc, O. Acar, Y. E. Kalay, EMK 2015, TURKEY.
9. Epsilon to Tau Phase Transformation in MnAl Alloy Systems, A.M. Genc, O. Acar, Y. E. Kalay, TMS 2016, USA.
10. Synthesis of AlNiCo Core/Shell Nanopowders by Hydrogen Plasma Reaction, A.M. Genc, M.V. Akdeniz, T. Ozturk, Y.E. Kalay, MRS Fall 2016, USA.
11. Microstructural Characterization of Magnetic MnAl Alloys, A.M. Genc, O. Acar, Y. E. Kalay, TMS 2017, USA.